

Politecnico di Torino

Politecnico di Torino

Master's Degree in Agritech Engineering

Application of UAVs for Agricultural Monitoring

The Case of Orchards with Anti-Hail Nets

Supervisors:
Prof. Danilo Demarchi
Prof. Paolo Gay
Prof. Lorenzo Comba
Dott. Massimo Vincenzo Ferro

Candidate:
Giacomo Gaboardi

Academic Year 2025/2026
September 2026

Abstract

Agricultural anti-hail and shading nets are increasingly common in modern orchards as a defense against extreme weather, but they interfere directly with UAV based remote sensing. Because the nets physical openings are much smaller than a drone camera's pixel footprint, each recorded pixel mixes the reflectance of the polymeric threads, the underlying canopy and the cast micro shadows, a phenomenon known as the mixed pixel effect. This distorts vegetation indices such as NDVI and can lead to unreliable agronomic assessments in netted orchards.

This work builds a methodological framework to isolate and quantify that distortion, moving from a controlled laboratory setting to a real field campaign. In the lab, a Specim FX10 hyperspectral scanner and an RS-5400 spectroradiometer were used to characterize four commercial anti-hail nets (black, light green, grey/black and transparent). The optical setup itself was validated first, establishing that a raised acquisition geometry produces the diffused, uniform shadow needed to correctly simulate an airborne perspective. The pure spectral signature of each net was then extracted through supervised spatial segmentation. The two sensors were cross validated first without nets and then both above and below the net, confirming that the acquisitions were successful, and the results will be reliable. The hyperspectral data was then computationally resampled to the nine discrete bands of the MAIA S2 multispectral sensor, revealing that light attenuation under the nets is strongly wavelength dependent rather than uniform. This effect is particularly marked for the light green net, whose shading factor collapses in the near infrared while remaining significant in the visible range. The laboratory results still need to be brought together into a full quantitative synthesis, which is left as the immediate next step of this work.

The laboratory findings were then tested against an outdoor campaign conducted in an experimental apple orchard. Because the orchard contains different apple varieties, tree level canopy reflectance could not serve as a rigid term of comparison between netted and non netted rows: ground based white reference panels were used instead, giving a stable, variety independent benchmark against which the two conditions could be compared. Flights were carried out with the same MAIA S2 nine band multispectral sensor used in the laboratory simulation, over rows covered respectively by light green and grey/black nets over adjacent uncovered rows, allowing a direct spectral comparison between netted and open canopy under real illumination conditions.

NDVI maps were generated for both scenarios to visualize how the presence of the nets alters the spatial vigor pattern normally used for crop diagnostics. The laboratory characterization and the field validation together offer a reliable base-

line for understanding how shading nets bias UAV based multispectral monitoring, and point toward the band specific correction strategies that precision agriculture workflows over netted orchards will need going forward.

Contents

1 Introduction **1**
- 1.1 Precision Agriculture and UAVs . . . 1
- 1.2 The impact of anti-hail nets . . . 2
  - 1.2.1 Radiometric Alteration . . . 3
  - 1.2.2 Spatial and Spectral Fusion (Mixed Pixel Effect) . . . 3
- 1.3 The Role of Hyperspectral Imaging . . . 3
- 1.4 Thesis Objectives and Structure . . . 4

2 Background and State of the Art **5**
- 2.1 Proximal Remote Sensing and Vegetation Indices . . . 5
  - 2.1.1 Physical Principles of Crop Reflectance . . . 5
  - 2.1.2 UAVs as Proximal Sensing Platforms . . . 7
  - 2.1.3 Vegetation Indices and Agronomic Applications . . . 9
- 2.2 Sensing Technologies and Platforms in Precision Agriculture . . . 12
  - 2.2.1 The Proximal Sensing Toolbox . . . 12
  - 2.2.2 Deployment Kinematics: Terrestrial and Aerial Platforms . . . 13
  - 2.2.3 Technology Adoption and Cost Effective Innovations in the Italian Context . . . 15
  - 2.2.4 High Resolution Radiometry and the Hyperspectral Approach 15
- 2.3 Optical Properties and Photobiology under Netted Environments . . 17

3 Materials and Methods **19**
- 3.1 Indoor Laboratory Experimentation . . . 19
  - 3.1.1 Experimental Setup and Instrumentation . . . 19
  - 3.1.2 Sample Characterization: The Shading Nets . . . 21
- 3.2 Conceptual Optical Model and Radiometric Nomenclature . . . 22
- 3.3 First Laboratory Session: Optical Setup Validation . . . 24
- 3.4 Second Laboratory Session: Sensor Cross Validation . . . 27
  - 3.4.1 Acquisition Protocol and Dual Sensor Sampling . . . 27
  - 3.4.2 Geometric Fractional Area and Color Segmentation . . . 28
  - 3.4.3 Radiometric Cross Validation Workflows . . . 29
- 3.5 Spectral Aggregation and Multispectral Simulation . . . 31
  - 3.5.1 Agronomic Translation and Shading Factor Extraction . . . 31
  - 3.5.2 Spectral Simulation of the Maia S2 Multispectral Sensor . . . 31
- 3.6 Outdoor Field Surveys . . . 33
  - 3.6.1 UAV Platform and Flight Planning . . . 33
  - 3.6.2 Experimental Design and Target Deployment . . . 35

3.6.3 Photogrammetric Pipeline and Data Extraction 36

4 Results **41**
4.1 Optical Setup Validation 41
4.2 Nets Optical and Spectral Characterization 45
4.2.1 Baseline Calibration 45
4.2.2 Morphometric Analysis and Spatial Segmentation 46
4.2.3 The Spectral Atlas 48
4.2.4 Agronomic Parameters and Shading Factor Evaluation 50
4.2.5 Comparative Baseline Assessment: Instrument Alignment . . . 51
4.2.6 Above Canopy Radiometric Analysis: The UAV Mixed Pixel Simulation 52
4.2.7 Sub Canopy Radiometric Analysis: Transmitted Light Assessment 56
4.2.8 Multispectral Sensor Simulation 61
4.3 UAV Field Validation 63
4.3.1 Spatial Distribution and Solar Angle Effect 63
4.3.2 Statistical Quantification of the Shading Bias 65

5 Discussions **69**
5.1 Synthesis of the Radiometric Impact of Shading Nets 69
5.2 Cross Scale Radiometric Consistency: Laboratory vs UAV Field Acquisitions 70
5.3 Implications for Precision Agriculture Monitoring 71
5.3.1 The Diffuser Effect and Loss of Radiometric Variance 71
5.3.2 Systematic Bias in Prescription Maps 72
5.3.3 Statistical Discriminative Capacity 72

6 Conclusions and Future Developments **75**
6.1 Conclusions 75
6.2 Operational Guidelines 75
6.3 Future Developments 76

List of Figures

1.1 Satellite perspective illustrating the diverse spectral effects of anti-hail net installations on agricultural landscapes. Contiguous fields covered by different net typologies exhibit distinct color variations, demonstrating the varying degrees of optical filtering. The complex pattern of colored fields highlights the challenge of uniform remote sensing. [1] 2

2.1 The relationship between the typical spectral signature of healthy vegetation (a) and the internal leaf anatomy (b). While VIS reflectance is governed by pigment absorption, the high NIR reflectance is driven by structural scattering within the spongy mesophyll. 6

2.2 Conceptual illustration of spectral reflectance variation based on leaf health. While visible light (Blue, Green, Red) reflectance changes slightly with pigment degradation, the Near Infrared (NIR) reflectance dramatically collapses as the internal cellular structure of the leaf deteriorates from healthy to dead. 7

2.3 Geometric relationship defining the Ground Sample Distance (GSD). The spatial footprint of a single pixel on the ground is a direct function of the flight altitude (h), the sensor's pixel pitch (p), and the lens focal length (f). 8

2.4 Output of the photogrammetric Structure from Motion (SfM) pipeline. The generation of a dense 3D point cloud allows for the precise geometric reconstruction of the canopy architecture, enabling spatial filtering and the isolation of the target vegetation from the background. 9

2.5 Spectral signature of healthy vegetation highlighting the specific wavelength bands utilized for calculating standard agronomic indices. The precise positioning of the Green, Red, RedEdge, and Near Infrared (NIR) regions determines the specific physiological sensitivity of GNDVI, NDVI, and NDRE. 11

2.6 Mixed pixel effect within the sensor's IFOV. The total reflectance ($\bar{R}_{pixel}$) is a linear combination of the sunlit canopy (R_{leaf}), the net threads (R_{net}), and the projected micro shadows (R_{shadow}), each weighted by its respective fractional area (f_i) where $\sum f_i = 1$. 11

2.7 Examples of standard proximal sensing hardware utilized in precision agriculture operations. From left to right: an active LiDAR sensor for geometric 3D reconstruction, a passive multispectral camera for standard vegetation indices, and a passive hyperspectral line scanner for high fidelity radiometric analysis. 13

2.8 Autonomous deployment platforms utilized in precision agriculture. (a) A UGV designed for sub canopy navigation, operating with a lateral optical perspective. (b) A UAV platform engineered for field scale nadiral data acquisition, providing top down radiometric mapping. 14

2.9 Conceptual schematic of the pushbroom acquisition principle utilized by the Specim FX10 sensor. The optical system captures spatial information strictly along a single slit and disperses the incoming light into continuous spectral bands. A complete three dimensional hypercube is generated by physically translating the sensor or the target area at a strictly constant velocity. 16

3.1 Complete overview of the Specim FX10 experimental setup, showing the hyperspectral camera mounted on the motorized linear translation stage, the sample area, the halogen illumination system, and the control laptop. 20

3.2 Configuration of the RS-5400 spectral analysis system. (a) A close up detail of the measurement probe and the black/white calibration standard in position on the motorized stage. (b) An overview of the complete test bench, including the spectrometer unit (housed in the backpack), the scanning device, and the user interface on the handheld tablet. 21

3.3 Macro photographs detailing the visual appearance and weaving patterns of the four agricultural shading nets evaluated in the second session. 22

3.4 Conceptual optical model detailing the directional light pathways and the distinct radiometric signals captured by the dual sensor setup. White arrows represent the illumination fluxes, blue arrows indicate the high resolution spatial measurements acquired by the Specim FX10 hyperspectral scanner, and red arrows denote the macroscopic point measurements recorded by the RS-5400 spectroradiometer. . . . 23

3.5 Visual comparison illustrating the radiometric calibration process in MATLAB. (a) Raw hyperspectral frame before correction, affected by illumination non uniformity; (b) Calibrated reflectance image utilizing the white background and dark references. 25

3.6 Comparison of the manual sampling procedure implemented in MATLAB for Net 02. Multiple polygonal regions (highlighted in yellow) were selected strictly within the mesh openings to isolate the background. The comparison highlights the sharp, distinct shadows in Setup 1 (a) versus the more diffused, uniform radiometric field in Setup 3 (b). 26

3.7 Supervised spatial sampling procedure implemented in MATLAB, demonstrated on the transparent Net 06. The operator manually identifies pure pixels for both the physical netting material (a) and the empty background spaces (b). These manual selections act as training data for the subsequent automatic spatial classification. . . . 29

3.8 Relative spectral sensitivity curves of the MAIA S2 multispectral sensor across the visible and near infrared spectrum. 32
3.9 The DJI Matrice 350 RTK quadcopter equipped with the MAIA S2 multispectral payload, utilized for the outdoor field surveys. The top mounted Incident Light Sensor (ILS) is clearly visible above the main chassis. 34
3.10 Schematic top down layout of the experimental design. The orchard was divided into four distinct zones, with eight identical white calibration panels evenly distributed at ground level within each block to serve as absolute radiometric references. 35
3.11 In field deployment of the white calibration panels. The artificial targets were positioned on the grass alleys directly beneath the protective nets (a) and in the open sky control zones (b) to provide a stable, variety independent radiometric baseline. 36
3.12 Photogrammetric outputs generated in Agisoft Metashape. (a) The dense 3D point cloud providing the detailed geometric structure of the orchard and the protective nets. (b) The continuous Digital Surface Model (DSM) interpolated from the dense cloud, necessary for the accurate orthorectification of the multispectral data. 37
3.13 Manual delineation of the polygonal Region of Interest (ROI) over a white calibration panel on the processed orthomosaic. NDVI values were extracted exclusively from the internal pixels to avoid signal contamination. 38

4.1 Comparison of spectral signatures across different acquisition setups for Net 01 (Dark Green). Above the mean reflectance and under the standard deviation. 42
4.2 Comparison of spectral signatures across different acquisition setups for Net 02 (Black).Above the mean reflectance and under the standard deviation. 43
4.3 Comparison of spectral signatures across different acquisition setups for Net 03 (Light Green). Above the mean reflectance and under the standard deviation. 43
4.4 Comparison of spectral signatures across different acquisition setups for Net 04 (Transparent). Above the mean reflectance and under the standard deviation. 44
4.5 Comparison of spectral signatures across different acquisition setups for Net 05 (Grey). Above the mean reflectance and under the standard deviation. 44
4.6 Visual demonstration of the baseline calibration process (exemplified on Net 03, Light Green). The left panel displays the raw, uncalibrated digital numbers affected by illumination gradients, while the right panel shows the processed reflectance yielding a completely uniform radiometric background. 46

4.7 Example of the automated spatial segmentation process. The algorithm evaluates the calibrated Region of Interest (left) by calculating the spectral angles (center), ultimately generating the isolated binary mask of the physical threads (right). 47
4.8 Final segmented masks utilized for the geometric fractional area extraction. Monocolor nets (02 and 06) are isolated using binary logic, while bicolor nets (03 and 05) employ multiclass segmentation to distinguish specific pigment contributions. 48
4.9 Spectral Atlas of the four definitive agricultural shading nets. The top panel displays the pure mean reflectance of the solid polymeric threads across the VNIR range. The bottom panel illustrates the spatial standard deviation (σ), confirming the high radiometric homogeneity of the extracted signal. 49
4.10 Baseline sensor cross validation on the bare white background. The peak normalized spectral curves illustrate the distinct hardware responses of the Specim FX10 scanner and the RS 5400 spectroradiometer to the halogen illumination source, prior to the introduction of the shading nets. 52
4.11 Repeatability of the RS 5400 spectroradiometer measurements over Net 03 (Light Green). The graph illustrates the five discrete conical acquisitions (grey lines) capturing localized structural variations, and the resulting spatially integrated mean (orange line) utilized for the cross validation. 53
4.12 Above canopy spectral comparison for Net 02 (Black). The macroscopic mixed signal demonstrates excellent morphological correlation between the Specim FX10 rectangular ROI and the RS 5400 spatial average, successfully validating the UAV pixel simulation. 54
4.13 Above canopy spectral comparison for Net 06 (Transparent). The high morphological alignment mathematically validates the accuracy of the macroscopic radiometric field captured by the experimental setup. 54
4.14 Above canopy spectral comparison for Net 03 (Light Green). The highly synchronized spectral curves correctly capture the complex mixed pixel integration of the transmissive green threads and the underlying background. 55
4.15 Above canopy spectral comparison for Net 05 (Grey/Black). Both instruments perfectly map the stable radiometric attenuation of the heterogeneous structure from above the canopy. 55
4.16 Sub canopy spectral comparison for Net 03 (Light Green). The optical diffusion of the green polymer homogenizes the light field, allowing the conical integration of the RS 5400 to successfully correlate with the spectral shape of the Specim FX10 extraction. 57
4.17 Sub canopy spectral comparison for Net 06 (Transparent). The high broadband transmittance yields a uniform transmitted radiation field, ensuring excellent spectral shape correlation between both instrument modalities. 58

4.18 Sub canopy spectral comparison for Net 02 (Black). The highly absorbing polymer generates sharp, high contrast shadows, causing the spatial integration within the 5 RS 5400 conical footprints to fail in accurately matching the morphological shape of the rigorously masked Specim FX10 signal. 59
4.19 Sub canopy spectral comparison for Net 05 (Grey/Black). Similar to Net 02, the absorbing structural threads create macroscopic spatial heterogeneity, leading to a morphological mismatch between the discrete FOV average and the continuous spatial extraction. 59
4.20 Simulated spectral signatures of the shading nets across the nine discrete bands of the MAIA S2 multispectral sensor, derived from the high resolution Specim FX10 datacubes. 62
4.21 NDVI spatial distribution map of the experimental orchard acquired during Flight 1 at solar noon (12:00 PM). The map illustrates the clear radiometric attenuation in the netted zones compared to the open sky control rows under optimal illumination conditions. 64
4.22 NDVI spatial distribution map acquired during Flight 2 in the mid afternoon (4:00 PM). A generalized signal reduction is observed across the entire orchard compared to solar noon, primarily driven by the lower solar elevation angle and the consequent increase in shadowing effects. 64
4.23 Statistical comparison of mean NDVI values across treatments for Flight 1 (Solar Noon). Bars sharing the same letter are not significantly different according to Tukey's HSD post hoc test ($p > 0.05$). The sensor successfully differentiates the open sky control ('a') from the covered zones ('b'), but fails to distinguish between the Green and Black networks. 66
4.24 Statistical comparison of mean NDVI values across treatments for Flight 2 (Mid Afternoon). Despite the generalized reduction in absolute NDVI values caused by the lower solar angle, the statistical relationship remains identical to solar noon, confirming the systemic nature of the shading bias. 66

List of Tables

3.1 Visual and material characteristics of the evaluated shading nets. . . 22
3.2 Spectral specifications of the nine discrete bands of the MAIA S2 multispectral sensor. 32

4.1 Morphometric results detailing the total physical area occupied by the shading nets and the specific internal pigment distribution for bicolor samples. 47
4.2 Aggregated agronomic parameters evaluating the total radiometric transmission and practical shading capacity of the four evaluated networks. 50
4.3 Above canopy macroscopic mean reflectance across the primary spectral intervals. The Δ Offset column mathematically highlights the constant geometric shift between the two sensors, confirming their identical capacity to capture the spectral signatures. 56
4.4 Sub canopy absolute transmitted reflectance across the primary spectral intervals. The wavelength dependent variations in the Δ offset for Nets 02 and 05 quantify the spatial heterogeneity and micro shadowing effects characterizing the transmitted light field. 60
4.5 Band dependent Shading Factor (SF_λ %) evaluated across the nine discrete optical channels of the MAIA S2 multispectral sensor for each evaluated net. 62
4.6 Descriptive statistics of the NDVI values extracted from the white calibration panels during Flight 1 (Solar Noon, 12:00 PM). 65
4.7 Descriptive statistics of the NDVI values extracted from the white calibration panels during Flight 2 (Mid Afternoon, 4:00 PM). 65

List of Equations

2.1 Radiative energy balance of a leaf surface 5
2.2 Theoretical Ground Sample Distance (GSD) 8
2.3 Normalized Difference Vegetation Index (NDVI) 10
2.4 Green Normalized Difference Vegetation Index (GNDVI) 10
2.5 Normalized Difference Red Edge (NDRE) 10
3.1 Radiometric calibration of raw datacubes 25
3.2 Spatial Standard Deviation 27
3.3 Calculation of the practical Shading Factor 31
4.1 Length of the pure shadow cone (umbra) 42

Chapter 1

Introduction

1.1 Precision Agriculture and UAVs

Modern agriculture is currently undergoing a crucial transition from conventional, uniform field management to data driven precision agriculture. [2] This paradigm shift is increasingly necessary to address contemporary global challenges, including the unpredictable impacts of climate change, the urgent need to optimize inputs (such as water, fertilizers, and plant protection products), and the growing market demand for high quality yields. By managing spatial and temporal variability within the field, precision agriculture aims to maximize agricultural efficiency while simultaneously reducing the environmental footprint.

Within this transitional phase, Unmanned Aerial Vehicles (UAVs) have emerged as highly versatile and effective remote sensing platforms. When compared to traditional satellite imagery, which is frequently hindered by cloud cover and limited by lower spatial resolutions, UAVs offer the distinct advantage of on demand flights below the cloud layer, providing centimeter level Ground Sample Distance (GSD).[3] This ultra high resolution is particularly beneficial for monitoring high value agricultural systems, such as orchards and vineyards.

Furthermore, UAVs offer significant operational advantages over ground based machinery. Unlike heavy tractors, drones do not cause soil compaction or mechanical damage to the crops, and they can be deployed even when field conditions are inaccessible due to heavy rains. Crucially, UAVs guarantee high levels of operational safety, capable of effortlessly mapping steep slopes or hazardous environments where driving a tractor would pose significant risks to the operator. However, it is essential to emphasize that drones are not intended to replace ground vehicles. The most effective precision agriculture framework relies on their collaboration: UAVs provide rapid, high resolution diagnostic mapping of the field, which in turn guides the targeted, variable rate interventions executed by intelligent tractors and ground rovers.

The core agronomic value of a UAV lies in its sensor payload, most notably multispectral cameras. Unlike standard RGB sensors that capture only the visible spectrum, multispectral cameras isolate specific, narrow bands of light, particularly in the Near Infrared (NIR) region, which is strongly correlated with the internal cellular structure and health of plant leaves. By mathematically combining the re-

flectance values of these specific wavelengths, typically the Red and NIR bands, it is possible to compute vegetation indices. The Normalized Difference Vegetation Index (NDVI) is the most widely adopted standard for evaluating vegetative vigor, estimating biomass, and mapping spatial variability. Through these multispectral indices, farmers can clearly identify areas of crop stress and monitor the overall health of the orchard, translating raw optical data into actionable agronomic insights.

1.2 The impact of anti-hail nets

To mitigate the increasing risks associated with extreme weather events and climate change, modern orchards and high value crops are frequently protected by agricultural canopies, such as anti-hail and shading nets. While these protective structures are essential for safeguarding the harvest and regulating the microclimate, they introduce a significant physical obstacle for remote sensing operations. Interposed directly between the UAV sensor and the crop canopy, the netting system acts as a complex optical filter, profoundly altering both the incoming solar irradiance and the outgoing reflected radiance before it reaches the camera.



Figure 1.1: Satellite perspective illustrating the diverse spectral effects of anti-hail net installations on agricultural landscapes. Contiguous fields covered by different net typologies exhibit distinct color variations, demonstrating the varying degrees of optical filtering. The complex pattern of colored fields highlights the challenge of uniform remote sensing. [1]

1.2.1 Radiometric Alteration

The presence of a protective net modifies the optical signal in two fundamental ways: by reducing the total amount of light reaching the plants (quantitative alteration, or shading) and by modifying the spectral composition of the light (qualitative alteration).[4] Depending on the specific material, weaving pattern, and thread color (for example black, green, transparent, or grey), the net selectively absorbs, transmits, and reflects different wavelengths. This selective filtering heavily impacts the Visible (VIS) and Near Infrared (NIR) regions of the electromagnetic spectrum. Consequently, the raw reflectance values recorded by the sensor are distorted, which inevitably propagates errors into the mathematical calculation of vegetation indices like the NDVI, potentially leading to inaccurate or biased agronomic assessments.

1.2.2 Spatial and Spectral Fusion (Mixed Pixel Effect)

Beyond the radiometric filtering, UAV based acquisitions over netted crops suffer from a critical geometric limitation known as the mixed pixel effect.[5] The physical openings of standard agricultural meshes are typically on the scale of a few millimeters. Conversely, even at very low flight altitudes, the Ground Sample Distance (GSD) of a multispectral UAV camera generally ranges of centimeters. Because the sensor's pixel footprint is geometrically larger than the individual holes in the net, the camera is physically incapable of "looking through" the mesh to capture a pure signal of the underlying canopy. Instead, each individual pixel performs a spatial integration, blending the optical signature of the solid polymeric threads with the optical signature of the vegetation and the shadowed gaps below. This fusion creates a contaminated, composite reflectance that no longer represents the true physiological state of the crop alone.

1.3 The Role of Hyperspectral Imaging

To effectively quantify and ultimately correct the radiometric distortions and the mixed pixel effect observed in UAV imagery, it is first necessary to understand the precise optical behavior of the protective nets. Standard multispectral sensors, while highly efficient for field scale agronomic monitoring, capture light across a few relatively broad spectral bands. This broad resolution is insufficient to isolate the complex, wavelength dependent filtering caused by the structural threads.

Therefore, a rigorous optical characterization necessitates a controlled laboratory approach utilizing high resolution hyperspectral imaging. Unlike multispectral cameras, hyperspectral sensors capture electromagnetic radiation across hundreds of narrow, contiguous bands, generating a continuous, unbroken reflectance curve for every spatial pixel. In the context of this study, hyperspectral imaging acts as a crucial prerequisite: it provides the precise radiometric study needed to decouple the pure spectral signature of the polymeric meshes from the underlying background. Only through this deep optical characterization in a laboratory environment is it possible to mathematically understand how different net typologies alter the spectral signal, providing the foundation to simulate and predict their impact on standard

multispectral UAV surveys.

1.4 Thesis Objectives and Structure

Although the deployment of protective canopies is increasingly common in modern orchards, there is currently a significant lack of comprehensive literature detailing exactly how these structures alter remote sensing data or how the underlying plant physiology radiometrically responds. The precise physical and spectral nature of this interference remains a largely unexplored domain.

Addressing this gap, the primary objective of this thesis is to systematically quantify and characterize the radiometric distortion introduced by agricultural shading and anti-hail nets on UAV based multispectral imagery. Specifically, the innovative character of this research lies in developing a robust methodological framework to comprehensively evaluate the entire optical system. This approach goes beyond merely observing the mixed pixel effect; it involves physically isolating the pure spectral signature of the netting material and the specific radiometric properties of the cast shadow, to subsequently and mathematically reconstruct how they interact together. By coupling high resolution indoor hyperspectral analysis with outdoor multispectral UAV validations, the study seeks to definitively understand how different net typologies alter the spectral signatures of the underlying surfaces. The ultimate goal is to provide reliable baseline data and operational guidelines that can support the future development of radiometric correction algorithms for precision agriculture flights over netted orchards.

To achieve these objectives, the manuscript is organized into a fluid progression of six chapters. Following this introductory chapter, Chapter 2 provides a comprehensive review of the state of the art, exploring current literature on UAV remote sensing, multispectral vegetation indices, and the optical interference caused by protective canopies. Chapter 3 details the materials and methods, describing the chosen optical sensors, the experimental setups designed for the laboratory, and the flight protocols applied during the open field campaigns. The core analytical outcomes are presented in Chapter 4, which sequentially reports the optical validation of the experimental setup, the spectral characterization of the selected nets, the mathematical simulation of the mixed pixel effect, and the final quantitative radiometric evaluation conducted in the field. These results are then critically interpreted in Chapter 5, where the agronomic and technical implications of the observed radiometric distortions are discussed. Finally, Chapter 6 concludes the work by summarizing the primary achievements and outlining potential trajectories for future research and operational applications.

Chapter 2

Background and State of the Art

2.1 Proximal Remote Sensing and Vegetation Indices

2.1.1 Physical Principles of Crop Reflectance

The foundation of optical remote sensing in agriculture relies on the complex physical interaction between incident electromagnetic radiation and the biological structure of plant leaves. To systematically extract agronomic data from an orchard, it is first necessary to define the leaf as an optical medium. According to the principle of conservation of energy, the spectral behavior of a canopy can be described by the radiative energy balance equation. When incident solar irradiance (I) interacts with a leaf surface, the energy is partitioned into three distinct spectral components: reflected (R), transmitted (T), and absorbed (A) radiance. Normalized against the incident light, this relationship is expressed as:

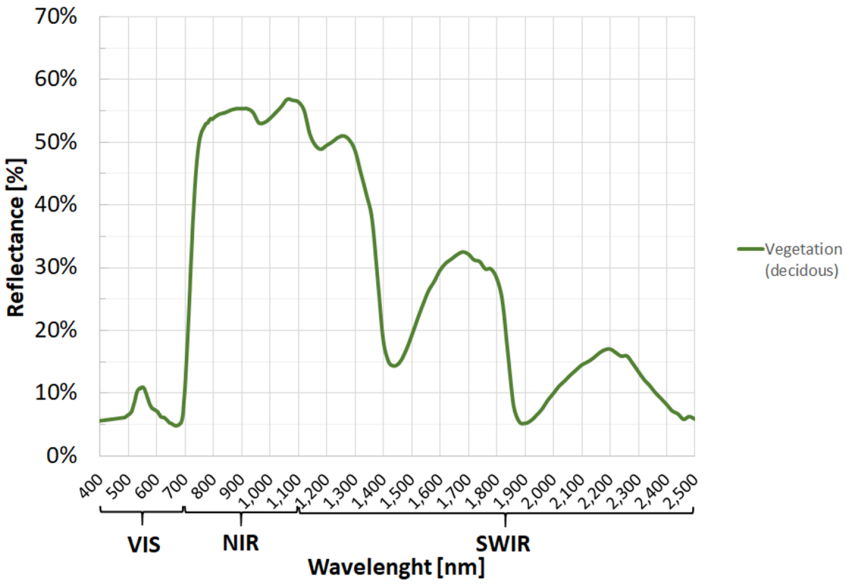
$$R(\lambda) + T(\lambda) + A(\lambda) = 1 \tag{2.1}$$

where λ represents the specific wavelength of the electromagnetic spectrum. Optical remote sensing platforms, such as multispectral and hyperspectral UAV cameras, exclusively measure the reflected component $R(\lambda)$ leaving the canopy in the direction of the sensor.

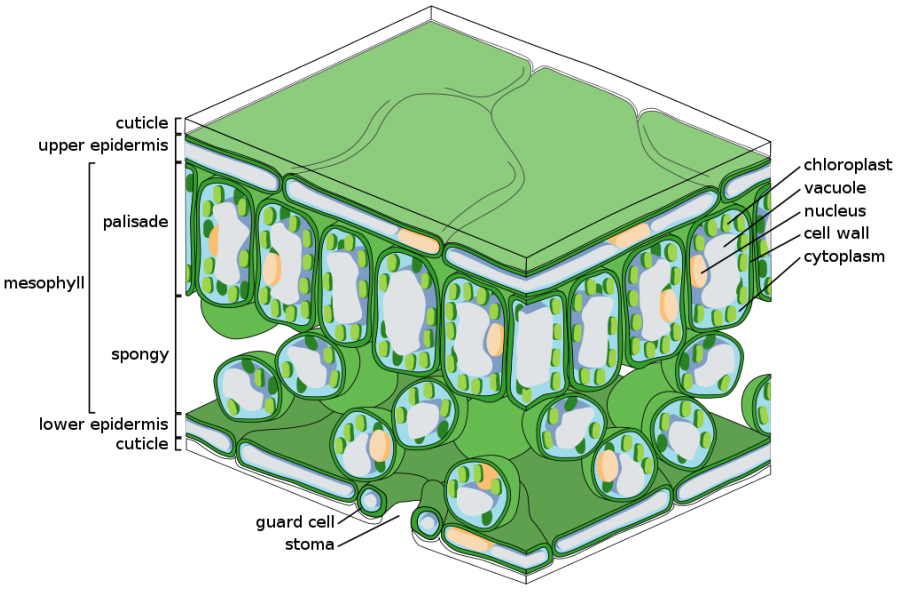
The spectral signature of healthy vegetation is highly distinctive and varies drastically across different wavelength domains due to specific biochemical and anatomical factors. In the Visible region (VIS, 400-700 nm), the optical response is heavily dominated by photosynthetic pigments, primarily chlorophyll a and b, as well as carotenoids. These pigments strongly absorb light in the blue ($\sim$450 nm) and red ($\sim$670 nm) bands to drive the photosynthetic process, collectively known as Photosynthetically Active Radiation (PAR). Consequently, overall reflectance in the VIS spectrum is remarkably low, typically remaining below 10-15%, with a relative peak around 550 nm (the "green bump") which corresponds to the green color perceived by the human eye.

Immediately beyond the visible spectrum lies the RedEdge region (680-750 nm), representing one of the most critical diagnostic features in agricultural remote sens-

ing. The RedEdge is defined as the point of maximum slope (inflection point) where the curve transitions from the strong chlorophyll induced absorption of the red band to the high reflectance of the infrared. The exact spectral position and steepness of this slope are highly sensitive indicators of plant stress and nitrogen content.



(a) Typical spectral signature [6]



(b) Leaf cellular anatomy [7]

Figure 2.1: The relationship between the typical spectral signature of healthy vegetation (a) and the internal leaf anatomy (b). While VIS reflectance is governed by pigment absorption, the high NIR reflectance is driven by structural scattering within the spongy mesophyll.

Moving into the Near Infrared region (NIR, 750-1300 nm), the nature of the optical interaction undergoes a fundamental shift. In this domain, biochemical absorp-

tion drops to near zero. Instead, the high reflectance values (often exceeding 40-50%) are driven entirely by physical and structural scattering. The internal anatomy of a healthy leaf, particularly the spongy mesophyll layer, is characterized by numerous intercellular air spaces. The continuous transitions of the refractive index between hydrated cellular walls and these air voids cause multiple internal refractions and scattering events, forcefully directing the NIR radiation back outwards. A turgid, structurally sound mesophyll will therefore produce a highly reflective NIR signal, whereas dehydration or cellular degradation will cause this reflectance to collapse.

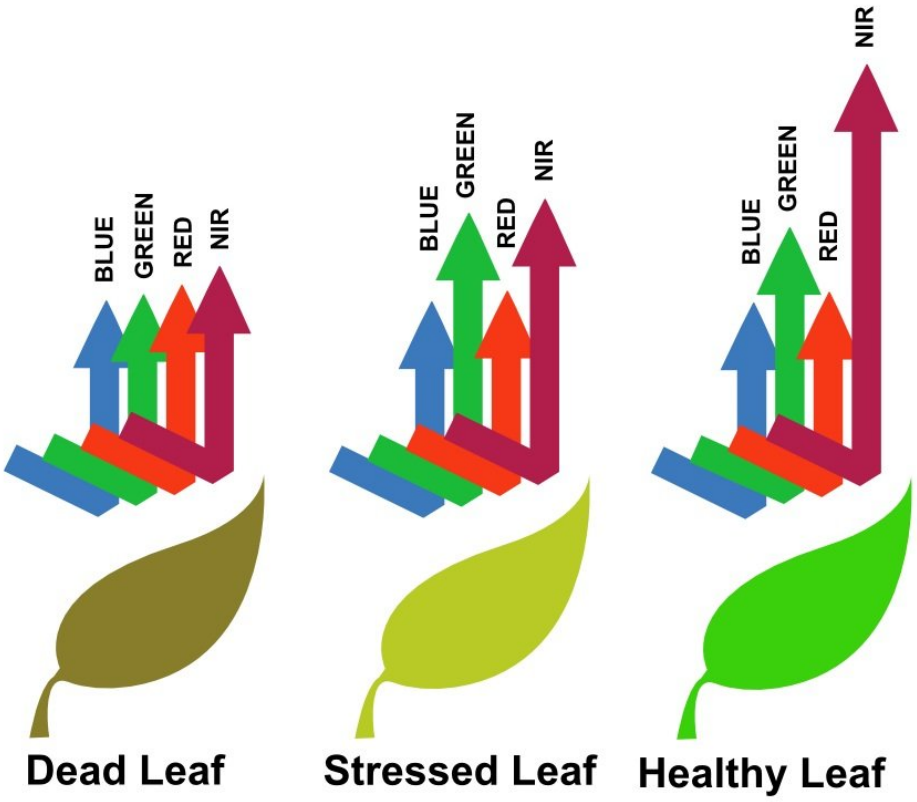


Figure 2.2: Conceptual illustration of spectral reflectance variation based on leaf health. While visible light (Blue, Green, Red) reflectance changes slightly with pigment degradation, the NearInfrared (NIR) reflectance dramatically collapses as the internal cellular structure of the leaf deteriorates from healthy to dead. [8]

Ultimately, the stark radiometric contrast between the deep VIS absorption and the high NIR scattering forms the indispensable mathematical foundation for calculating vegetation indices. Any physical interference, such as an agricultural net, that selectively distorts this precise contrast will inevitably compromise the integrity of the diagnostic algorithms used in precision agriculture.

2.1.2 UAVs as Proximal Sensing Platforms

While the physical principles of reflectance determine what needs to be measured, the acquisition platform dictates the geometric and radiometric quality of those measurements. Unmanned Aerial Vehicles (UAVs) have established themselves as the

preeminent platforms for Proximal Remote Sensing in precision agriculture. Unlike satellite systems, which are constrained by fixed orbital revisit times and susceptible to atmospheric interference (for example, cloud cover), UAVs offer unparalleled operational flexibility. They can be deployed on demand, operating within the atmospheric boundary layer directly above the canopy.

The most critical engineering metric defining the spatial resolution of a UAV optical system is the Ground Sample Distance (GSD). The GSD represents the physical distance between the centers of two consecutive pixels measured on the ground. A smaller GSD equates to a higher spatial resolution, which is imperative for heterogeneous agricultural environments like netted orchards. The theoretical GSD is fundamentally dictated by the flight altitude and the camera's optical geometry, expressed by the equation:

$$GSD = \frac{h \cdot p}{f} \tag{2.2}$$

where h is the flight altitude above ground level, p is the physical dimension of a single pixel on the camera sensor (pixel pitch), and f is the focal length of the lens. By adjusting the flight altitude h, UAVs can easily achieve sub centimeter GSDs, a level of detail unattainable by current orbital platforms.

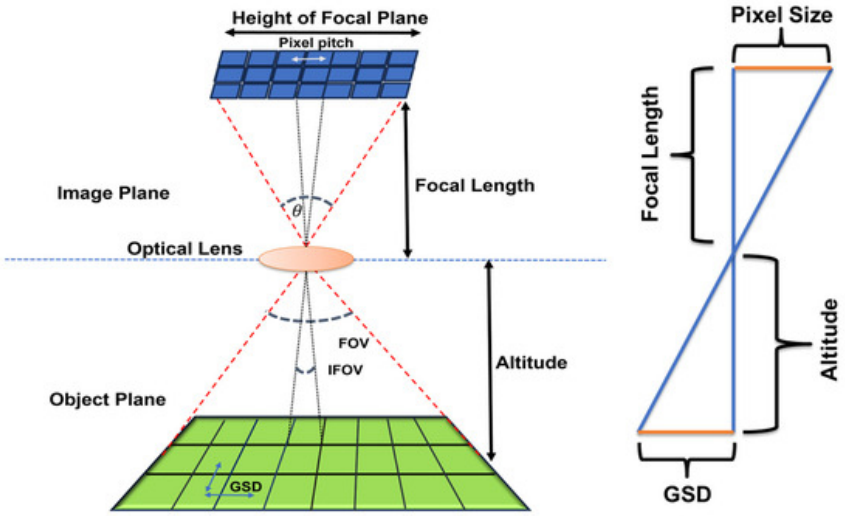


Figure 2.3: Geometric relationship defining the Ground Sample Distance (GSD). The spatial footprint of a single pixel on the ground is a direct function of the flight altitude (h), the sensor's pixel pitch (p), and the lens focal length (f). [9]

The true agronomic potential of a UAV, however, relies entirely on its payload. In the context of Proximal Remote Sensing, payload integration is governed by strict SWaP (Size, Weight, and Power) constraints. While heavy, highly calibrated hyperspectral scanners are often employed in controlled environments for rigorous baseline validations, field operations typically rely on lighter, application specific multispectral cameras. Furthermore, the state of the art in payload optimization includes innovative methods developed to extract near infrared (NIR) data directly

from standard RGB imagery. By bypassing the need for dedicated, bulky multispectral sensors, these advanced algorithmic approaches significantly reduce the cost and weight of the payload while still providing the essential spectral bands required for calculating vegetation indices.

Despite the high spatial resolution, a single aerial photograph is insufficient for rigorous agronomic analysis due to severe perspective distortions, especially at the edges of the frame. Therefore, the raw data must be processed through a complex photogrammetric pipeline utilizing Structure from Motion (SfM) algorithms. The UAV is programmed to fly over the target area following a precise grid pattern, capturing hundreds of overlapping images (typically with 75-80% frontal and lateral overlap).

The SfM algorithms mathematically match millions of keypoints across these overlapping images to reconstruct the flight geometry and generate two fundamental outputs: a radiometric orthomosaic and a dense 3D point cloud. The orthomosaic is a distortion free, georeferenced 2D map suitable for calculating indices like the NDVI on a field scale. Conversely, the dense point cloud provides crucial volumetric data regarding the canopy architecture. The precise alignment and active spatial filtering of these point clouds in dedicated spatial processing software (such as CloudCompare) are critical operations. They allow engineers to mathematically separate the vegetative canopy from the terrain and external obstacles, ensuring that the subsequent spectral analysis is exclusively focused on the biological target.

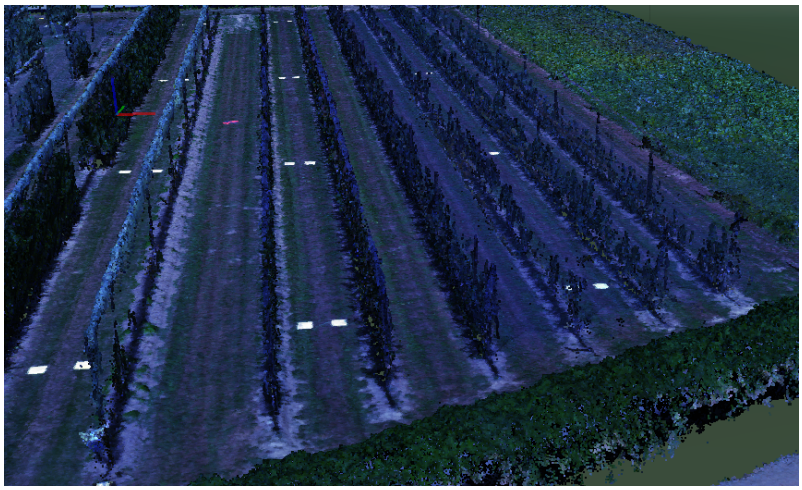


Figure 2.4: Output of the photogrammetric Structure from Motion (SfM) pipeline. The generation of a dense 3D point cloud allows for the precise geometric reconstruction of the canopy architecture, enabling spatial filtering and the isolation of the target vegetation from the background.

2.1.3 Vegetation Indices and Agronomic Applications

The raw radiometric data acquired by UAV platforms, while geometrically precise, must be mathematically transformed to extract actionable agronomic insights. This transformation is achieved through the calculation of Vegetation Indices. A vegetation index is an algebraic combination, typically a normalized ratio, of two or

more specific spectral bands. The primary engineering objective of a Vegetation Index is to maximize the sensitivity to the biophysical characteristics of the target canopy (such as biomass, leaf area index, and chlorophyll content) while minimizing the radiometric noise caused by background soil reflections, variations in solar illumination angle, and atmospheric scattering.

The most universally applied metric in precision agriculture is the Normalized Difference Vegetation Index (NDVI). Based on the physical principles of crop reflectance previously discussed, the NDVI exploits the stark radiometric contrast across the RedEdge. It is calculated by normalizing the difference between the high structural reflectance in the Near Infrared (NIR) band and the deep biochemical absorption in the Red band, according to the following equation:

$$NDVI = \frac{R_{NIR} - R_{Red}}{R_{NIR} + R_{Red}} \tag{2.3}$$

where R_{NIR} and R_{Red} represent the absolute reflectance values (or calibrated digital numbers) in their respective wavelengths. The resulting dimensionless index yields values ranging from -1 to +1. In agronomic applications, values approaching +1 indicate dense, highly vigorous vegetation with a healthy spongy mesophyll, whereas values closer to zero or negative indicate bare soil, water, or dead biomass.

While the NDVI remains the industry standard, optical remote sensing employs several complementary indices tailored to specific physiological traits. One notable variant is the Green Normalized Difference Vegetation Index (GNDVI), which substitutes the Red band with the Green band (R_{Green}, typically centered around 550 nm):

$$GNDVI = \frac{R_{NIR} - R_{Green}}{R_{NIR} + R_{Green}} \tag{2.4}$$

The GNDVI is significantly more sensitive to variations in chlorophyll concentration than the standard NDVI. It is particularly effective for assessing the nitrogen status of the canopy and detecting early stages of plant senescence, as the green reflectance changes more dynamically before structural degradation occurs.

Another critical index is the Normalized Difference Red Edge (NDRE). Instead of relying on the pure Red absorption band, the NDRE utilizes the spectral reflectance measured in the narrow RedEdge transition zone (R_{RE}, typically between 700 nm and 740 nm):

$$NDRE = \frac{R_{NIR} - R_{RE}}{R_{NIR} + R_{RE}} \tag{2.5}$$

The primary engineering advantage of the NDRE is its ability to mitigate the saturation effect. While the NDVI tends to saturate (plateau) in the presence of very dense canopies with a high Leaf Area Index (LAI), the NDRE light penetrates deeper into the canopy volume, providing a more accurate estimation of biomass and vigor in late stage crop development.

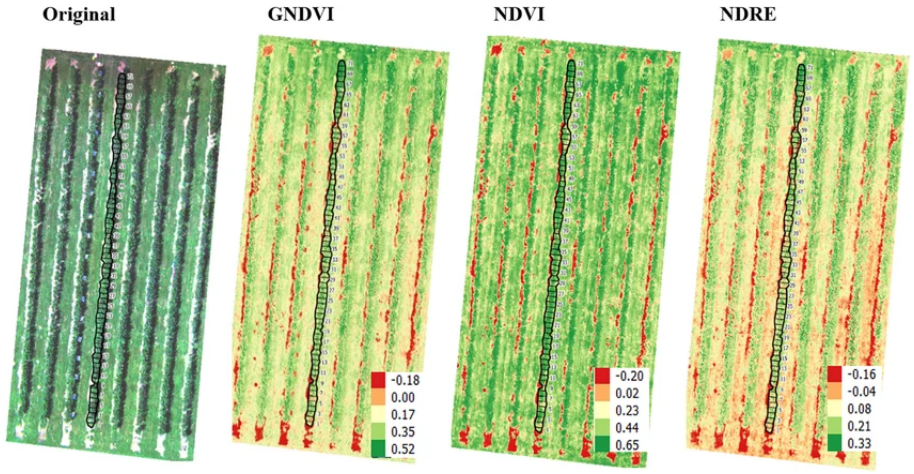
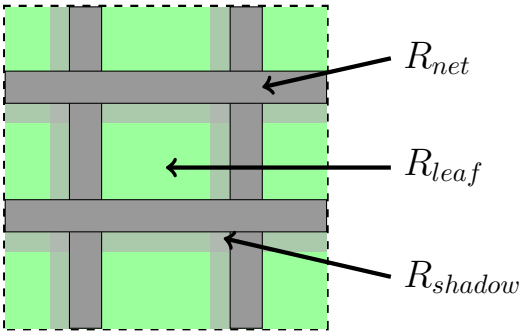


Figure 2.5: Spectral signature of healthy vegetation highlighting the specific wavelength bands utilized for calculating standard agronomic indices. The precise positioning of the Green, Red, RedEdge, and Near Infrared (NIR) regions determines the specific physiological sensitivity of GNDVI, NDVI, and NDRE. [10]

However, the mathematical robustness of all these indices relies on a fundamental assumption: the sensor is recording the pure radiometric signature of the biological target under relatively homogeneous illumination. In modern fruit production systems, this assumption is frequently violated by the presence of protective infrastructures, such as hail nets and shading screens. These micro structured physical barriers intercept the solar radiation, casting complex shadow patterns on the canopy below and physically blending their own spectral signature with that of the leaves within the sensor's Instantaneous Field of View.



$$\bar{R}_{pixel} = f_{leaf}R_{leaf} + f_{net}R_{net} + f_{shadow}R_{shadow}$$

Figure 2.6: Mixed pixel effect within the sensor's IFOV. The total reflectance ($\bar{R}_{pixel}$) is a linear combination of the sunlit canopy (R_{leaf}), the net threads (R_{net}), and the projected micro shadows (R_{shadow}), each weighted by its respective fractional area (f_i) where $\sum f_i = 1$.

This phenomenon introduces severe non linear radiometric noise into the spatial dataset. Consequently, the standard VI algorithms are systematically distorted, risking the generation of false agronomic prescriptions. Quantifying and physically

characterizing this specific radiometric disruption is the core challenge addressed in the subsequent chapters of this work.

2.2 Sensing Technologies and Platforms in Precision Agriculture

2.2.1 The Proximal Sensing Toolbox

The acquisition of actionable agronomic data relies on a diverse array of proximal sensing technologies, each engineered to capture specific geometric or biophysical properties of the crop. These instruments can be fundamentally classified into two macro categories based on their operational principle: active and passive sensors.

Active sensors emit their own electromagnetic energy and measure the backscattered signal returning from the target. The most prominent technology in this category for agricultural applications is LiDAR (Light Detection and Ranging). By rapidly emitting laser pulses and measuring the time of flight, LiDAR systems generate highly accurate, pure geometric 3D point clouds. Due to the laser's ability to partially penetrate the canopy through small gaps, LiDAR is unparalleled for assessing structural parameters such as tree volume, canopy density, and Leaf Area Index (LAI). However, LiDAR systems are entirely structural; they do not provide the radiometric data necessary for evaluating the biochemical status (for example chlorophyll or nitrogen content) of the foliage.

Conversely, passive sensors rely on external ambient illumination, primarily solar irradiance, recording the radiation reflected or emitted by the canopy. This category encompasses a wide range of optical architectures, which can be categorized by their spectral range and resolution:

- **Thermal Infrared (TIR) Cameras:** Operating in the long wave infrared spectrum (typically 8-14 μm), these sensors measure the thermal energy emitted by the crop. Thermal imaging is highly correlated with stomatal conductance and transpiration rates, making it the primary diagnostic tool for mapping water stress and optimizing precision irrigation.

- **RGB Cameras:** Standard digital sensors that capture the visible spectrum (Red, Green, Blue) with extremely high spatial resolution and at a low capital cost. While excellent for basic visual inspections, phenotyping, and geometric photogrammetry, their broad and overlapping spectral bands limit their utility for rigorous biophysical analysis.

- **Multispectral Sensors:** The current operational standard for optical precision agriculture. These cameras acquire data across 4 to 6 discrete, relatively broad spectral bands (including the critical RedEdge and NIR regions). They offer an optimal engineering compromise between payload weight, cost, and the radiometric fidelity required to compute standard vegetation indices.

- **Hyperspectral Sensors:** The radiometric "gold standard." Unlike multispectral systems, hyperspectral scanners capture the electromagnetic spec-

trum across hundreds of narrow, contiguous spectral bands (often with a Full Width at Half Maximum, FWHM, of just a few nanometers). This continuous measurement generates a complex spatial spectral data structure known as a "hypercube," allowing for the reconstruction of an unbroken reflectance curve for every single pixel.

While hyperspectral technology provides the ultimate diagnostic capability, capable of detecting minute radiometric anomalies, its deployment remains highly restricted. The exorbitant hardware costs, the immense volume of data generated, and the advanced computational complexity required for processing relegate hyperspectral sensors primarily to the domain of high level academic research and laboratory grade validations, rather than widespread commercial deployment.



(a) LiDAR sensor [11] (b) Multispectral camera [12] (c) Hyperspectral scanner [13]

Figure 2.7: Examples of standard proximal sensing hardware utilized in precision agriculture operations. From left to right: an active LiDAR sensor for geometric 3D reconstruction, a passive multispectral camera for standard vegetation indices, and a passive hyperspectral line scanner for high fidelity radiometric analysis.

2.2.2 Deployment Kinematics: Terrestrial and Aerial Platforms

The agronomic efficacy of any proximal remote sensing payload is intrinsically dependent on the kinematic and geometric characteristics of its deployment vector. The physical platform dictates the sensor's optical perspective, the achievable spatial resolution, and the temporal flexibility of the acquisition campaign. In modern precision agriculture, these deployment vectors are fundamentally divided into terrestrial systems and aerial platforms, each presenting distinct engineering advantages and geometric limitations.

Terrestrial deployment has traditionally relied on tractor mounted sensors. These systems are highly robust and designed for real time edge computing. They often integrate directly with the vehicle's ISOBUS network to execute Variable Rate Applications (VRA) dynamically. From an optical engineering standpoint, tractor mounted sensors operate from a lateral or slightly oblique perspective. While this geometry is optimal for scanning the outer canopy perimeter or evaluating lower trunk parameters, it suffers from severe self occlusion in dense orchard architectures

and completely fails to map the upper canopy structure. Furthermore, the reliance on heavy machinery is heavily constrained by ground trafficability and contributes to detrimental soil compaction.

To mitigate mechanical compaction and increase operational autonomy, the deployment of Unmanned Ground Vehicles (UGVs) and agricultural rovers is gaining traction. Utilizing Simultaneous Localization and Mapping (SLAM) algorithms, often fusing LiDAR and stereoscopic data, UGVs navigate autonomously between rows, providing highly repeatable, under canopy radiometric measurements. Nevertheless, their Field of View (FOV) remains strictly limited to the lateral cross section of the vegetative wall.

For comprehensive, field scale spatial analysis, Unmanned Aerial Vehicles (UAVs) have emerged as the definitive vector. UAVs geometrically decouple the optical payload from the ground, eliminating trafficability constraints and providing a strictly nadiral (top down) measurement perspective. By programming precise flight altitudes and overlapping grid trajectories in three dimensional space, engineers can deterministically control the Ground Sample Distance (GSD) and generate continuous spatial models of the entire orchard canopy.

Crucially, however, this nadiral acquisition geometry represents a severe vulnerability in modern fruit production systems equipped with protective infrastructures. Because the UAV observes the canopy strictly from above, its optical path is physically intercepted by overarching hail nets. This top down interception is the fundamental geometric catalyst for the mixed pixel effect. The structural threads and the micro shadows cast by the netting inevitably occlude the underlying biological target, introducing a systematic radiometric distortion that standard UAV processing pipelines cannot autonomously resolve.



(a) Unmanned Ground Vehicle (UGV) [14]



(b) Unmanned Aerial Vehicle (UAV) [15]

Figure 2.8: Autonomous deployment platforms utilized in precision agriculture. (a) A UGV designed for sub canopy navigation, operating with a lateral optical perspective. (b) A UAV platform engineered for field scale nadiral data acquisition, providing top down radiometric mapping.

2.2.3 Technology Adoption and Cost Effective Innovations in the Italian Context

Despite the proven agronomic benefits of proximal remote sensing and UAV deployment, the widespread commercial adoption of these technologies remains structurally uneven. In the Italian agricultural landscape, which is predominantly characterized by highly fragmented land ownership, specialized micro farms, and deep rooted traditional practices, the transition toward precision agriculture faces significant socioeconomic and technical barriers. The primary deterrent is the initial capital expenditure required for dedicated, high fidelity optical hardware, such as native multispectral or hyperspectral sensors. Furthermore, the steep learning curve associated with processing complex spatial spectral data into actionable agronomic prescriptions often discourages end users.

However, when these monitoring systems are successfully integrated, the agronomic and economic outcomes are highly positive and easily quantifiable. For traditional agricultural enterprises, adopting a data driven approach proves to be a highly convenient operational solution. It enables the transition from uniform field treatments to site specific management, optimizing the distribution of fundamental inputs such as water, fertilizers, and phytosanitary products. This targeted approach not only maximizes crop yield and quality but also drastically reduces operational waste and environmental impact. Consequently, the integration of proximal sensing architectures represents a strategic and highly beneficial upgrade even for conventional, smaller scale orchards.

To bridge the technological gap and facilitate market penetration, the Agritech sector is increasingly adopting a "Sensing as a Service" paradigm coupled with automated cloud based analytics. Rather than requiring individual farms to purchase expensive sensor payloads and master complex photogrammetric software, specialized contractors acquire the field data. The raw spectral datasets are subsequently uploaded to cloud architectures that automatically process the information, delivering simplified, ready to use prescription maps directly to the farmer's mobile device or tractor terminal. This structural shift from capital expenditure to accessible operational services democratizes precision agriculture, allowing traditional growers to leverage advanced agronomic insights without necessitating in house engineering expertise.

2.2.4 High Resolution Radiometry and the Hyperspectral Approach

While commercial multispectral solutions provide valuable data for general agronomic management, the scientific characterization of complex optical phenomena requires superior radiometric precision. To mathematically isolate the spectral interference caused by protective nets from the actual biological signature of the underlying canopy, researchers must deploy advanced hyperspectral sensors.

These instruments predominantly utilize a scanner architecture. Unlike standard snapshot cameras that capture an entire two dimensional spatial matrix in a single instant, a scanner sensor acquires spatial information strictly along a single

narrow line. The incoming light passes through a physical slit and is dispersed by a diffraction grating into hundreds of contiguous spectral bands. This optical process creates a data matrix for every acquisition frame, where one dimension represents the spatial pixels along the line and the other dimension represents the spectral wavelengths. To generate the final complete spatial image, the sensor or the target must move continuously at a strictly constant velocity, sequentially scanning the area line by line. In the context of this research, a Specim FX10 hyperspectral scanner is employed as the primary analytical instrument. This device operates specifically within the Visible and Near Infrared (VNIR) spectrum. Its extreme spectral resolution enables the extraction of a continuous unbroken reflectance curve for every single spatial pixel. This advanced level of detail is fundamental to precisely quantify the shading effect and the radiometric distortions introduced by agricultural nets. Furthermore, to guarantee the scientific validity of the acquired hypercubes, rigorous radiometric calibration is performed before every scan using optimal white reference panels and dark current measurements. This procedure converts the raw digital numbers recorded by the sensor into absolute reflectance values, establishing a reliable baseline for the subsequent field scale UAV modeling.

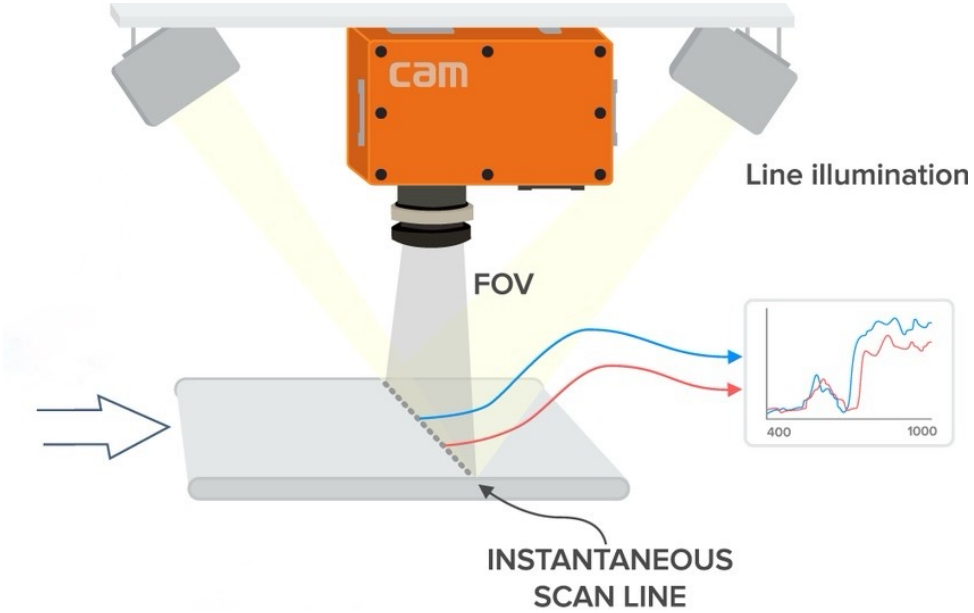


Figure 2.9: Conceptual schematic of the pushbroom acquisition principle utilized by the Specim FX10 sensor. The optical system captures spatial information strictly along a single slit and disperses the incoming light into continuous spectral bands. A complete three dimensional hypercube is generated by physically translating the sensor or the target area at a strictly constant velocity. [16]

2.3 Optical Properties and Photobiology under Netted Environments

The scientific community has increasingly documented how the optical properties of protective infrastructures negatively impact the radiometric fidelity of remote sensing platforms. Current literature consistently reports that the interposition of an agricultural net introduces a significant bias in standard monitoring workflows. Crucially, this spectral distortion is the complex result of both the physical optical interference of the netting material and the consequent photobiological adaptation of the underlying plant canopy.

From a purely optical perspective, researchers have observed a pronounced attenuation of reflectance values in the near infrared region. Because the structural threads physically occlude the target, they absorb and scatter the incoming radiation before it reaches the sensor, artificially depressing the signal. Simultaneously, the selective filtering of the visible spectrum, particularly the red region, varies heavily depending on the polymer pigmentation of the net.

However, literature also highlights that the spectral distortion is compounded by the biological response of the vegetation. Plants cultivated under these modified radiometric environments adapt to the increased presence of diffuse light and the overall shading factor by altering their leaf structure and pigment concentrations. This photobiological acclimation means the intrinsic spectral signature of a protected canopy is fundamentally different from that of an open field crop.

The mathematical combination of the optical occlusion caused by the net and the biological adaptation of the leaves leads to a systematic underestimation of essential vegetative metrics. Numerous field trials demonstrate that the NDVI extracted from netted orchards is consistently miscalculated. From an agronomic engineering standpoint, failing to disentangle the physical optical interference of the net from the actual biological status of the plant directly compromises the reliability of prescription maps and undermines the effectiveness of precision agriculture interventions.

Chapter 3

Materials and Methods

3.1 Indoor Laboratory Experimentation

The first phase of the research was conducted in a controlled laboratory environment to systematically isolate and quantify the optical behavior of agricultural shading nets. The primary objective was to obtain a high resolution spectral characterization, successfully decoupling the radiometric measurements from unpredictable environmental variables such as solar zenith angle fluctuations, atmospheric scattering, and complex canopy architecture.

To practically execute this analysis, the laboratory workflow was divided into two distinct operational sessions. The first session was strictly dedicated to setup optimization. The specific activities involved mounting a hyperspectral line scanner on a motorized translation stage and capturing data at various physical elevations between the lens, the netting material, and the background. This physical calibration was performed to identify the exact geometric configuration capable of generating a diffused light field, thereby correctly replicating a nadir airborne perspective.

Following the optical validation, the second session focused on the core data acquisition using the optimized setup. The operational steps consisted of scanning a definitive selection of commercial nets with the hyperspectral camera to extract their continuous spectral signatures. In parallel, point based measurements were manually acquired using a portable spectroradiometer positioned both above the net canopy and directly beneath it. This dual sensor deployment was executed to continuously cross validate the instruments, providing a highly reliable and geometrically accurate baseline for the subsequent multispectral simulations.

3.1.1 Experimental Setup and Instrumentation

Spectral acquisitions were predominantly performed utilizing a Specim FX10 hyperspectral camera (Specim, Spectral Imaging Ltd., Oulu, Finland). This push broom sensor operates in the Visible and Near Infrared (VNIR) spectral range, specifically between 400 nm and 1000 nm, allowing for the continuous capture of hundreds of narrow contiguous spectral bands.

The setup was integrated into a motorized linear translation stage (Specim Scanner System), allowing the target to move at a constant speed beneath the stationary

sensor. The camera was securely mounted facing downwards (nadir configuration) at a distance of 28 cm from the target plane, simulating the typical viewing angle of a UAV during an aerial survey. To guarantee a constant and repeatable radiometric environment, the illumination was provided by symmetrical broadband linear halogen lamps. These lamps were specifically selected to ensure a continuous and uniform emission across the entire VNIR spectrum, minimizing directional shadows on the target surface.

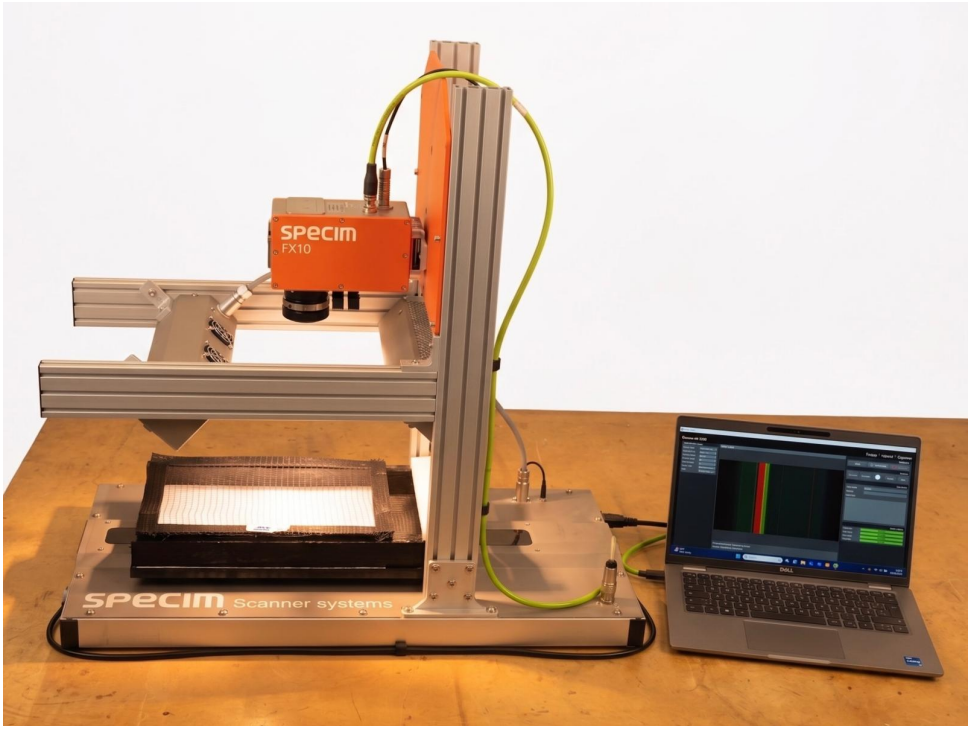
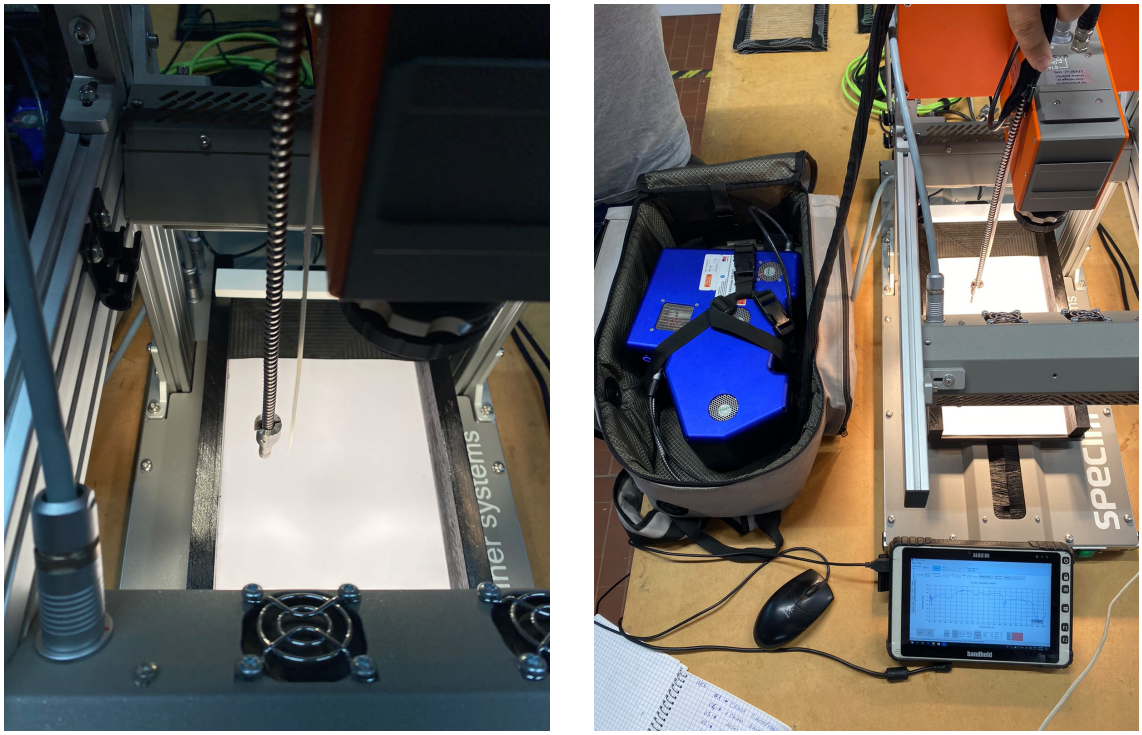


Figure 3.1: Complete overview of the Specim FX10 experimental setup, showing the hyperspectral camera mounted on the motorized linear translation stage, the sample area, the halogen illumination system, and the control laptop.

Alongside the hyperspectral camera, an RS-5400 portable spectroradiometer was introduced to perform precise sensor cross validation. While the Specim FX10 provided continuous spatial and spectral datacubes that require computational matrix processing, the RS-5400 processes the radiometric signal natively. The instrument captures the reflected light through a fiber optic probe and disperses the continuous wavelengths across internal diode arrays. Utilizing its integrated hardware and software, it performs a real time radiometric calibration by computing the exact ratio between the target's absolute radiance and a previously stored white reference. This hardware driven pipeline instantly generates a fully calibrated spectral reflectance curve for each discrete measurement point, outputting a ready to use dataset. A detailed description of its specific deployment is provided in the subsequent sections detailing the second session's workflow. For all acquisitions, a standard white paper sheet was positioned directly beneath the shading nets to serve as a uniform, highly reflective background. This setup isolated the specific optical behavior of the polymeric threads, allowing for a precise evaluation of light diffusion and shading

effects.

Prior to the net acquisitions, a rigorous radiometric calibration protocol was executed. Raw digital numbers (DN) were converted into absolute reflectance values by acquiring a bright reference using a standard white calibration panel (representing 100% reflectance) and a dark reference (acquired with the camera lens completely covered to account for sensor thermal noise). The specific data aggregation protocols, including the mathematical extraction of the spectral curves from the spatial regions of interest and the exact number of physical replicates acquired for both sensors, are detailed during the first validation phase (Section 3.3).



(a) Detail of the measurement probe. (b) Overview of the test bench.

Figure 3.2: Configuration of the RS-5400 spectral analysis system. (a) A close up detail of the measurement probe and the black/white calibration standard in position on the motorized stage. (b) An overview of the complete test bench, including the spectrometer unit (housed in the backpack), the scanning device, and the user interface on the handheld tablet.

3.1.2 Sample Characterization: The Shading Nets

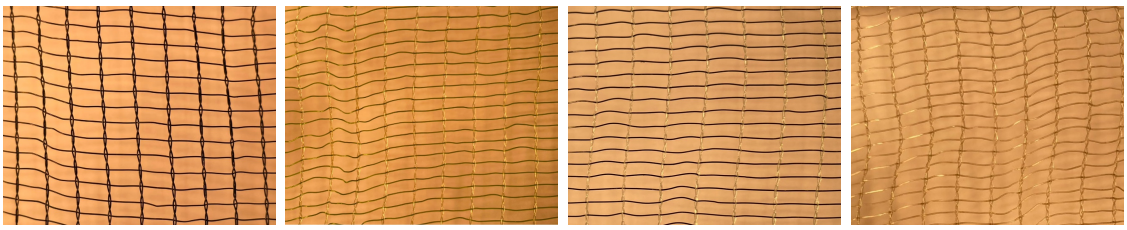
To comprehensively evaluate the radiometric impact of different protective covers, five commercially available agricultural anti-hail nets were selected for the validation session (nets 01, 02, 03, 04, and 05). Subsequently, a refined subset consisting of nets 02, 03, 05, and 06 served as the primary experimental group for the core data processing and final performance evaluation, as they yielded the definitive results discussed hereafter. These nets differ significantly in color and thread arrangement,

representing a diverse cross section of the solutions currently adopted in modern orchards.

Table 3.1 summarizes the primary physical properties of the selected samples, while the weaving patterns and visual appearance of the four nets used in the second session are illustrated in Figure 3.3.

Table 3.1: Visual and material characteristics of the evaluated shading nets.

ID	**Color / Type**	**Material**
Net 01	Black Green (Bicolor)	HDPE
Net 02	Black	HDPE
Net 03	Light Green	HDPE
Net 04	Transparent (Crystal)	HDPE
Net 05	Black Transparent (Bicolor)	HDPE
Net 06	Transparent	HDPE



(a) Net 02 (b) Net 03 (c) Net 05 (d) Net 06

Figure 3.3: Macro photographs detailing the visual appearance and weaving patterns of the four agricultural shading nets evaluated in the second session.

All samples are manufactured from High Density Polyethylene (HDPE) employing a typical leno weave pattern designed for anti-hail applications.

3.2 Conceptual Optical Model and Radiometric Nomenclature

To ensure absolute clarity and consistency throughout the methodological description, this section establishes the fundamental optical pathways and the radiometric nomenclature adopted for the core laboratory experiments. The following conceptual model mathematically isolates the complex interactions between the artificial illumination source, the physical structure of the anti-hail net, the highly reflective background, and the dual sensor setup employed in this study.

By standardizing these terms, the subsequent data processing pipelines and spectral simulations can be described using precise, predefined acronyms, effectively streamlining the technical narrative. Figure 3.4 provides a comprehensive visual summary of all the isolated radiometric components.

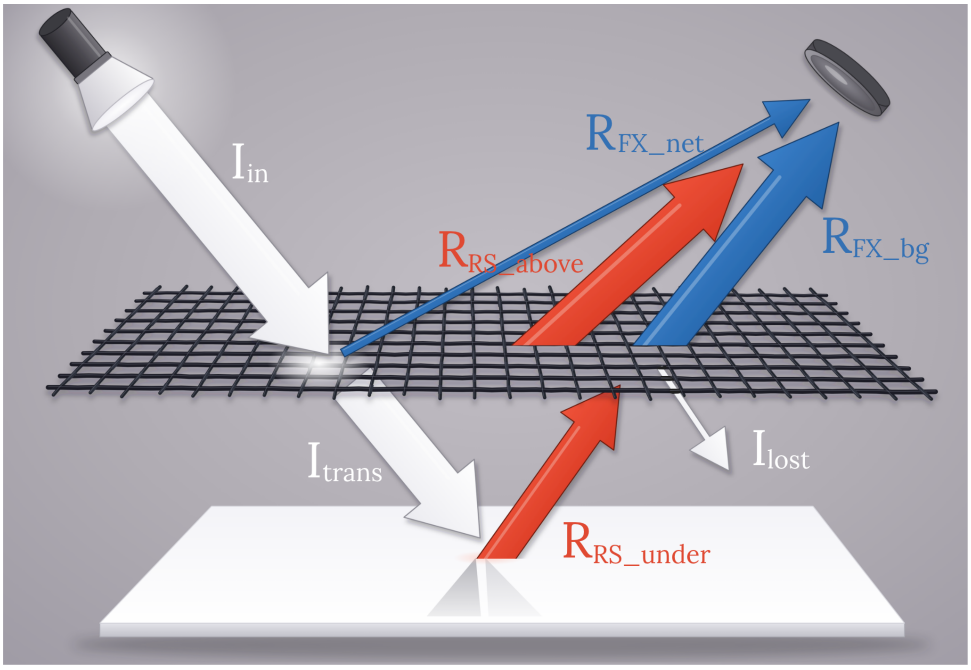


Figure 3.4: Conceptual optical model detailing the directional light pathways and the distinct radiometric signals captured by the dual sensor setup. White arrows represent the illumination fluxes, blue arrows indicate the high resolution spatial measurements acquired by the Specim FX10 hyperspectral scanner, and red arrows denote the macroscopic point measurements recorded by the RS-5400 spectroradiometer.

Based on the geometric configuration illustrated above, the radiometric components are rigorously defined as follows. To address the distinction between contextual physical phenomena and empirical data, the parameters are separated into theoretical illumination pathways and actively measured optical signals:

Theoretical Illumination Fluxes (Contextual)
These components (represented by white arrows) describe the physical behavior of the light. They are not mathematically quantified in the subsequent analytical phases, but are explicitly defined to provide the fundamental conceptual framework required to understand the origin of the measured signals:

- I_{in} (Incident Irradiance): The primary broadband radiation generated by the halogen illumination system that strikes the upper surface of the protective net.
- I_{trans} (Transmitted Irradiance): The fraction of incident radiation that physically passes through the mesh openings or is forward scattered by the polymeric threads, successfully reaching the background plane.
- I_{lost} (Lost or Scattered Irradiance): The radiant energy that is absorbed by the polymer material or scattered outside the field of view of the sensors, thus not contributing to the useful optical signal.

Hyperspectral Scanner Measurements (Specim FX10)

- R_{FX_net}: The isolated spectral reflectance captured by the line scanner corresponding exclusively to the pure pixels of the solid structural threads.

- R_{FX_bg}: The isolated spectral reflectance captured by the line scanner corresponding exclusively to the mesh openings (the pure background pixels), which are inherently influenced by the spatial shading effect of the overhead structure.

Spectroradiometer Point Measurements (RS-5400)

- R_{RS_above}: The macroscopic point based measurement acquired with the optical probe held perpendicular at a fixed distance of 10 cm above the net structure. Its conical field of view integrates the combined reflectance of the structural threads and the visible underlying background.

- R_{RS_under}: The targeted measurement acquired by positioning the optical probe at a distance of approximately 1 cm directly beneath the net mesh (just above the background sheet), quantifying the absolute radiometric response of the target when illuminated exclusively by the filtered and diffused transmitted irradiance (I_{trans}).

3.3 First Laboratory Session: Optical Setup Validation

The initial laboratory session was designed to validate the optical configuration and determine the most reliable setup for hyperspectral acquisition using the Specim FX10 scanner. The primary objective was to identify the geometric and focal configuration that minimized the spatial variance of the background and the optical noise introduced by the shadows of the threads. For this methodological validation, all five commercial shading nets (Nets 01, 02, 03, 04, and 05) were evaluated.

To comprehensively assess the optical behavior, acquisitions were performed under three distinct configurations. In all setups, the total distance between the hyperspectral scanner and the white background plane was maintained at a constant 28 cm:

1. **Contact Setup:** The net was positioned at a distance of 1 cm from the white background, representing the physical thickness of the mounting frame.

2. **Raised Setup (Background in Focus):** The net was elevated to a distance of 5 cm from the background. The optical focus of the Specim FX10 was locked precisely on the white background plane.

3. **Raised Setup (Net in Focus):** The net was maintained at the 5 cm elevation, but the scanner's focus was shifted entirely onto the polymeric threads, leaving the white background intentionally out of focus.

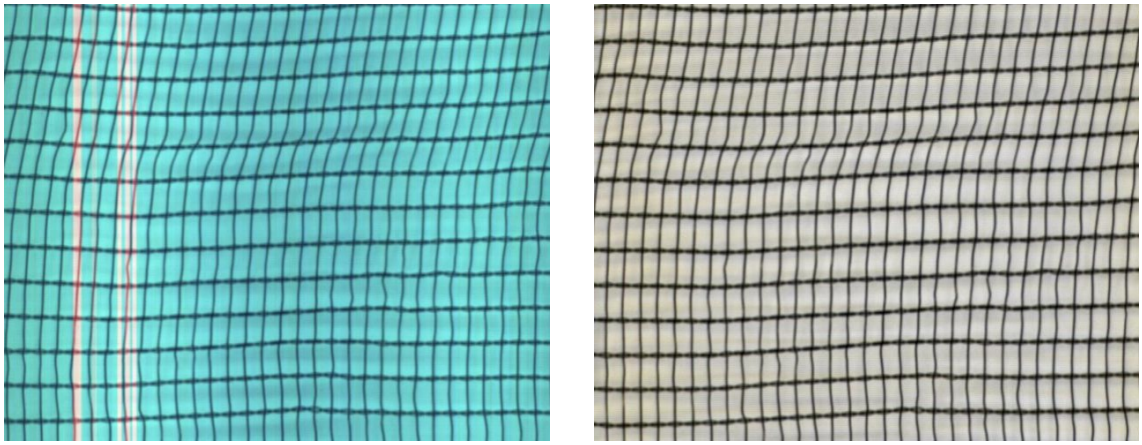
The volume of raw hyperspectral data generated by the Specim FX10 camera required a robust and automated computational pipeline. The entire data processing workflow was developed and executed within the MATLAB environment.

The first fundamental step consisted of the radiometric calibration of the raw datacubes. To eliminate sensor specific artifacts and account for the spectral distribution of the halogen illumination, the raw digital numbers (DN) were converted into absolute reflectance values (R) for each specific wavelength (λ) using the following standard empirical line method:

$$R_\lambda = \frac{DN_\lambda - D_\lambda}{W_\lambda - D_\lambda} \tag{3.1}$$

where W_λ represents the white reference and D_λ is the dark reference acquired with a closed shutter to subtract the thermal noise of the sensor. Instead of relying on a standard external calibration panel, the highly reflective white paper serving as the background was directly utilized as the white reference (W_λ). Preliminary empirical tests confirmed that this approach yielded equivalent radiometric results while significantly streamlining the data processing workflow for subsequent analyses.

To visually demonstrate the effectiveness of this radiometric calibration, Figure 3.5 illustrates a comparison between a raw, uncalibrated hyperspectral frame and the corresponding processed reflectance image.

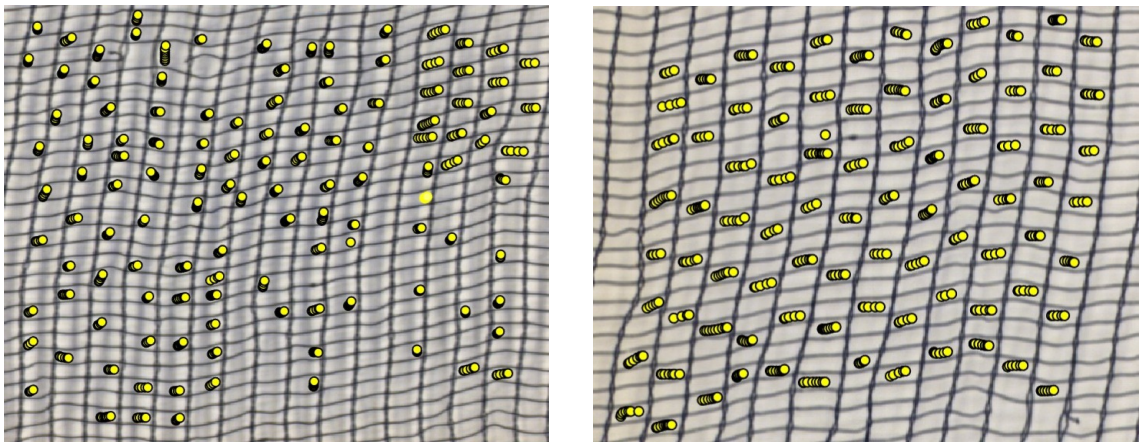


(a) Raw Uncalibrated Image (DN) (b) Calibrated Reflectance Image

Figure 3.5: Visual comparison illustrating the radiometric calibration process in MATLAB. (a) Raw hyperspectral frame before correction, affected by illumination non uniformity; (b) Calibrated reflectance image utilizing the white background and dark references.

Following the radiometric calibration, rather than applying a global spatial mask, a targeted manual sampling procedure was executed. Multiple small polygonal regions were carefully delineated exclusively within the mesh openings. This meticulous selection ensured that only the underlying background pixels were sampled, actively excluding the solid polymeric threads from the calculation. To illustrate the impact of the different geometric configurations on the shadow's spatial distribution,

Figure 3.6 provides a comparison of this manual selection process for Net 02 under Setup 1 and Setup 3.



(a) Setup 1: Contact (1 cm distance) (b) Setup 3: Raised (5 cm, Net in Focus)

Figure 3.6: Comparison of the manual sampling procedure implemented in MATLAB for Net 02. Multiple polygonal regions (highlighted in yellow) were selected strictly within the mesh openings to isolate the background. The comparison highlights the sharp, distinct shadows in Setup 1 (a) versus the more diffused, uniform radiometric field in Setup 3 (b).

For these specifically selected regions, the Mean Reflectance and the Standard Deviation (σ) were computed across the sampled pixels for every wavelength in the VNIR range (400-1000 nm). To ensure complete methodological transparency, the core data extraction and statistical aggregation for this and all subsequent spatial analyses were executed using a dedicated MATLAB routine. Once the spatial regions are defined, the algorithm reshapes the 3D hyperspectral datacube into a two dimensional array and applies the generated boolean mask to isolate exclusively the selected target pixels:

Listing 3.1: Data extraction and statistical aggregation of the spectral signature over spatial pixels.

```
% Flatten the 3D datacube and the boolean spatial mask
matrice_piatta = reshape(matrice_dati, righe * colonne, bande);
maschera_piatta = maschera_totale(:);

% Extract only the manually selected pixels
% (N pixels x B bands)
pixel_selezionati = matrice_piatta(maschera_piatta, :);

% Calculate the spatial mean and standard deviation for each band
media_spettro = mean(pixel_selezionati, 1)';
dev_std_spettro = std(pixel_selezionati, 0, 1)';
```

As demonstrated in the code snippet, the algorithm generates an $N \times B$ data matrix, where N represents the total number of manually sampled spatial pixels and B represents the number of discrete spectral bands. The representative spectral signature of the target is mathematically defined by computing the column wise mean of this matrix, effectively calculating the average absolute reflectance across all N physical pixels for each specific wavelength.

Crucially, the statistical variance is derived directly from spatial heterogeneity rather than repeated temporal measurements. For each discrete spectral band λ, the unbiased sample standard deviation (σ_λ) evaluates the exact population of N spatial pixels according to the following mathematical formulation:

$$\sigma_\lambda = \sqrt{\frac{1}{N-1}\sum_{i=1}^{N}(R_{i,\lambda} - \mu_\lambda)^2} \tag{3.2}$$

where $R_{i,\lambda}$ represents the absolute reflectance of the i-th spatial pixel at wavelength λ, and μ_λ represents the spatial mean reflectance for that same band. Calculating this spatial standard deviation was the primary objective of this validation session. By mathematically quantifying how much the individual spatial pixels deviate from the mean reflectance at any given wavelength, it served as a critical metric to evaluate the spatial homogeneity of the shaded light field. By comparing the variance across the three setups, it was possible to identify which geometric configuration produced the most uniformly diffused shadow.

3.4 Second Laboratory Session: Sensor Cross Validation

3.4.1 Acquisition Protocol and Dual Sensor Sampling

The second laboratory session focused exclusively on the definitive subset of shading covers (Nets 02, 03, 05, and 06), utilizing the optimized raised geometric configuration established during the preliminary validation. The primary objective was to acquire highly reliable radiometric data by synchronizing the high resolution spatial scans of the Specim FX10 with the point based spectral readings of the RS-5400 spectroradiometer.

To guarantee the absolute invariability of the artificial halogen illumination, the dual sensor acquisitions were executed strictly sequentially for each physical sample. Initially, the hyperspectral line scanner performed two independent spatial acquisitions across different sections of the net. Capturing two distinct spatial datacubes per sample ensured a broader physical representation of the weaving pattern, allowing for a more robust mathematical average during the subsequent data processing phase.

Immediately following the hyperspectral scans, the RS-5400 optical probe was deployed on the same exact test bench. To ensure the absolute radiometric accuracy of the point based measurements, the white reference calibration of the spectroradiometer was strictly performed at two different elevations. A standard highly reflec-

tive calibration panel was recorded both at the upper focal plane corresponding to the physical net structure, and at the lower plane corresponding to the background sheet.

To adequately account for the intrinsic spatial heterogeneity of the polymeric mesh, a rigorous manual sampling strategy was applied to the spectroradiometer. The fiber optic probe was systematically positioned to record five distinct measurement points directly above the net canopy (R_{RS_above}) and five discrete points directly beneath it, targeting the filtered light on the white background (R_{RS_under}).

The individual spectral readings from these five points were subsequently exported as discrete data files and processed utilizing a dedicated MATLAB routine. The computational aggregation consisted of extracting the calibrated relative reflectance from each file to populate a unified data matrix. By applying a row wise arithmetic mean across this matrix, the algorithm effectively integrated the five conical fields of view into a single, robust spectral signature representing the macroscopic radiometric flux for the evaluated network sample.

3.4.2 Geometric Fractional Area and Color Segmentation

To mathematically quantify the physical area occupied by the solid network threads and to differentiate multi colored weaving patterns, a custom computational pipeline was developed within the MATLAB programming environment. Since the radiometric calibration is executed in a preceding processing step, this specific algorithm focuses entirely on the spatial segmentation of the calibrated datacubes.

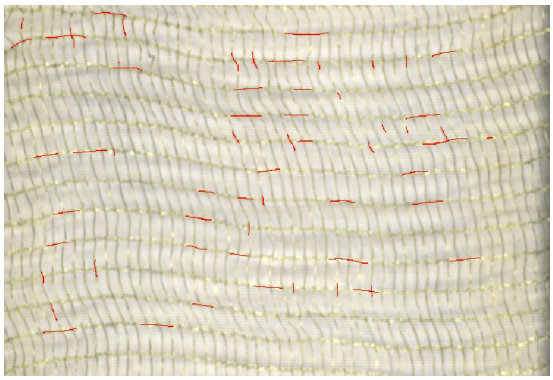
To circumvent the optical noise and false positives often associated with automated global thresholding, the segmentation relies on a supervised classification approach driven by a graphical user interface. Through this interface, the operator manually selects multiple reference samples across the image to establish the reference training data. As illustrated in Figure 3.7, the user delineates specific regions by drawing freehand reference lines precisely over the solid structural threads and placing polygonal markers strictly within the underlying background holes. Once these specific regions are drawn, the custom MATLAB script extracts the absolute reflectance values of all the manually selected pixels across the entire hyperspectral wavelength range, generating a pure pixel matrix. The representative spectral signatures and the corresponding spatial standard deviation vectors for these training classes were then mathematically extracted applying the identical matrix aggregation protocol and statistical formulation previously defined in Section 3.3. Utilizing these extracted and statistically defined spectral signatures, the MATLAB algorithm automatically recognizes and classifies the remaining pixels within the designated area. The software evaluates the radiometric profile of every unclassified pixel and assigns it to the most spectrally similar reference class. This machine driven recognition effectively separates the entire spatial domain into mutually exclusive boolean masks representing the physical network and the empty spaces. For heterogeneous bi colored nets, this identical supervised logic is extended by providing distinct manual samples for each different polymer pigmentation.

Once the automated recognition phase is complete, the script computes the precise spatial fraction for each specific target class. The physical percentage is math-

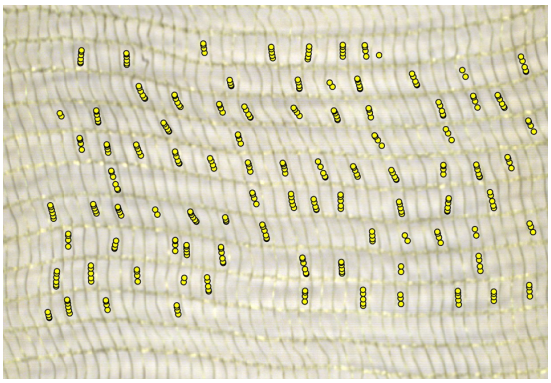
ematically derived by computing the ratio between the pixel count of the classified target and the total number of valid pixels within the analyzed section:

$$f_c(\%) = \left(\frac{P_c}{P_{total}} \right) \times 100$$

where P_c is the number of pixels automatically assigned to the specific class c, and P_{total} is the total number of pixels evaluated. These highly accurate geometric fractions are subsequently exported to serve as the exact weighting coefficients required for the mixed pixel optical simulation in the final analytical phase.



(a) Manual sampling of the solid threads



(b) Manual sampling of the background holes

Figure 3.7: Supervised spatial sampling procedure implemented in MATLAB, demonstrated on the transparent Net 06. The operator manually identifies pure pixels for both the physical netting material (a) and the empty background spaces (b). These manual selections act as training data for the subsequent automatic spatial classification.

3.4.3 Radiometric Cross Validation Workflows

To mathematically demonstrate the reliability of the entire experimental setup, a comprehensive radiometric cross validation pipeline was engineered in MATLAB. This workflow systematically compared the high resolution spatial data from the Specim FX10 with the point based reference measurements generated by the RS-5400 spectroradiometer.

Because the two instruments operate with fundamentally different spectral resolutions and sensor architectures, a preliminary spectral alignment protocol was implemented. The MATLAB algorithm utilized a linear interpolation function to mathematically resample the raw RS-5400 spectral signatures, mapping them precisely onto the specific wavelength bands of the Specim FX10 sensor (400-1000 nm). Following this spectral synchronization, the validation proceeded through four distinct analytical phases.

Phase A: Baseline Sensor Alignment
Before evaluating the shading nets, an initial calibration check was performed to ensure both instruments established the same radiometric baseline. The bare white

calibration panel was measured by both sensors. Within the MATLAB interface, the operator delineated a large rectangular Region of Interest (ROI) over the hyperspectral datacube to extract a robust spatial average of the white background. To strictly compare the spectral shape and eliminate any discrepancies in absolute irradiance intensity, a peak normalization algorithm was applied. Both the Specim and the interpolated RS-5400 spectral curves were mathematically scaled to a maximum relative value of 100. This phase successfully confirmed the absence of instrumental bias between the two sensors.

Phase B: Macroscopic Field of View Validation
This phase aimed to validate the optical behavior from a macroscopic perspective, simulating the mixed signal typically captured by a high altitude airborne sensor. The point based measurement acquired by the RS-5400 positioned directly above the net canopy (R_{RS_above}) was compared against the hyperspectral data. To perfectly replicate the macroscopic field of view of the spectrometer probe, the operator drew a single, expansive rectangular ROI over the Specim datacube. This large bounding box deliberately encompassed both the solid structural threads and the underlying empty mesh openings, generating a true spatial average of the entire complex optical system.

Phase C: Transmitted Shading Validation
To validate the radiometric alteration of the light successfully transmitted through the canopy, the RS-5400 measurement acquired beneath the net (R_{RS_under}) was utilized. Conversely to Phase B, the spatial extraction from the Specim datacube required surgical precision. Instead of a single broad rectangle, the operator manually sampled multiple small polygonal regions strictly within the empty holes of the mesh. This targeted sampling effectively isolated the background pixels, calculating the mean spectral signature of the shaded light and proving that both sensors accurately recorded the identical transmitted radiometric flux.

Phase D: Mixed Pixel Equation Validation
The final validation phase constituted the definitive mathematical proof of the mixed pixel optical model. The objective was to computationally reconstruct the real mixed macroscopic signal (extracted in Phase B) using a theoretical algebraic summation. Within the dedicated MATLAB interface, the operator sampled multiple isolated sections of the pure polymer threads (R_{FX_net}) and multiple isolated sections of the pure background (R_{FX_bg}). For heterogeneous bi colored samples, distinct samples were acquired for each pigment.

These pure radiometric endmembers were then mathematically weighted using the exact geometric fractional areas (f_c) calculated during the spatial segmentation phase (Section 3.4.2). The software computed the simulated macroscopic reflectance ($R_{simulated}$) at each wavelength λ through the following linear mixture equation:

$$R_{simulated}(\lambda) = \sum_{c=1}^{n} \left(R_c(\lambda) \times \frac{f_c}{100} \right) + \left(R_{FX_bg}(\lambda) \times \frac{f_{bg}}{100} \right)$$

where R_c and f_c represent the reflectance and spatial percentage of the specific thread classes, while f_{bg} represents the percentage of the empty background spaces. By demonstrating that this simulated curve perfectly matched the real macroscopic

curve extracted via the large bounding box, the theoretical methodology for evaluating remote sensing distortions over netted environments was definitively validated.

3.5 Spectral Aggregation and Multispectral Simulation

Following the physical laboratory acquisitions, the subsequent phase focused entirely on data processing. The core activities involved developing a custom computational pipeline in MATLAB to spatially segment the structural threads of the nets, extract their practical shading capacity, and computationally resample the continuous hyperspectral datacubes. This mathematical aggregation was executed to simulate the discrete optical response of a standard multispectral camera, effectively translating the pure radiometric data into agronomically actionable information.

3.5.1 Agronomic Translation and Shading Factor Extraction

To translate the purely radiometric data into agronomically actionable information, we used the isolated spatial masks to quantify the total optical attenuation induced by the structures. Rather than restricting the analysis to specific biological bands, we averaged reflectance values across the entire VNIR spectrum evaluated, from 400 to 1000 nm. Because the white calibration panel was normalized to an absolute reflectance of 1, the signal recorded from the isolated background holes ($\bar{R}_{FX_bg}$) gives a direct measure of the light actually transmitted. The practical Shading Factor (SF) for each net follows as the percentage of intercepted incident radiation:

$$SF(\%) = (1 - \bar{R}_{FX_bg}) \times 100 \tag{3.3}$$

We chose this broadband approach to capture the macroscopic light interception behaviour of the nets before moving on to the discrete multispectral simulation. Vegetation indices such as NDVI combine reflectance from both the visible absorption bands and the near infrared plateau, so knowing how much attenuation occurs across the full spectrum matters for interpreting the radiometric errors these nets introduce into aerial prescription maps later in the analysis. The aggregated statistics were exported to tables to build the spectral atlases and run the comparative analysis.

3.5.2 Spectral Simulation of the Maia S2 Multispectral Sensor

To directly bridge the gap between the controlled laboratory environment and the subsequent airborne field surveys, a dedicated computational step was implemented to simulate the optical response of the MAIA S2 multispectral camera. The MAIA S2 sensor features nine discrete spectral bands, specifically engineered to replicate the radiometric resolution of the Sentinel 2 satellite constellation.

While the Specim FX10 scanner provides a continuous high resolution spectral curve across the entire visible and near infrared range, commercial UAV surveys rely on these specific discrete windows. Table 3.2 details the precise spectral characteristics of the nine MAIA S2 channels, including the specific boundaries and the Central Wavelength (CWL), while Figure 3.8 illustrates their relative sensitivity curves.

Table 3.2: Spectral specifications of the nine discrete bands of the MAIA S2 multispectral sensor.

Sensor Band	**Start WL (nm)**	**Stop WL (nm)**	**CWL (nm)**	**Color**
S1	433.0	453.0	443	Violet
S2	457.5	522.5	490	Blue
S3	542.5	577.5	560	Green
S4	650.0	680.0	665	Red
S5	697.5	712.5	705	Red Edge 1
S6	732.5	747.5	740	Red Edge 2
S7	773.0	793.0	783	NIR 1
S8	784.5	899.5	842	NIR 2
S9	855.0	875.0	865	NIR 3

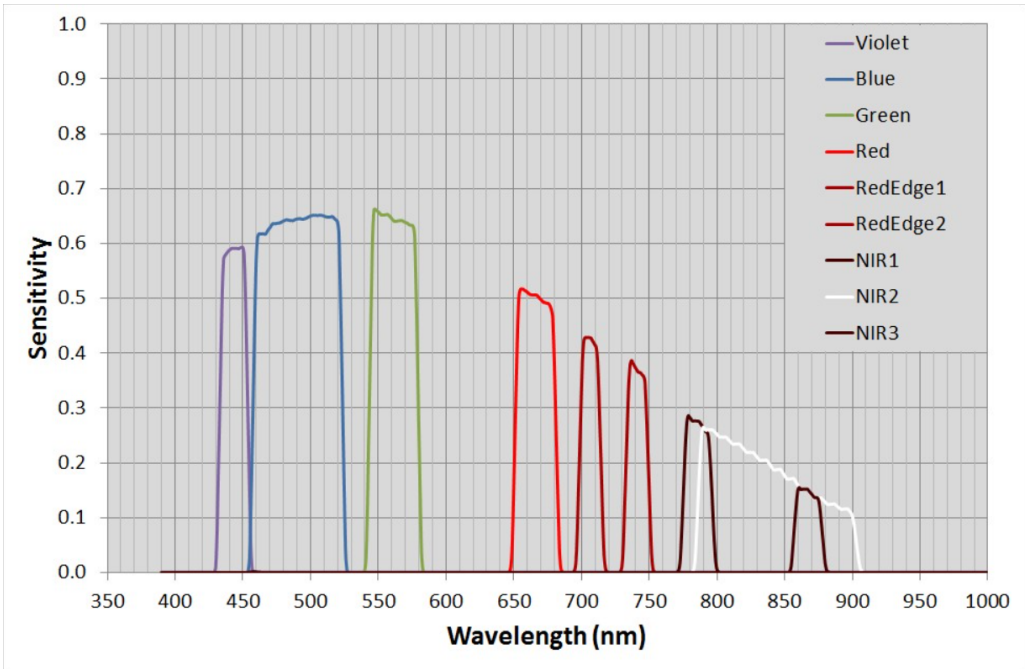


Figure 3.8: Relative spectral sensitivity curves of the MAIA S2 multispectral sensor across the visible and near infrared spectrum. [12]

Utilizing these exact specifications, the MATLAB algorithm aggregated the continuous hyperspectral data acquired in the laboratory. By extracting and mathematically averaging the narrow bands from the Specim datacube that strictly fell within the established Start WL and Stop WL boundaries for each specific chan-

nel, a synthetic nine band multispectral signature was generated for every evaluated sample.

This computational simulation was fundamental to translate the laboratory findings into practical field applications. Specifically, among the three available near infrared channels, the NIR 2 band (Sensor Band S8) was explicitly selected as the designated reference for the computation of the simulated vegetation indices. Isolating this specific narrow band provides the optimal radiometric response required to calculate the NDVI, thereby establishing a robust predictive baseline for the subsequent outdoor photogrammetric flights.

3.6 Outdoor Field Surveys

The final phase of the methodology translated the laboratory findings into real world precision agriculture applications. The activities performed in this stage consisted of programming and executing automated UAV flight missions over an experimental orchard, deploying standardized artificial radiometric targets beneath different netting treatments, and extracting the vegetation indices from the generated orthomosaics to statistically quantify the shading bias under real illumination conditions. The outdoor validation campaigns were carried out with a DJI Matrice 350 RTK (DJI Inc., Shenzhen, China), a quadcopter built for heavy scientific payloads.

3.6.1 UAV Platform and Flight Planning

The outdoor validation campaigns were carried out with a DJI Matrice 350 RTK (DJI Inc., Shenzhen, China), a quadcopter built for heavy scientific payloads. With two TB65 batteries the platform weighs about 6.47 kg, with a maximum takeoff weight of 9.2 kg and a payload capacity of up to 2.7 kg; flight time reaches 55 minutes unloaded, dropping to around 30 minutes at maximum takeoff weight, still enough to cover broad agricultural surfaces in a single mission. The UAV was equipped with the MAIA S2 multispectral camera, a sensor explicitly designed for aerial integration.

As previously detailed in Section 3.5.2 (Table 3.2), the MAIA S2 architecture comprises nine independent monochrome CMOS sensors arranged in a 3×3 matrix with a 25 mm center to center distance. Each individual sensor has physical dimensions of 3.6 × 4.8 mm and a resolution of 1.2 Megapixels (1280 × 960 pixels). Crucially for airborne remote sensing, the sensors are equipped with a global shutter mechanism. This allows for the simultaneous recording of the electromagnetic charge across every photosensitive cell, successfully eliminating rolling shutter distortions and spatial aliasing artifacts typically encountered during high speed flights. Every sensor features a fixed focus lens (calibrated permanently in the laboratory) with a nominal focal length of 7.5 mm, an f/2.8 aperture, and a Field of View (FOV) of 35° horizontally, 26° vertically, and 43° diagonally.

To guarantee precise spatial and radiometric data, the camera system integrates several auxiliary components. An onboard Incident Light Sensor dynamically records ambient illumination changes during the exposures, enabling the accurate

conversion of digital values into absolute reflectance and ensuring data comparability across different lighting conditions. Furthermore, the payload is completed by a dedicated GNSS receiver for automatic image geotagging, an IMU based gimbal connector for optimal attitude stabilization, and radio telemetry systems for real time image transmission and remote control.



Figure 3.9: The DJI Matrice 350 RTK quadcopter equipped with the MAIA S2 multispectral payload, utilized for the outdoor field surveys. The top mounted Incident Light Sensor (ILS) is clearly visible above the main chassis.

Flight missions were meticulously programmed using the UgCS ground station software. To achieve a high spatial resolution while maintaining operational efficiency, the flight altitude was set to 40 m with a constant cruising speed of 6 m/s. The UAV utilized an onboard RTK positioning system, which ensured centimeter level precision for image georeferencing. This geometric configuration yielded a GSD of approximately 0.0139 m/pixel. Both frontal and lateral image overlaps were strictly configured at 75% to guarantee an optimal photogrammetric reconstruction of the canopy.

To evaluate the radiometric distortion under varying solar zenith angles, two identical survey missions were executed on the same day (May 12, 2026). The first acquisition was conducted around solar noon (12:00 PM), while the second took place in the early afternoon (4:00 PM). Both campaigns were performed under clear sky conditions, with low wind and stable illumination, to minimize atmospheric noise. To guarantee absolute data comparability, all flight parameters, including altitude, speed, UAV orientation, overlap percentages, and camera configuration, were maintained strictly constant across both missions.

3.6.2 Experimental Design and Target Deployment

The outdoor validation was performed in an experimental apple orchard characterized by distinct protective infrastructures. To systematically isolate the optical interference of the shading nets from the natural biological variance of different apple tree varieties, the experimental design did not rely on direct canopy reflectance measurements. Instead, standard artificial radiometric targets were deployed at ground level beneath the structures.

The test area was divided into four specific experimental zones to allow for direct comparisons: a sector covered by the Light Green net (net 03 of the laboratory), its adjacent open sky control area, a sector covered by the Black net (net 05 of the laboratory), and its respective adjacent open sky control area. Figure 3.10 illustrates the schematic layout of the experimental design.

To obtain a standardized and highly reliable radiometric baseline across the different orchard sections, 32 identical square white reference panels (0.50 m $\times$ 0.50 m) were utilized. As depicted in the schematic, exactly eight calibration panels were systematically placed within each of the four zones. Figure 3.11 displays the in field positioning of these targets, strategically placed on the grass alleys between the tree rows to avoid direct shadowing from the trunks or lower branches.

These panels served as stable, variety independent radiometric reference targets. By extracting the spectral data exclusively from these standardized surfaces, it was possible to perform a rigorous statistical comparison of the radiometric attenuation caused strictly by the overlying netting materials under real outdoor illumination, effectively bypassing any noise introduced by canopy geometry or leaf biochemistry.

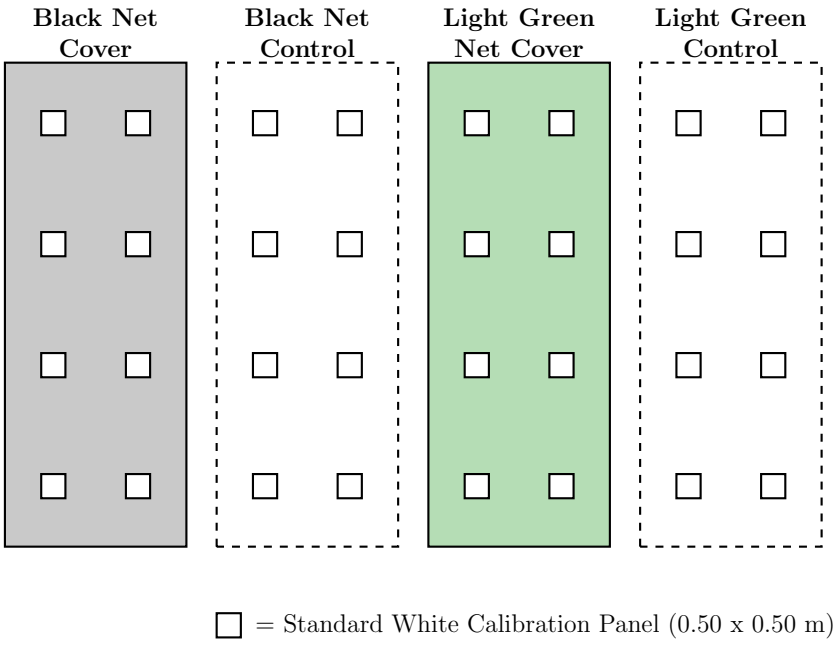


Figure 3.10: Schematic top down layout of the experimental design. The orchard was divided into four distinct zones, with eight identical white calibration panels evenly distributed at ground level within each block to serve as absolute radiometric references.



(a) Under Protective Net (b) Open Sky Control

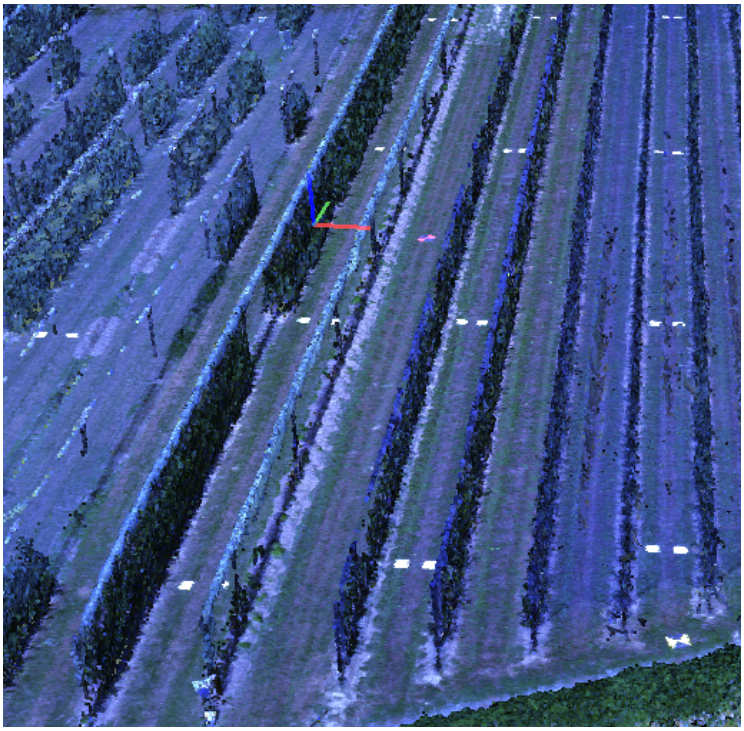
Figure 3.11: In field deployment of the white calibration panels. The artificial targets were positioned on the grass alleys directly beneath the protective nets (a) and in the open sky control zones (b) to provide a stable, variety independent radiometric baseline.

3.6.3 Photogrammetric Pipeline and Data Extraction

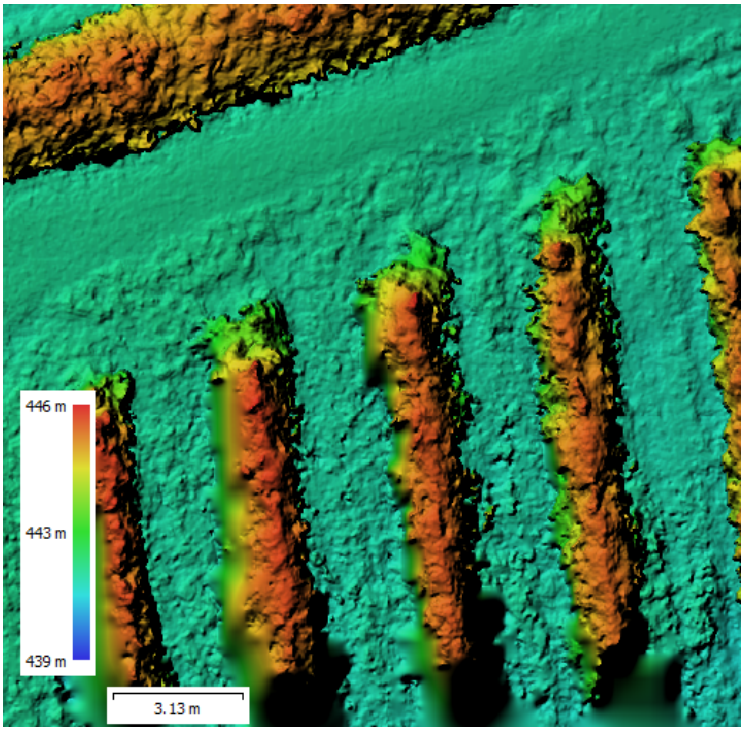
The raw multispectral imagery was processed using Agisoft Metashape Professional (Agisoft LLC, St. Petersburg, Russia). For each flight campaign, a dedicated project was established. All nine spectral bands were imported simultaneously into the software environment to preserve the rigorous spatial co registration between the different optical channels.

The data processing workflow followed a sequential photogrammetric pipeline. Initially, the raw images underwent radiometric calibration utilizing the dedicated MAIA server application. By integrating the ambient irradiance data recorded by the onboard ILS sensor during the flight, the raw digital numbers were converted into absolute reflectance values, ensuring the radiometric comparability of the datasets across the different acquisition times. Subsequently, the image alignment was performed via Structure from Motion (SfM) algorithms to reconstruct the three dimensional geometry of the scene. The models were precisely georeferenced utilizing Ground Control Points (GCPs) acquired with differential GNSS instrumentation.

Following camera optimization, a dense point cloud and the corresponding Digital Surface Model (DSM) were generated.



(a) Dense 3D point cloud



(b) Digital Surface Model (DSM)

Figure 3.12: Photogrammetric outputs generated in Agisoft Metashape. (a) The dense 3D point cloud providing the detailed geometric structure of the orchard and the protective nets. (b) The continuous Digital Surface Model (DSM) interpolated from the dense cloud, necessary for the accurate orthorectification of the multispectral data.

These geometric outputs provided the foundation for the creation of the final multispectral orthomosaics, effectively correcting perspective and radiometric distortions. The ultimate reflectance maps for each of the nine spectral bands were exported in GeoTIFF format utilizing the WGS 84 / UTM zone 32N reference system (EPSG:32632). To guarantee data reliability, any marginal portions of the orthomosaic exhibiting insufficient photographic overlap were systematically excluded from the subsequent analyses.

To evaluate the vigor attenuation, the NDVI was computed using the raster calculator. Aligning with the theoretical framework established in Equation 2.3, the index was derived utilizing the reflectance values of the near infrared band (NIR 2 - Band S8, 842 nm) and the red band (RED - Band S4, 665 nm).

The spatial extraction of the radiometric data was performed through manual segmentation. As illustrated in Figure 3.13, a discrete polygonal Region of Interest (ROI) was manually drawn over each of the 32 white calibration panels on the generated NDVI maps. The extraction algorithm was strictly constrained to evaluate exclusively the pixels falling within these predefined ROIs. This targeted approach isolated the specific radiometric response of the panels beneath the different experimental treatments, preventing any signal contamination from the surrounding grass or orchard canopy.

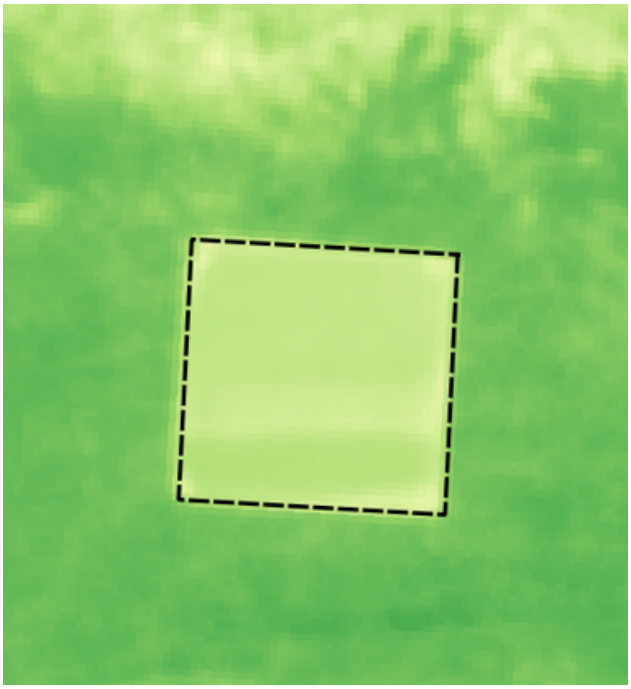


Figure 3.13: Manual delineation of the polygonal Region of Interest (ROI) over a white calibration panel on the processed orthomosaic. NDVI values were extracted exclusively from the internal pixels to avoid signal contamination.

The statistical evaluation of the extracted NDVI values was conducted within the MATLAB programming environment (The MathWorks Inc., Natick, MA, USA). A one way Analysis of Variance (ANOVA) was executed to ascertain the presence of statistically significant differences between the mean NDVI values recorded under

the three primary experimental conditions: the open sky Control (aggregating the unnetted zones), the Light Green net, and the Black net.

Following the confirmation of a significant F-test, multiple post hoc comparisons were performed utilizing Tukey's Honestly Significant Difference (HSD) test with a significance level (α) set at 0.05. To facilitate data interpretation in the final results, the statistical outcomes are represented using standard significance letters, where treatments sharing the same letter indicate no statistically significant difference ($p > 0.05$), while different letters denote a statistically significant radiometric divergence ($p < 0.05$).

Chapter 4

Results

This chapter presents the analytical outcomes of the experimental campaign, structured to logically reflect the methodological progression from controlled indoor environments to open field UAV surveys.

The findings are organized into three main sections. The first section details the preliminary optical validation of the laboratory setup, utilizing spatial variance analysis to mathematically demonstrate how a raised geometric configuration successfully simulates the radiometric integration typical of a drone's airborne perspective. The second section focuses on the core spectral characterization and sensor cross validation performed on the definitive selection of agricultural shading nets. It sequentially presents the baseline instrument calibration, the extraction of morphometric and agronomic parameters, the spectral atlases, and the step by step mathematical reconstruction of the "mixed pixel" effect by isolating the components above and below the meshes. Finally, the third section translates these laboratory findings into real world precision agriculture scenarios. It presents the quantitative radiometric evaluation conducted on ground truth targets during outdoor UAV flights, directly assessing the impact of the protective nets on multispectral vigor maps.

4.1 Optical Setup Validation

To accurately evaluate the optical properties of the shading nets, the experimental methodology initially involved acquiring the samples under three geometric configurations: the contact setup at a distance of 1 cm, and the two raised setups (focused and defocused) at an elevation of 5 cm, as described in Section 3.3. Figures 4.1 to 4.5 illustrate the spectral behavior of the five evaluated nets across the available setups.

A detailed analysis of the spectral curves reveals a consistent trend across the evaluated samples. The contact setup (1 cm) systematically exhibits a significantly higher standard deviation and altered mean reflectance values compared to the elevated configurations. This behavior is mathematically justified by the principles of geometric optics regarding extended light sources, where the length of the pure shadow cone (umbra), denoted as L, generated by an obstacle is calculated using the formula:

$$L = \frac{d \cdot h}{D - d} \tag{4.1}$$

where d represents the thickness of the net thread (estimated at approximately 2 mm), D is the effective width of the halogen light source (estimated at 10 mm), and h is the distance between the light source and the net. Given a total fixed distance from the halogen lamps to the background plane of 180 mm, the variable h adjusts according to the net's elevation. For the contact setup (net elevated at 10 mm), h is 170 mm, yielding an umbra length L of 42.5 mm (4.25 cm). Consequently, the background plane located only 1 cm away falls entirely within the pure shadow region, resulting in a sharp, high contrast radiometric transition between the solid threads and the highly reflective background. Conversely, elevating the nets to 50 mm (5 cm) reduces h to 130 mm, producing a theoretical umbra length L of 32.5 mm (3.25 cm). At this elevation, the 5 cm physical gap effectively places the background well beyond the 3.25 cm apex of the umbra, allowing the pure shadow to dissipate entirely into a diffused penumbra. This physical diffusion drastically reduces the spatial standard deviation, homogenizing the radiance field and accurately replicating the mixed pixel phenomenon experienced by a UAV during aerial surveys, which explains why the two elevated setups (focused and defocused at 5 cm) yield almost perfectly overlapping spectral signatures and comparably low variances.

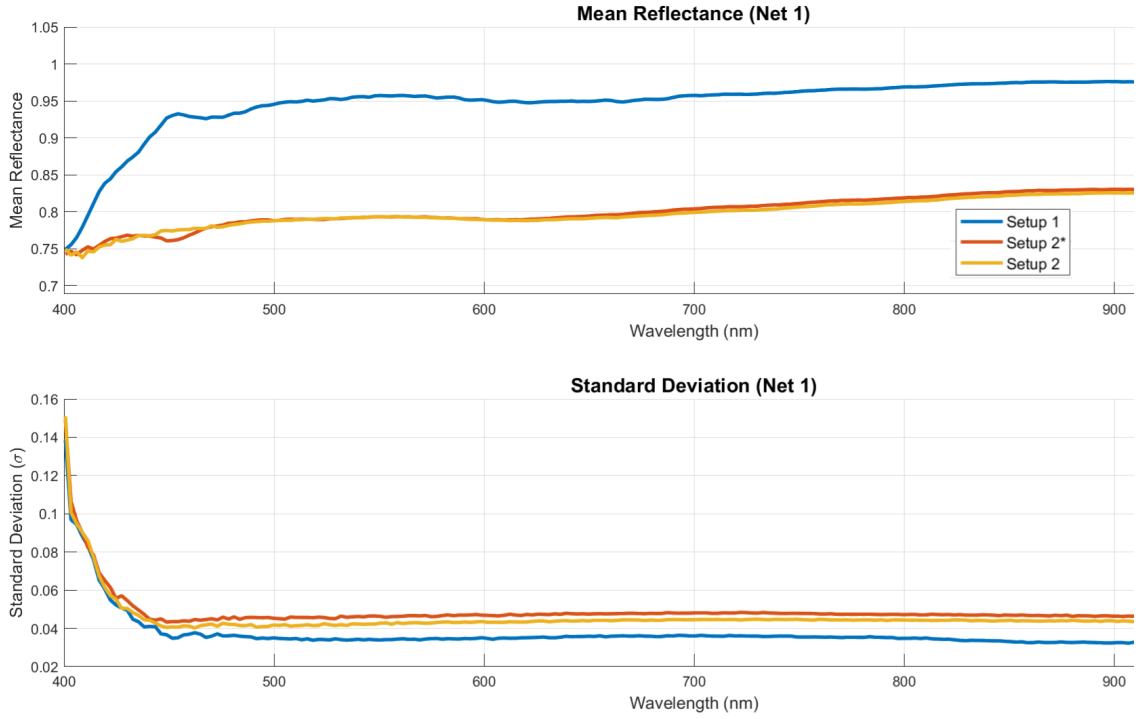


Figure 4.1: Comparison of spectral signatures across different acquisition setups for Net 01 (Dark Green). Above the mean reflectance and under the standard deviation.

During the acquisition phase, a dataset asymmetry occurred due to specific focusing constraints of the hyperspectral camera. While Nets 02, 03, and 04 were successfully captured under all three configurations, Nets 01 and 05 were only acquired using the contact and the raised focused setups.

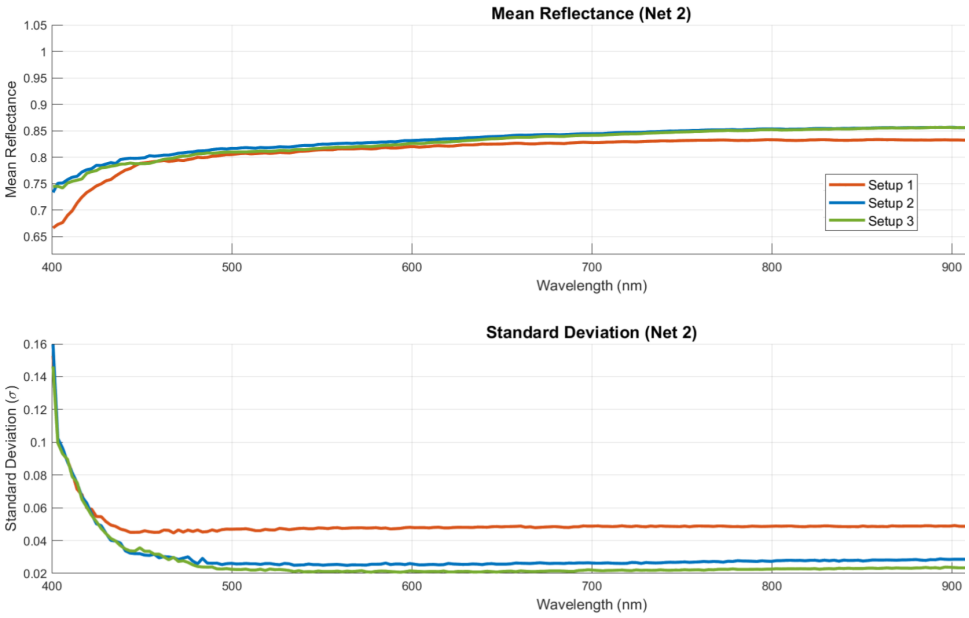


Figure 4.2: Comparison of spectral signatures across different acquisition setups for Net 02 (Black).Above the mean reflectance and under the standard deviation.

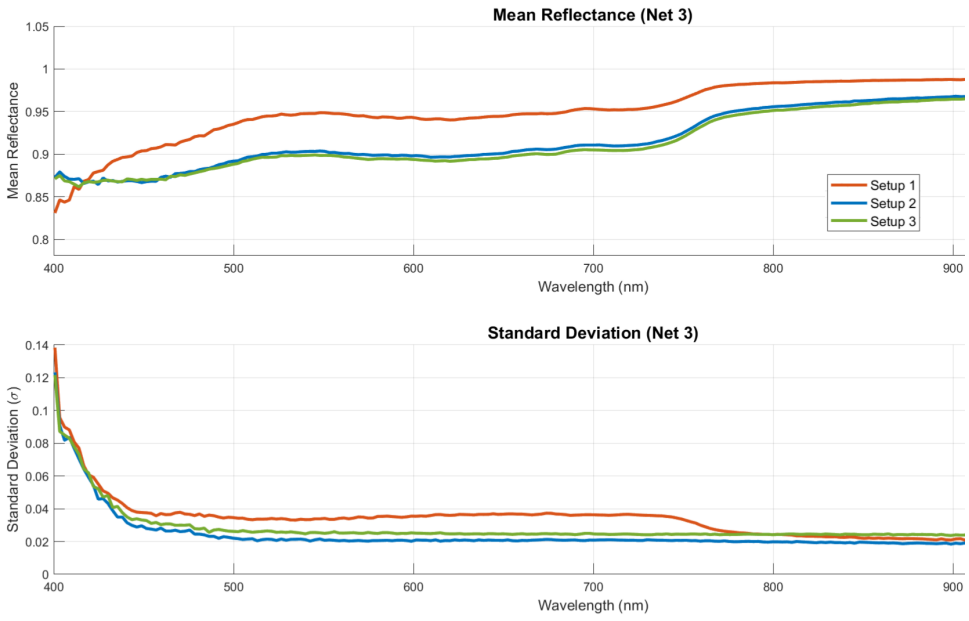


Figure 4.3: Comparison of spectral signatures across different acquisition setups for Net 03 (Light Green). Above the mean reflectance and under the standard deviation.

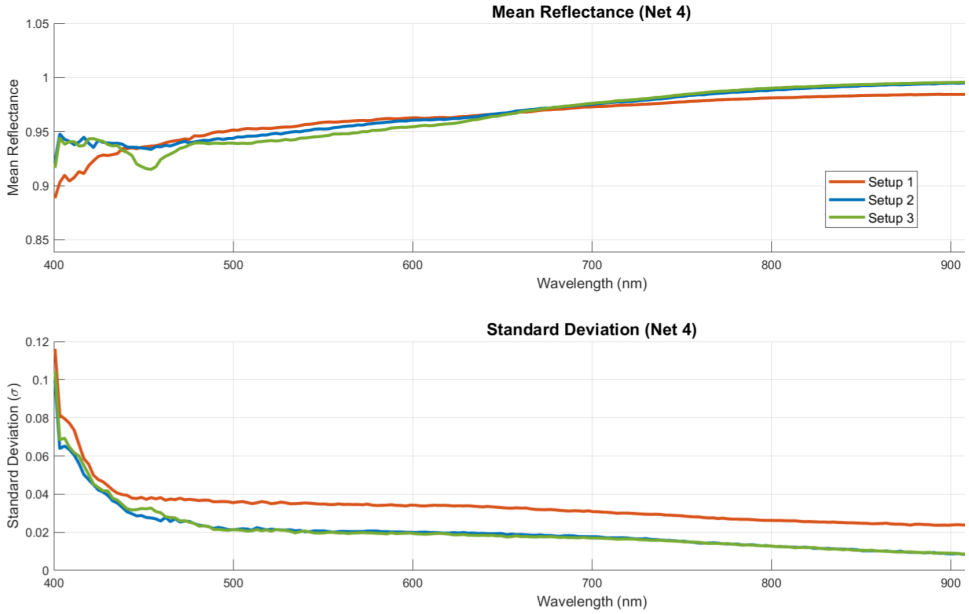


Figure 4.4: Comparison of spectral signatures across different acquisition setups for Net 04 (Transparent). Above the mean reflectance and under the standard deviation.

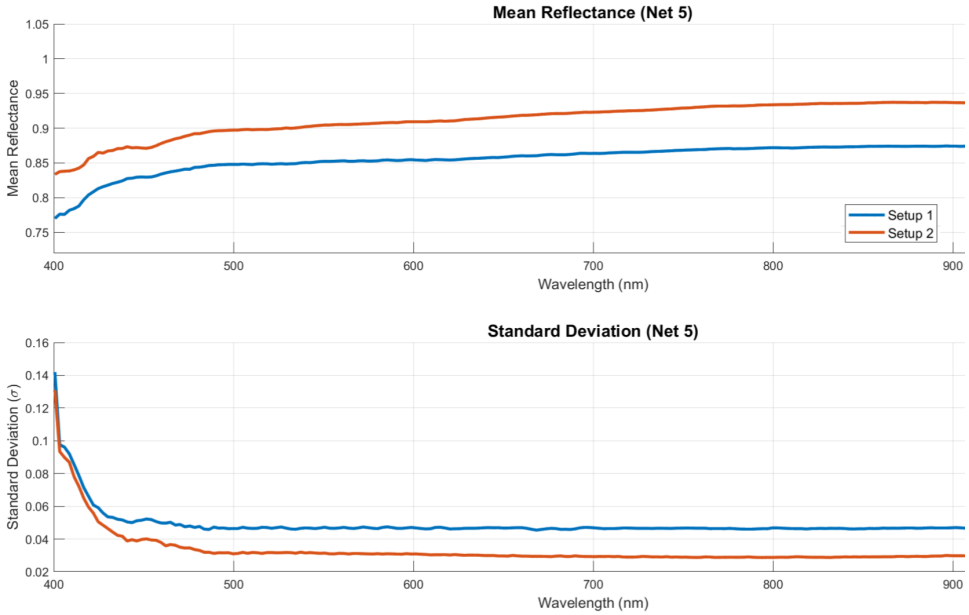


Figure 4.5: Comparison of spectral signatures across different acquisition setups for Net 05 (Grey). Above the mean reflectance and under the standard deviation.

Furthermore, to ensure absolute focus on the background plane beneath the dark, dense mesh of Net 1, a high contrast metallic target (a hex key) was temporarily placed on the white reference sheet during setup to assist the camera's optical calibration. Despite the missing defocused data for Nets 01 and 05, the analysis of

the complete datasets (Nets 02, 03, and 04) clearly demonstrates the optical equivalence between the raised focused and raised defocused configurations. Therefore, given their overlapping radiometric stability and shared capacity to properly simulate the diffused shadow, both elevated configurations were validated and considered entirely suitable as standard baselines for the official acquisitions in the subsequent laboratory sessions.

4.2 Nets Optical and Spectral Characterization

This chapter focuses on the comprehensive evaluation of the optical behavior, spectral signatures, and practical shading performance of the selected agricultural covers. The primary analytical objective is to dissect how distinct polymer compositions, weaving patterns, and chromatic properties alter the spectral response across the visible and near infrared domains. Rather than acting as neutral density filters, the evaluated networks introduce highly variable optical alterations: while black structures impose a flat, broadband attenuation, chromatic variations such as the light green net generate strong wavelength dependent behaviors, particularly characterized by a high near infrared transmission compared to visible absorption.

Following the exhaustive characterization of these distinct spectral signatures, a dual sensor cross validation framework utilizing both the Specim FX10 hyperspectral scanner and the RS-5400 spectroradiometer is implemented. This comparative workflow is deliberately positioned not as the primary focus, but as a rigorous methodological verification tool to confirm that the physical optical properties identified in the laboratory are recorded with absolute consistency and reliability across different measurement architectures, bridging continuous spatial imaging with discrete point based radiometry.

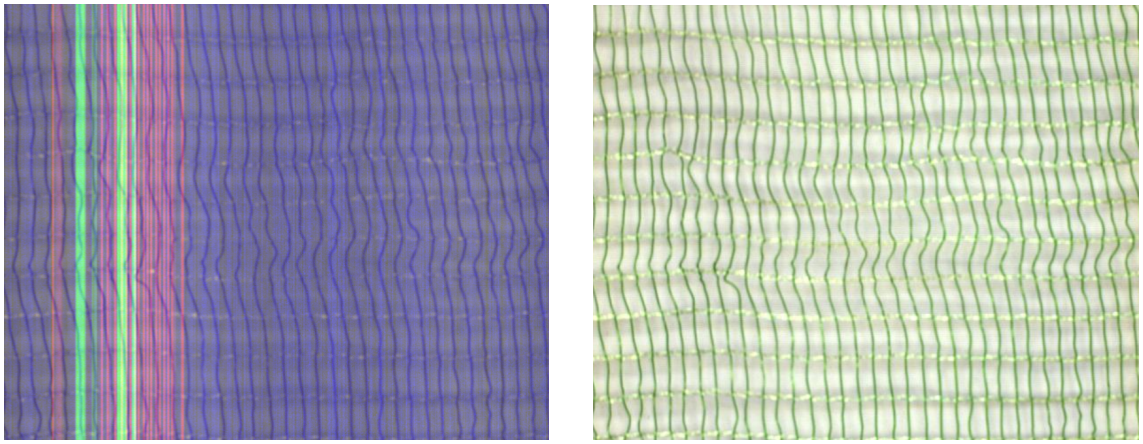
4.2.1 Baseline Calibration

As detailed in the methodological framework (Section 3.3), the radiometric calibration of the raw hyperspectral datacubes was a mandatory prerequisite before conducting any spatial or spectral extraction. The empirical line method was systematically applied to the raw digital numbers of the definitive testing subset, comprising Nets 02, 03, 05, and 06. By utilizing the white background as the primary reference and subtracting the sensor's thermal noise via the dark reference, the computational pipeline successfully compensated for the spatial inhomogeneities of the artificial halogen illumination.

The quantitative outcome of this baseline calibration is a stable and reliable radiometric field where the pure white background consistently returns an absolute reflectance value of 1.0 across the entire spatial domain. This mathematically confirms the successful removal of the directional illumination gradients and sensor noise through the empirical line correction.

To visually demonstrate the practical effectiveness of this computational process, Figure 4.6 provides a single exemplary comparison utilizing the raw and calibrated data of Net 03 (Light Green). The raw image, visibly affected by vertical striping artifacts and lateral illumination drops, is completely transformed into a uniform

reflectance map. This normalization provides a robust foundation for the subsequent isolation of the polymeric threads and the accurate evaluation of the shading factor across all evaluated samples.



(a) Raw (DN) (b) Calibrated Reflectance

Figure 4.6: Visual demonstration of the baseline calibration process (exemplified on Net 03, Light Green). The left panel displays the raw, uncalibrated digital numbers affected by illumination gradients, while the right panel shows the processed reflectance yielding a completely uniform radiometric background.

4.2.2 Morphometric Analysis and Spatial Segmentation

Following the radiometric calibration, the supervised classification algorithm was executed to extract the exact geometric fractions of the evaluated samples. This spatial segmentation is crucial to quantify the physical area occupied by the solid threads (the optical obstacle) versus the empty background holes (the transmitted signal).

As demonstrated in Figure 4.7, the algorithm utilizes a Spectral Angle Mapper (SAM) approach. By evaluating the spectral distance between every pixel and the manually selected training regions, it generates a continuous spatial error map (center) that is subsequently thresholded to create the definitive isolated mask of the network structure (right).

To ensure the physical fidelity of the extracted geometric fractions, a slight manual rounding was applied to the raw algorithmic outputs. This necessary adjustment compensated for minor classification noise, such as isolated spurious pixels or micro shadows detected along the thread edges. Furthermore, for the heterogeneous bicolor samples (Nets 03 and 05), the algorithm successfully discriminated between the different polymer pigments. In these instances, the fractional percentages of the individual colors are calculated exclusively relative to the solid net structure, independent of the total image area.

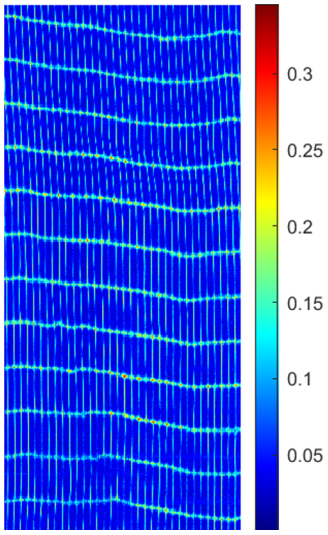


Figure 4.7: Example of the automated spatial segmentation process. The algorithm evaluates the calibrated Region of Interest (left) by calculating the spectral angles (center), ultimately generating the isolated binary mask of the physical threads (right).

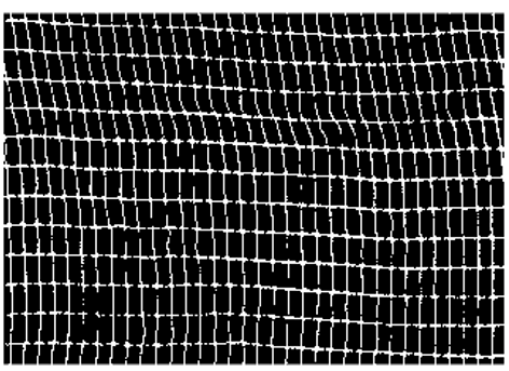
The final morphometric results for the definitive testing subset are summarized in Table 4.1.

Table 4.1: Morphometric results detailing the total physical area occupied by the shading nets and the specific internal pigment distribution for bicolor samples.

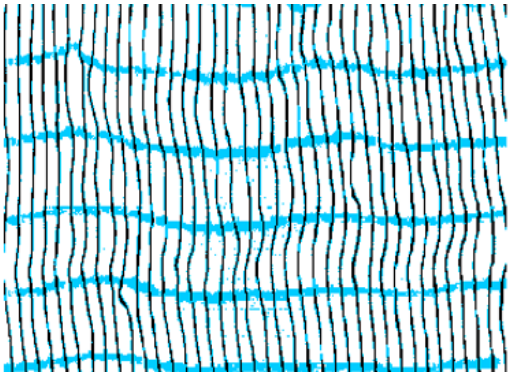
ID	**Type**	**Net Area (%)**	**Pigment Dist. (%)**
Net 02	Monocolor (Black)	17.5	100 Black
Net 03	Bicolor (Light Green)	29.0	71 Green, 29 White
Net 05	Bicolor (Grey/Black)	21.5	77 Black, 23 Grey
Net 06	Transparent	22.0	100 Transparent

Interpreting these extracted geometric fractions is a fundamental prerequisite for the subsequent radiometric analyses. The "Net Area (%)" mathematically quantifies the exact physical occlusion caused by the structural threads within the sensor's field of view. Consequently, this parameter acts as the primary weighting coefficient in the mixed pixel equation: structures presenting a higher physical coverage, such as Net 03 (29.0%), inherently dominate a larger fraction of the integrated radiometric signal, maximizing the potential optical interference compared to thinner meshes like Net 02 (17.5%). Furthermore, for heterogeneous structures, the internal pigment distribution explicitly defines the chromatic composition of that interference. For instance, the radiometric impact of Net 03 is not uniformly green, but structurally governed by a specific ratio of 71% transmissive green polymer and 29% highly reflective white structural threads. Isolating these exact geometric and chromatic fractions provides the precise numerical coefficients required to computationally simulate how the physical net blends with the underlying canopy in standard UAV surveys.

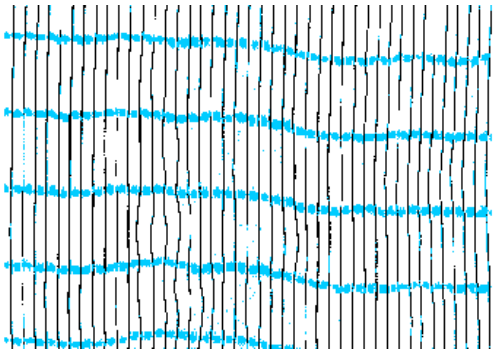
Figure 4.8 illustrates the final isolated spatial masks utilized to compute these areas. Monocolor nets are represented as simple binary masks (white threads on a black background), whereas bicolor nets are displayed as multiclass segmentations to highlight the specific spatial arrangement of the differently pigmented threads.



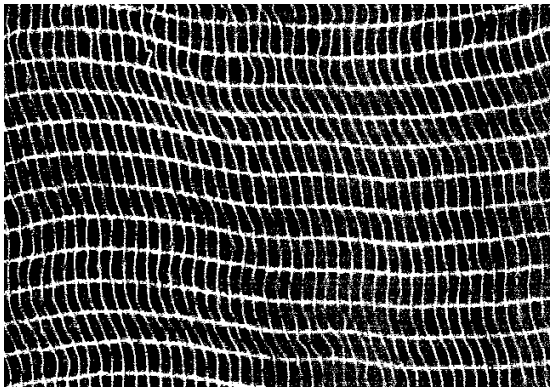
(a) Net 02 (Binary Mask)



(b) Net 03 (Multiclass Mask)



(c) Net 05 (Multiclass Mask)



(d) Net 06 (Binary Mask)

Figure 4.8: Final segmented masks utilized for the geometric fractional area extraction. Monocolor nets (02 and 06) are isolated using binary logic, while bicolor nets (03 and 05) employ multiclass segmentation to distinguish specific pigment contributions.

4.2.3 The Spectral Atlas

By directly applying the isolated spatial masks obtained during the morphometric analysis to the calibrated hyperspectral datacubes, the pure radiometric signatures of the solid netting materials were extracted (R_{FX_net}). To ensure the utmost mathematical rigor, for the heterogeneous bicolor samples (Net 03 and Net 05), the mean reflectance was not extracted as a simple global spatial average. Instead, the distinct spectral behaviors of each specific pigment were isolated independently using the multiclass masks. The overall pure spectral signature of the solid net was then computationally reconstructed by mathematically weighting these pure pigment curves according to their exact geometric fractional percentages established in Table 4.1 (e.g., 71% Green and 29% White for Net 03). This procedure completely decoupled the optical response of the High Density Polyethylene (HDPE) threads

from the underlying background, generating a highly accurate definitive spectral atlas for the evaluated covers across the visible and near infrared (VNIR) spectrum (400-1000 nm).

Figure 4.9 presents the definitive Spectral Atlas of the four evaluated samples. The top panel illustrates the mean reflectance curves, while the bottom panel displays the corresponding spatial standard deviation, which acts as a mathematical metric for light uniformity.

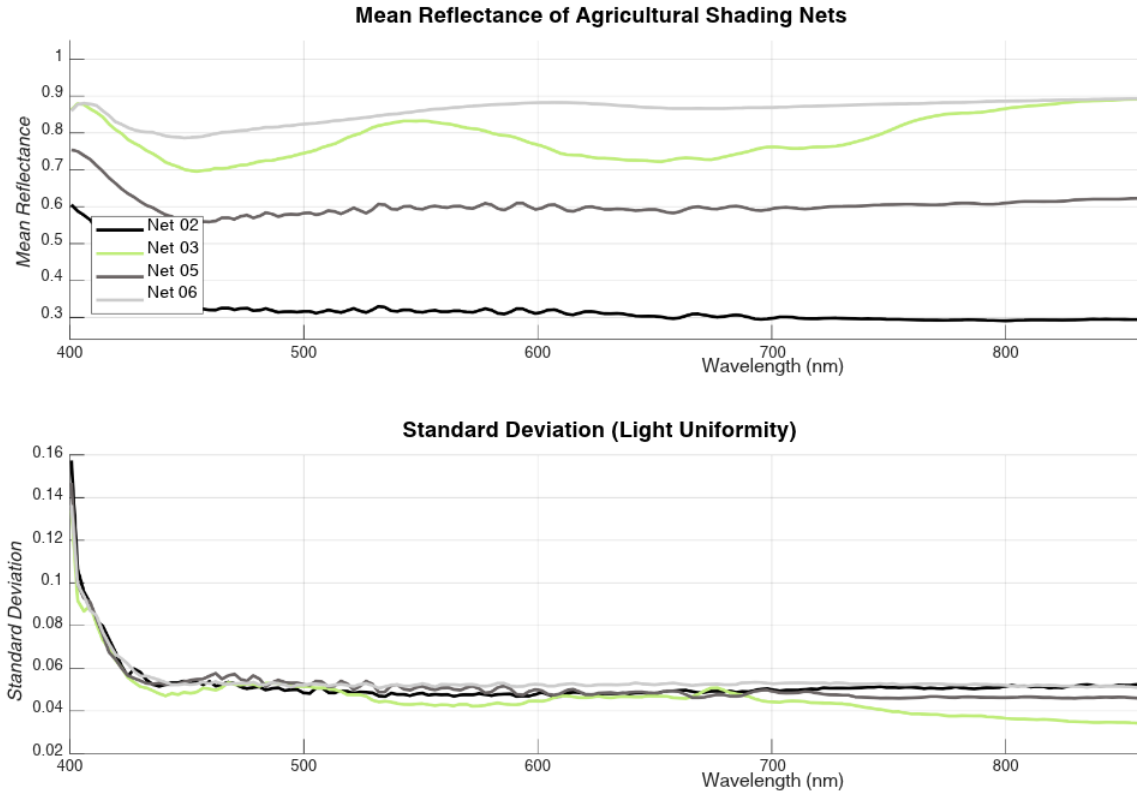


Figure 4.9: Spectral Atlas of the four definitive agricultural shading nets. The top panel displays the pure mean reflectance of the solid polymeric threads across the VNIR range. The bottom panel illustrates the spatial standard deviation (σ), confirming the high radiometric homogeneity of the extracted signal.

A comparative analysis of the mean reflectance curves reveals distinct optical behaviors dictated by the polymer pigmentation. Net 06 (Transparent) and Net 02 (Black) represent the two radiometric extremes of the dataset. Net 06 exhibits the highest overall reflectance (consistently above 0.8 across most of the spectrum), acting primarily as a strong, wavelength independent optical diffuser. Conversely, Net 02 demonstrates a flat, broadband attenuation profile with the lowest reflectance (approximately 0.3) across the entire VNIR spectrum, indicative of its high radiation absorption capacity. Net 05 (Grey/Black) displays an intermediate, relatively flat spectral response, stabilizing around a reflectance of 0.6 after an initial drop in the lower visible range.

Crucially, Net 03 (Light Green) introduces a highly specific, wavelength dependent distortion rather than a neutral density filtration. Its spectral signature mimics

typical vegetation foliage: it displays a localized reflectance peak in the green visible region (around 530-550 nm), pronounced absorption in the red band (650-680 nm), and a sharp increase in the Near Infrared (NIR) region (> 700 nm), where its reflectance approaches the levels of the transparent net. This non neutral optical behavior is of critical agronomic importance, as it has the potential to significantly interfere with the standard red and NIR channels utilized to compute standard vegetation indices, such as the NDVI.

Finally, the bottom panel confirms the robustness of the acquisition methodology. Aside from a localized variance spike at the extreme 400 nm boundary, attributable to the lower signal to noise ratio of the halogen lamps and reduced sensor sensitivity at the edge of the visible spectrum, the standard deviation remains remarkably low and stable (between 0.04 and 0.06) for all evaluated samples across the 450-1000 nm range. This mathematically validates the spatial homogeneity of the radiometric field achieved by the raised focused setup, ensuring that the extracted mean reflectance values represent a perfectly integrated signal without the interference of localized, high contrast shadows.

4.2.4 Agronomic Parameters and Shading Factor Evaluation

To translate the purely radiometric data into actionable agronomic information, the spatial masks were inverted to isolate exclusively the empty background holes. Because the bare white background was initially calibrated to represent a baseline reflectance of 100%, the radiometric signal recorded strictly from these shaded background regions mathematically represents R_{FX_bg}, effectively quantifying the transmitted light. Consequently, the practical Shading Factor (SF) for each net was calculated by measuring the percentage of intercepted incident radiation across the evaluated spectral range, as formally defined by Equation 3.3 in the methodological framework.

Table 4.2 summarizes the aggregated optical performance for the four definitive shading nets, detailing the mean transmittance, the resulting Shading Factor, and the spatial variance of the transmitted light field.

Table 4.2: Aggregated agronomic parameters evaluating the total radiometric transmission and practical shading capacity of the four evaluated networks.

Net	R_{FX_bg} **(%)**	**SF (%)**	**Std. Dev. (%)**
02 (Black)	83.57	16.43	3.02
03 (Light Green)	92.30	7.70	2.36
05 (Grey/Black)	91.50	8.50	3.31
06 (Transparent)	92.45	7.55	2.87

An engineering analysis of the extracted parameters reveals significant quantitative differences strictly dependent on the physical and chromatic properties of the structural threads. As anticipated, Net 02 (Black) physically intercepts the highest proportion of incident radiation, providing the maximum shading capacity with a

practical Shading Factor of 16.43%. Conversely, Net 06 (Transparent) acts primarily as a diffusing element rather than an optical blocker, allowing maximal light penetration and yielding the lowest Shading Factor of 7.55%. The bicolor structures deliver intermediate performances, with Net 03 (Light Green) demonstrating a transmission profile very similar to the transparent baseline (7.70% Shading Factor), while Net 05 (Grey/Black) exhibits a slightly higher light interception (8.50%).

Crucially, the spatial uniformity of the transmitted radiation is mathematically validated by the Mean Standard Deviation parameter. Across all evaluated samples, the variance of the light reaching the background remains remarkably low, ranging strictly between 2.36% and 3.31%. These narrow intervals confirm that the optimized raised setup successfully generates a highly diffused and homogeneous light field beneath the canopy. By preventing the formation of sharp shadows with high contrast, this optical diffusion ensures that the radiometric signal captured directly reflects the stable agronomic environment, providing an optimal baseline for the subsequent extraction of multispectral vegetation indices.

4.2.5 Comparative Baseline Assessment: Instrument Alignment

Before evaluating the complex optical interactions introduced by the shading structures, a preliminary cross validation was conducted to ensure absolute radiometric alignment between the two employed instruments: the Specim FX10 hyperspectral scanner and the RS 5400 portable spectroradiometer. As detailed in the Phase A validation protocol (Section 3.4.3), this baseline check was performed by measuring the bare white calibration panel without any interfering mesh to isolate the pure instrumental response to the halogen light source.

Given the fundamentally different sensor architectures and fields of view, a continuous push broom line scanner processing a spatial Region of Interest (ROI) versus a point based fiber optic probe, a direct comparison of absolute raw values would have introduced bias. Furthermore, an excessively illuminated white reference panel during the initial laboratory setup caused a shift in the absolute intensity rendering. However, because this identical background illumination was maintained consistently across all subsequent acquisitions, the underlying relative spectral shapes remained completely stable and mathematically reliable.

Therefore, to strictly compare the spectral responses and confirm the absence of instrumental bias while compensating for this absolute intensity offset, a peak normalization algorithm was applied using a dedicated MATLAB script. Both the spatially averaged Specim FX10 data and the interpolated RS 5400 readings were scaled to a maximum relative value of 100, allowing the analysis to focus exclusively on the morphology of the spectral signatures.

Figure 4.10 illustrates the result of this baseline alignment. An analysis of the normalized curves reveals the characteristic emission profile of the halogen lamps utilized in the setup, displaying a typical bell shape with lower emission in the short visible wavelengths and a peak in the red to near infrared transition zone.

Rather than a theoretical perfect overlap, the graph highlights the distinct physical signatures of the two hardware architectures. The RS 5400 spectroradiometer

demonstrates a sharper, earlier intensity peak around 708 nm, accompanied by steeper drops at the spectral extremes and localized signal variations typical of fiber optic transmission. Conversely, the Specim FX10 scanner records its maximum peak slightly later at approximately 743 nm and maintains a significantly broader intensity shoulder in both the blue region (below 450 nm) and the near infrared spectrum (above 800 nm).

Understanding these baseline instrumental divergences is crucial. Having established and normalized these inherent hardware characteristics on the pure white background during Phase A, it is possible to proceed with certainty. Any subsequent spectral variation detected when interposing the agricultural nets can be entirely attributed to the optical interference of the physical meshes, rather than to an uncalibrated instrumental error.

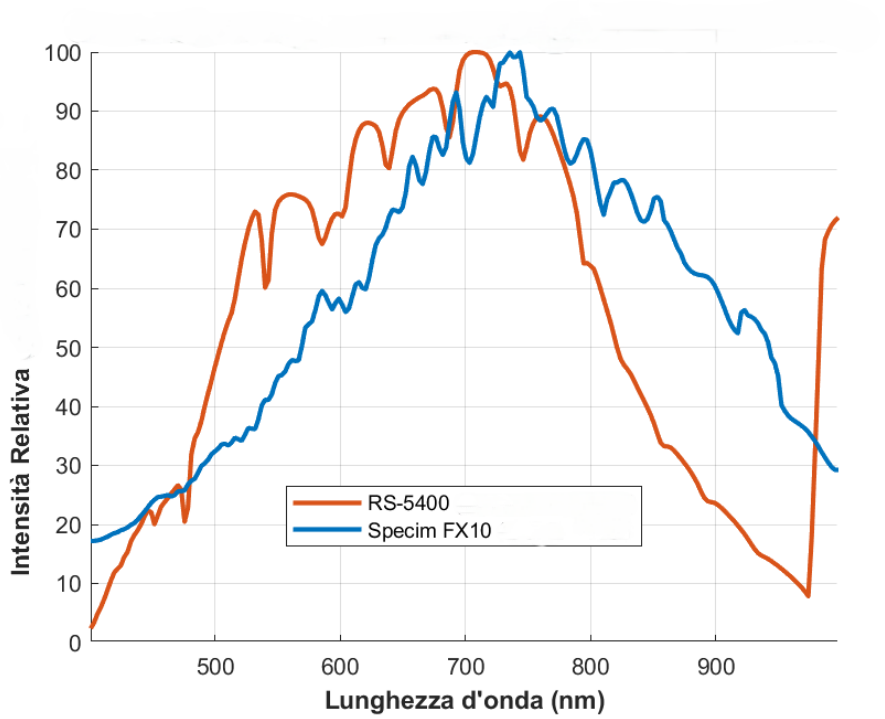


Figure 4.10: Baseline sensor cross validation on the bare white background. The peak normalized spectral curves illustrate the distinct hardware responses of the Specim FX10 scanner and the RS 5400 spectroradiometer to the halogen illumination source, prior to the introduction of the shading nets.

4.2.6 Above Canopy Radiometric Analysis: The UAV Mixed Pixel Simulation

Serving as a cornerstone of this radiometric study, the analysis proceeded to Phase B of the validation framework (Section 3.4.3). This crucial stage evaluated the macroscopic optical signal reflected from above the shading structures. Unlike the sub canopy isolation, this measurement captures the true mixed pixel effect: the exact radiometric integration of both the solid polymeric threads and the underlying

background gaps. This configuration physically replicates the precise macroscopic optical signal that an Unmanned Aerial Vehicle (UAV) multispectral camera records during an open field flight over a netted agricultural orchard.

To validate this mixed signal, the macroscopic response acquired by the Specim FX10 was cross referenced against the RS 5400 spectroradiometer positioned above the canopy (R_{RS_above}). Methodologically, the Specim FX10 data was extracted by applying a large, continuous rectangular Region of Interest (ROI) over the high resolution datacube, ensuring the exact geometric ratio of threads to gaps was captured. Conversely, the RS 5400 measurement represents the spatial average of five discrete conical acquisitions taken above the target area.

To visually illustrate this spatial integration process, Figure 4.11 displays the five individual spectroradiometer scans acquired over Net 03 alongside their computed mean. Minor intensity variations are observable among the single repetitions (grey lines), caused by slight differences in the physical ratio of threads and gaps falling within each specific conical footprint. However, the resulting averaged curve (orange line) successfully smooths these localized physical heterogeneities, providing a highly stable and statistically representative radiometric signal for the macroscopic target.

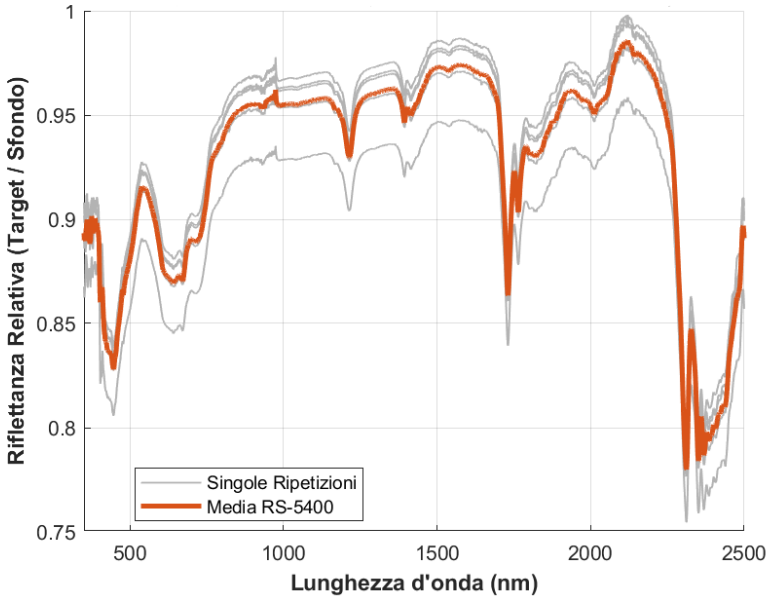


Figure 4.11: Repeatability of the RS 5400 spectroradiometer measurements over Net 03 (Light Green). The graph illustrates the five discrete conical acquisitions (grey lines) capturing localized structural variations, and the resulting spatially integrated mean (orange line) utilized for the cross validation.

Figures 4.12 through 4.13 illustrate the subsequent spectral comparisons for the four definitive covers across the evaluated VNIR range. A vertical intensity offset is visible between the two instruments across all samples. This absolute magnitude shift is an expected geometric consequence of the differing sensor architectures. The Specim ROI is strictly bounded and perfectly orthogonal, whereas the RS 5400 conical FOV from above captures a slightly different spatial integration area and is more susceptible to minor Bidirectional Reflectance Distribution Function (BRDF) variations caused by the three dimensional weaving of the polymer threads.

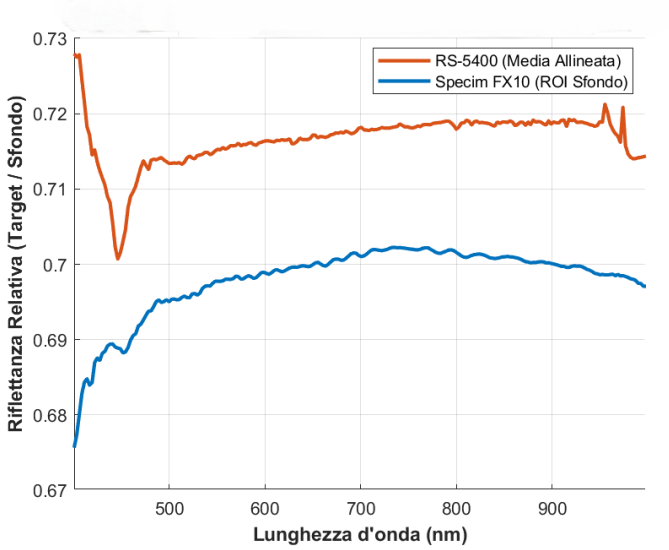


Figure 4.12: Above canopy spectral comparison for Net 02 (Black). The macroscopic mixed signal demonstrates excellent morphological correlation between the Specim FX10 rectangular ROI and the RS 5400 spatial average, successfully validating the UAV pixel simulation.

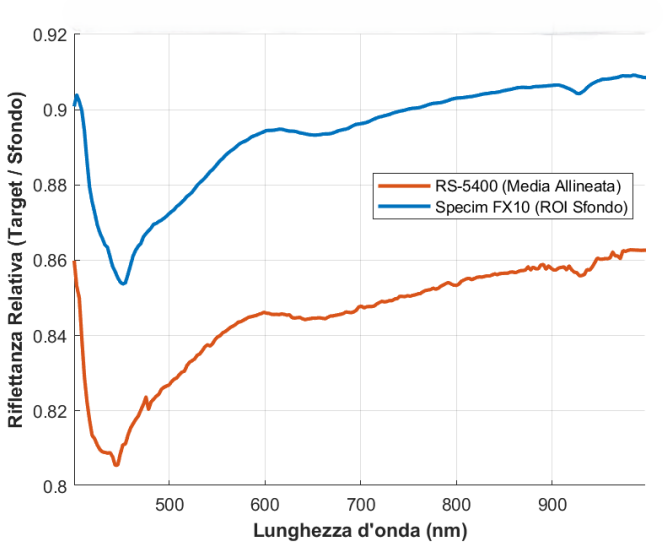


Figure 4.13: Above canopy spectral comparison for Net 06 (Transparent). The high morphological alignment mathematically validates the accuracy of the macroscopic radiometric field captured by the experimental setup.

However, the critical metric for validation is the morphological correlation of the spectral shapes, which is exceptionally high. Unlike the spatial variance observed beneath the absorbing nets, the macroscopic signal integrated from above yields highly stable and perfectly synchronized spectral curves. From the flat broadband absorption of the black polymer (Figure 4.12) to the vegetation like green peak of Net 03 (Figure 4.14), the distinct radiometric features are identically mapped by both the hyperspectral scanner and the point spectroradiometer.

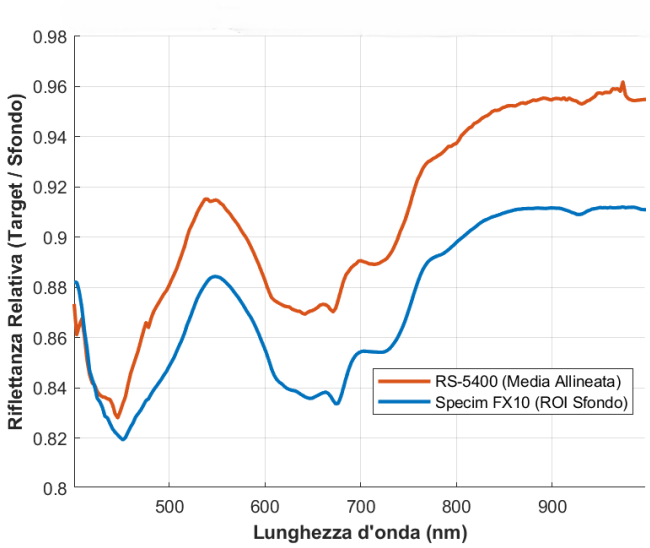


Figure 4.14: Above canopy spectral comparison for Net 03 (Light Green). The highly synchronized spectral curves correctly capture the complex mixed pixel integration of the transmissive green threads and the underlying background.

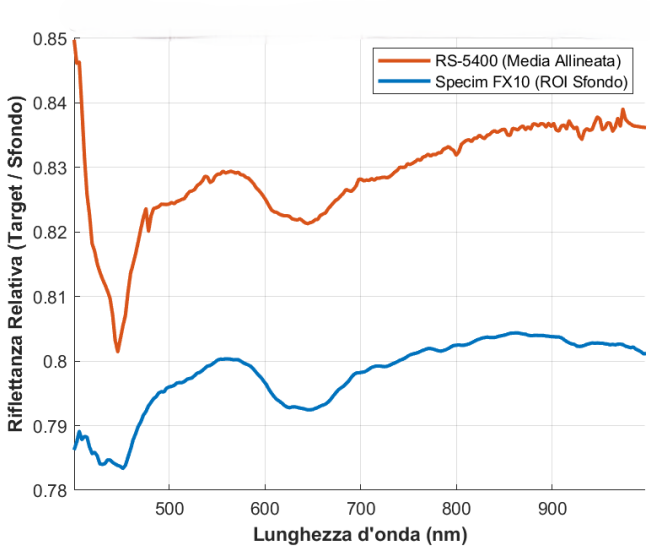


Figure 4.15: Above canopy spectral comparison for Net 05 (Grey/Black). Both instruments perfectly map the stable radiometric attenuation of the heterogeneous structure from above the canopy.

This excellent morphological alignment definitively validates the experimental raised setup. It mathematically proves that the macroscopic mixed signal captured by the Specim FX10 is not an instrumental artifact, but a physically accurate representation of the above canopy radiometric field. This successful cross validation provides a highly robust and reliable foundation for the subsequent multispectral simulation and precision agriculture assessments.

To mathematically quantify the spectral separability of the mixed macroscopic targets and confirm the measurement consistency between the two architectures,

Table 4.3 details the absolute mean reflectance recorded above the canopy. Incorporating the exact laboratory data, the comparison highlights a physiological radiometric offset introduced by the differing integration geometries: the spatial pixel averaging of the Specim FX10 versus the conical field of view of the RS-5400.

However, the introduction of the dedicated offset column (Δ) explicitly demonstrates that this absolute shift remains remarkably constant across all spectral bands for any given target. For instance, the black structure (Net 02) exhibits a consistent broadband profile with a minor offset strictly confined between +1.6% and +2.4%. Similarly, for the structurally complex Light Green cover (Net 03), both sensors perfectly align in identifying the shape of the spectral curve: they jointly validate the local reflectance peak in the green band, the sharp absorption drop in the red region, and the identical transition slope towards the high transmission near infrared plateau ($> 90\%$). This structural stability definitively proves that both sensors perfectly align in capturing the identical spectral behaviors, independent of the geometric baseline.

Table 4.3: Above canopy macroscopic mean reflectance across the primary spectral intervals. The Δ Offset column mathematically highlights the constant geometric shift between the two sensors, confirming their identical capacity to capture the spectral signatures.

Target	**Band (nm)**	**Specim FX10 (%)**	**RS-5400 (%)**	**Δ Offset**
Net 02 (Black)	400–500 (Blue)	68.9	71.3	+2.4
	500–600 (Green)	69.7	71.5	+1.8
	600–700 (Red)	70.0	71.7	+1.7
	700–750 (Red Edge)	70.2	71.8	+1.6
	750–900 (NIR)	70.1	71.9	+1.8
Net 03 (Light Green)	400–500 (Blue)	83.9	85.3	+1.4
	500–600 (Green)	87.2	90.3	+3.1
	600–700 (Red)	84.1	87.6	+3.5
	700–750 (Red Edge)	85.7	89.5	+3.8
	750–900 (NIR)	90.2	94.3	+4.1
Net 05 (Bicolor)	400–500 (Blue)	78.8	82.0	+3.2
	500–600 (Green)	79.9	82.7	+2.8
	600–700 (Red)	79.4	82.4	+3.0
	700–750 (Red Edge)	79.9	82.9	+3.0
	750–900 (NIR)	80.3	83.4	+3.1
Net 06 (Transparent)	400–500 (Blue)	87.0	82.0	−5.0
	500–600 (Green)	88.5	83.9	−4.6
	600–700 (Red)	89.4	84.5	−4.9
	700–750 (Red Edge)	89.8	84.9	−4.9
	750–900 (NIR)	90.4	85.5	−4.9

4.2.7 Sub Canopy Radiometric Analysis: Transmitted Light Assessment

Following the baseline instrumental alignment, the analysis proceeded to evaluate the complex radiometric field generated beneath the shading structures. As de-

fined in Phase C of the methodological framework (Section 3.4.3), this step involved comparing the transmitted radiation computationally extracted from the Specim FX10 datacubes (R_{FX_bg}) against the physical measurements acquired by placing the RS 5400 fiber optic probe directly beneath the nets (R_{RS_under}). It is crucial to highlight the fundamental methodological difference in signal acquisition. The Specim data represents a highly rigorous, computationally masked signal containing exclusively the light passing through the physical canopy gaps. Conversely, the RS 5400 does not measure a dimensionless point; rather, its fiber optic probe possesses a specific angular Field of View (FOV). This conical FOV physically integrates all the radiometric flux falling within its circular footprint beneath the mesh. For each sample, the RS 5400 signal represents the spatial average of five discrete conical acquisitions. Figures 4.18 through 4.17 present the spectral comparisons for the four definitive targets. A vertical intensity offset is immediately observable across all samples. This discrepancy is physically and mathematically expected. The Specim FX10 computationally isolates the brightly illuminated background pixels, representing pure transmission zones without structural interference. In contrast, the RS 5400 conical FOV inherently integrates a mixed radiometric field, incorporating both the direct light passing through the gaps and the micro shadows cast by the overlying threads within its footprint, thereby lowering the absolute recorded intensity. Beyond the absolute intensity, the morphological correspondence of the spectral signatures reveals a critical optical phenomenon strictly dependent on the material properties of the polymers. A satisfactory shape correlation between the two instruments is observed exclusively for Net 03 (Figure 4.16) and Net 06 (Figure 4.17).

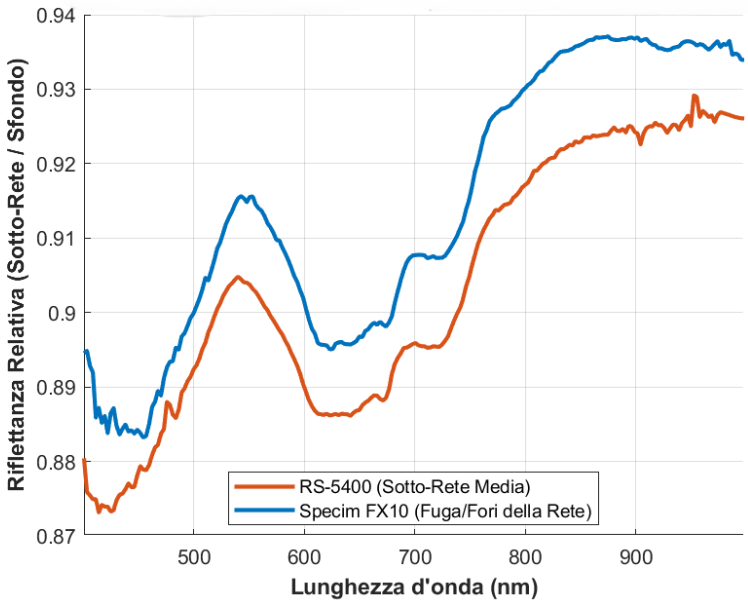


Figure 4.16: Sub canopy spectral comparison for Net 03 (Light Green). The optical diffusion of the green polymer homogenizes the light field, allowing the conical integration of the RS 5400 to successfully correlate with the spectral shape of the Specim FX10 extraction.

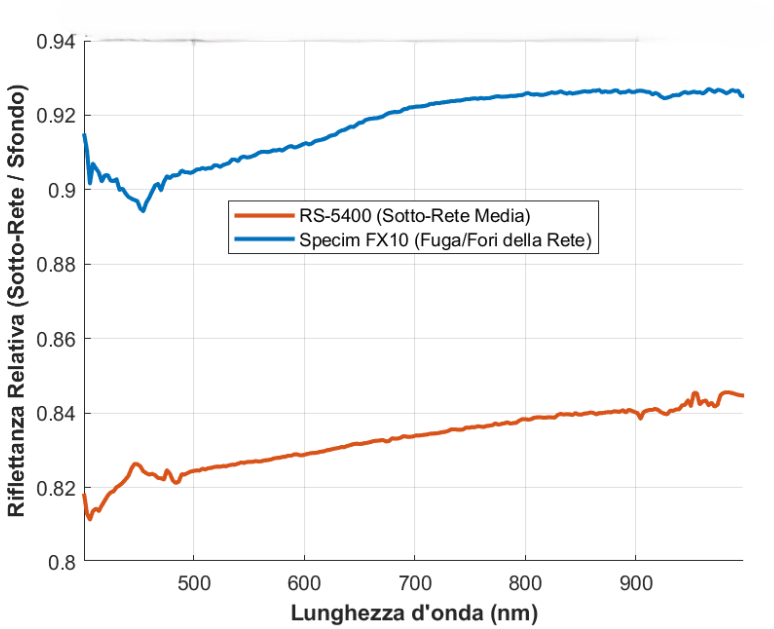


Figure 4.17: Sub canopy spectral comparison for Net 06 (Transparent). The high broadband transmittance yields a uniform transmitted radiation field, ensuring excellent spectral shape correlation between both instrument modalities.

Because the light green and transparent polymers are highly transmissive and act as optical diffusers, they generate a highly homogenized light field beneath the canopy. Consequently, the spatial integration within the five RS 5400 conical footprints successfully captures a statistically representative sample of this uniform transmitted radiation, accurately mirroring the spectral shape extracted by the Specim spatial masks.

Conversely, for Net 02 (Figure 4.18) and Net 05 (Figure 4.19), the spectral shapes exhibit significant divergences. These dark, highly absorbing polymers block radiometric scattering entirely, projecting sharp, high contrast geometric shadows onto the background. In such a macroscopic and highly heterogeneous optical environment, the integrated signal within the discrete conical FOV becomes extremely sensitive to sub millimeter positioning variations relative to the structural grid. Depending on the exact placement, the probe FOV might capture an unbalanced ratio of unattenuated direct light versus deep polymer shadows. Averaging only five discrete conical footprints in this unstable environment is statistically insufficient to capture the true morphological mean, leading to an erratic aggregated signal that fails to match the rigorously masked R_{FX_bg} signature. This behavior mathematically demonstrates a key conclusion of this study: when analyzing highly absorbing, high contrast shading covers, discrete FOV sampling is highly susceptible to spatial aliasing. The high resolution hyperspectral continuous masking approach utilized by the Specim FX10 proves to be vastly superior, providing a highly stable and isolated radiometric baseline.

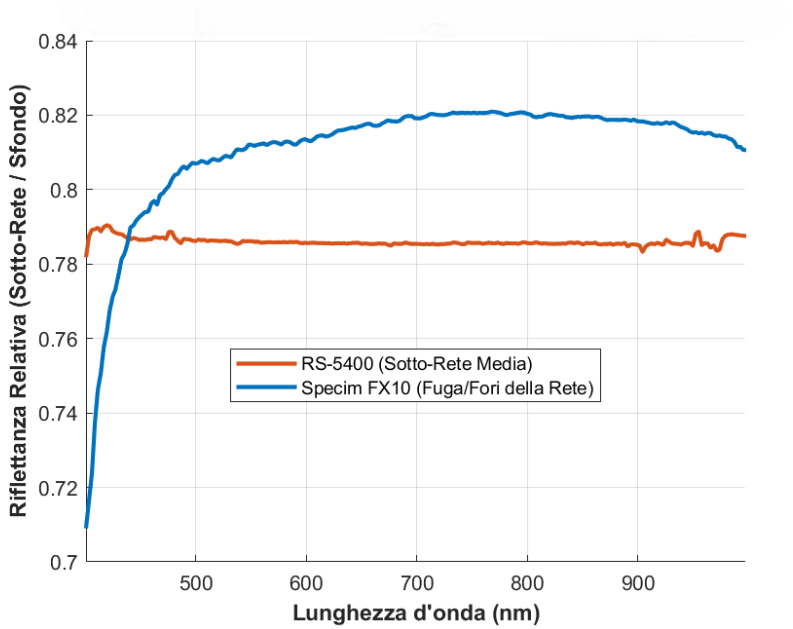


Figure 4.18: Sub canopy spectral comparison for Net 02 (Black). The highly absorbing polymer generates sharp, high contrast shadows, causing the spatial integration within the 5 RS 5400 conical footprints to fail in accurately matching the morphological shape of the rigorously masked Specim FX10 signal.

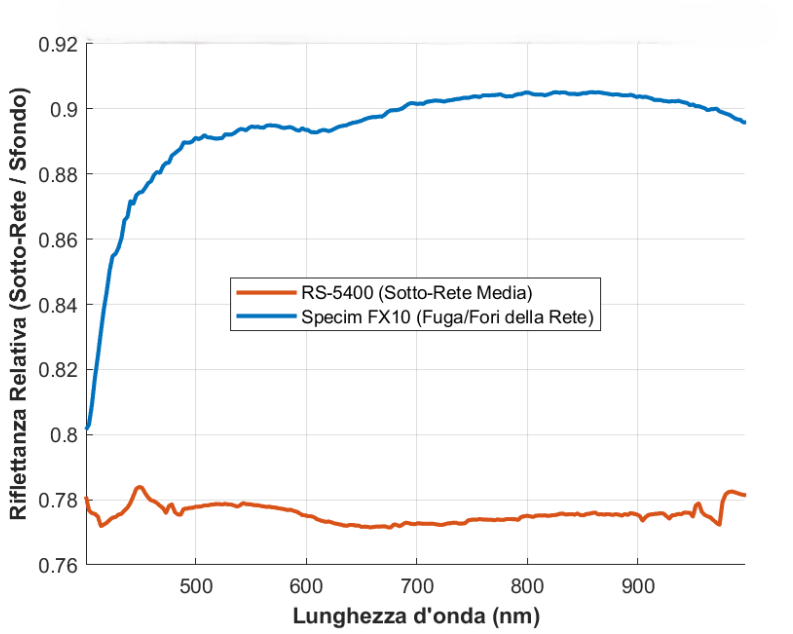


Figure 4.19: Sub canopy spectral comparison for Net 05 (Grey/Black). Similar to Net 02, the absorbing structural threads create macroscopic spatial heterogeneity, leading to a morphological mismatch between the discrete FOV average and the continuous spatial extraction.

To precisely quantify the shading severity and the spectral filtering properties

of each structural cover, Table 4.4 synthesizes the absolute transmitted reflectance across the primary optical intervals. The extracted data highlights the profound physical complexity of the sub canopy light field.

For highly transmissive materials (such as Net 06) and selectively filtering covers (Net 03), the transmitted radiation maintains a structurally stable profile, with the geometric offset (Δ) between the two acquisition architectures remaining strictly constant across all wavelengths. However, beneath denser and structurally heterogeneous meshes like Net 02 (Black) and Net 05 (Bicolor), the transmitted flux is heavily influenced by localized scattering, diffraction, and complex micro shadowing generated by the physical polymeric threads. This extreme spatial heterogeneity in the localized irradiance field explains the wavelength dependent divergences observed in the Δ offset for these specific nets (e.g., drifting from -8.8% to -12.9% for Net 05). Rather than a measurement artifact, this morphological deviation mathematically captures how denser structural architectures physically fragment the transmitted light field.

Table 4.4: Sub canopy absolute transmitted reflectance across the primary spectral intervals. The wavelength dependent variations in the Δ offset for Nets 02 and 05 quantify the spatial heterogeneity and micro shadowing effects characterizing the transmitted light field.

Target	**Band (nm)**	**Specim FX10 (%)**	**RS-5400 (%)**	**Δ Offset**
Net 02 (Black)	400–500 (Blue)	78.2	78.7	+0.5
	500–600 (Green)	81.1	78.6	−2.5
	600–700 (Red)	81.7	78.6	−3.1
	700–750 (Red Edge)	82.0	78.5	−3.5
	750–900 (NIR)	82.0	78.6	−3.4
Net 03 (Light Green)	400–500 (Blue)	88.9	88.0	−0.9
	500–600 (Green)	91.0	89.9	−1.1
	600–700 (Red)	89.9	88.9	−1.0
	700–750 (Red Edge)	90.9	89.8	−1.1
	750–900 (NIR)	93.2	91.9	−1.3
Net 05 (Bicolor)	400–500 (Blue)	86.5	77.7	−8.8
	500–600 (Green)	89.3	77.8	−11.5
	600–700 (Red)	89.7	77.3	−12.4
	700–750 (Red Edge)	90.3	77.3	−13.0
	750–900 (NIR)	90.4	77.5	−12.9
Net 06 (Transparent)	400–500 (Blue)	90.2	82.1	−8.1
	500–600 (Green)	90.9	82.7	−8.2
	600–700 (Red)	91.7	83.2	−8.5
	700–750 (Red Edge)	92.3	83.5	−8.8
	750–900 (NIR)	92.6	83.9	−8.7

In conclusion, the sub canopy radiometric assessment definitively establishes the distinct spectral filtering properties of each agricultural cover. The radiometric differences among the targets are most pronounced in two specific spectral regions: the red band (600–700 nm) and the Near Infrared domain (750–900 nm). Within the visible spectrum, the covers exhibit stark morphological contrasts: the transparent structure (Net 06) maintains a high broadband transmission, whereas the black and

bicolor meshes (Net 02 and Net 05) impose a severe, flat attenuation. The light green cover (Net 03) introduces a highly selective chromatic signature, isolating a transmission peak in the green band (500–600 nm) followed by a sharp absorption drop in the red band. Moving into the Near Infrared region, the optical behaviors diverge completely: while Net 02 and Net 05 continue to act as severe broadband attenuators, the transmission of Net 03 surges, yielding a high NIR signal that closely mirrors the transparent baseline of Net 06.

Crucially, despite the absolute intensity offsets generated by structural micro shadowing, both the continuous spatial imaging of the Specim FX10 and the macroscopic point radiometry of the RS-5400 consistently detect these exact wavelength dependent variations across all samples. This absolute instrumental coherence confirms that the observed spectral divergences are intrinsic physical properties of the nets, rather than acquisition artifacts, successfully providing a validated foundation for the subsequent multispectral aerial simulations.

4.2.8 Multispectral Sensor Simulation

To bridge the gap between controlled indoor hyperspectral measurements and real world precision agriculture applications, the continuous high resolution hyperspectral datasets acquired with the Specim FX10 were computationally resampled to simulate the discrete spectral response of a standard multispectral camera. Specifically, the processing pipeline convolved the pure spectral signatures using the central wavelengths and full width at half maximum response functions corresponding to the nine discrete optical channels of the MAIA S2 multispectral sensor, whose architectural configuration was detailed in Section 3.5.2 (Table 3.2).

This simulation models the exact radiometric environment encountered by an Unmanned Aerial Vehicle (UAV) during overflights above protected crop systems. By applying the previously defined methodology to each discrete spectral band, the specific band dependent Shading Factor (SF_λ) was evaluated, proving that light attenuation under agricultural nets is not a uniform broadband phenomenon but a highly wavelength dependent process.

Figure 4.20 illustrates the simulated spectral signatures within the MAIA S2 bands for the definitive subset of shading covers. The resulting curves and the quantitative values summarized in Table 4.5 reveal distinct optical behaviors across the visible and near infrared (VNIR) spectrum.

An in depth engineering analysis of the simulated multispectral response highlights critical implications for aerial crop monitoring. For Net 02 (Black), the attenuation is remarkably high across all channels due to broadband absorption, yet it exhibits a decreasing gradient from the short wavelengths (20.37% in S1_VIOLET) toward the near infrared region (14.43% in S9_NIR3). Conversely, neutral and transparent covers (Net 05 and Net 06) display stable, lower attenuation profiles that decrease smoothly as wavelength increases.

The most critical operational insight emerges from the optical behavior of Net 03 (Light Green). While its visible shading factors in the blue, green, and red bands remain relatively pronounced (ranging between 9.51% and 13.19%), its interception capacity collapses dramatically in the near infrared channels, dropping to a mini-

mal Shading Factor of 3.54% in S9_NIR3. This strong spectral selectivity occurs because the green pigment and polymer structure are transparent to NIR radiation, effectively allowing the near infrared flux to pass unhindered.

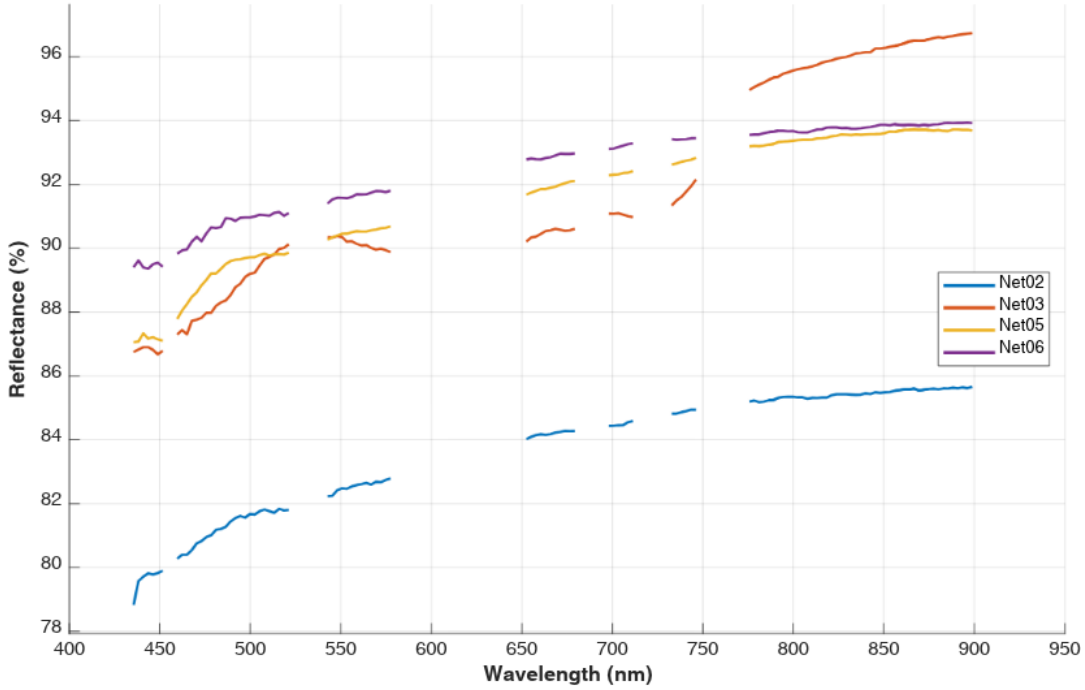


Figure 4.20: Simulated spectral signatures of the shading nets across the nine discrete bands of the MAIA S2 multispectral sensor, derived from the high resolution Specim FX10 datacubes.

Table 4.5: Band dependent Shading Factor (SF_λ %) evaluated across the nine discrete optical channels of the MAIA S2 multispectral sensor for each evaluated net.

MAIA S2 Band	**Net 02**	**Net 03**	**Net 05**	**Net 06**
S1_VIOLET	20.37	13.19	12.84	10.54
S2_BLUE	18.72	11.30	10.71	9.29
S3_GREEN	17.45	9.86	9.49	8.34
S4_RED	15.81	9.51	8.09	7.13
S5_RE1	15.51	8.95	7.66	6.80
S6_RE2	15.12	8.28	7.28	6.58
S7_NIR1	14.77	4.81	6.76	6.39
S8_NIR2	14.54	3.87	6.44	6.20
S9_NIR3	14.43	3.54	6.30	6.14

From an agronomic perspective, this severe spectral imbalance introduces a systematic distortion into vegetation indices. Because standard indices such as the Normalized Difference Vegetation Index (NDVI) rely strictly on the differential reflectance between the red band (heavily intercepted by the net) and the near infrared

band (largely transmitted without attenuation), flying over a crop covered by Net 03 will induce a strong radiometric bias. Without a dedicated band by band radiometric correction, the resulting vigor maps will experience significant artificial inflation in the NIR region, leading to distorted spatial prescription maps and erroneous agronomic assessments in precision viticulture and horticulture.

4.3 UAV Field Validation

Following the rigorous characterization of the shading nets in the controlled laboratory environment, the analytical focus shifted to the outdoor precision agriculture scenario. This section translates the theoretical optical models into real world applications by evaluating the radiometric data acquired during the UAV flights over the experimental apple orchard.

4.3.1 Spatial Distribution and Solar Angle Effect

The primary visual outputs of the photogrammetric pipeline are the high resolution NDVI maps. To evaluate both the spatial impact of the protective infrastructures and the influence of varying illumination conditions, the flights were conducted at two distinct times: at solar noon (12:00 PM) to capture the optimal zenith angle, and in the mid afternoon (4:00 PM) to assess the effect of a lower solar elevation.

Figures 4.21 and 4.22 present the generated vigor maps for the entire study area during the first and second acquisitions, respectively. A preliminary visual inspection immediately highlights the macroscopic spatial interference caused by the shading covers. In both acquisitions, the unnetted control rows display a significantly higher radiometric intensity (represented by darker green hues), indicative of a strong, unattenuated near infrared signal. Conversely, the sectors covered by both the Light Green and Black nets exhibit a visibly depressed NDVI signal, appearing systematically lighter on the color scale.

Beyond the localized effect of the nets, comparing the two flights reveals a critical operational variable: the solar zenith angle. As the sun lowers in the mid afternoon, the overall radiometric response of the entire orchard decreases. This generalized signal attenuation is visually perceptible as a global darkening of the field in the second map. The lower solar elevation increases the length and volume of the micro shadows cast by the canopy itself and by the netting structures, thereby reducing the total reflected radiance reaching the UAV sensor. The absolute reduction in the radiometric signal between the two flights was quantified across all experimental zones. From solar noon to the mid afternoon, the mean NDVI of the open sky control area dropped by 19.14%. A similar generalized reduction affected the covered zones, with the Light Green net area decreasing by 26.87% and the Black net area by 13.15%. This confirms that while the protective nets introduce a localized shading factor, the absolute magnitude of the vegetation indices acquired by the drone remains highly sensitive to the global daily illumination cycle.

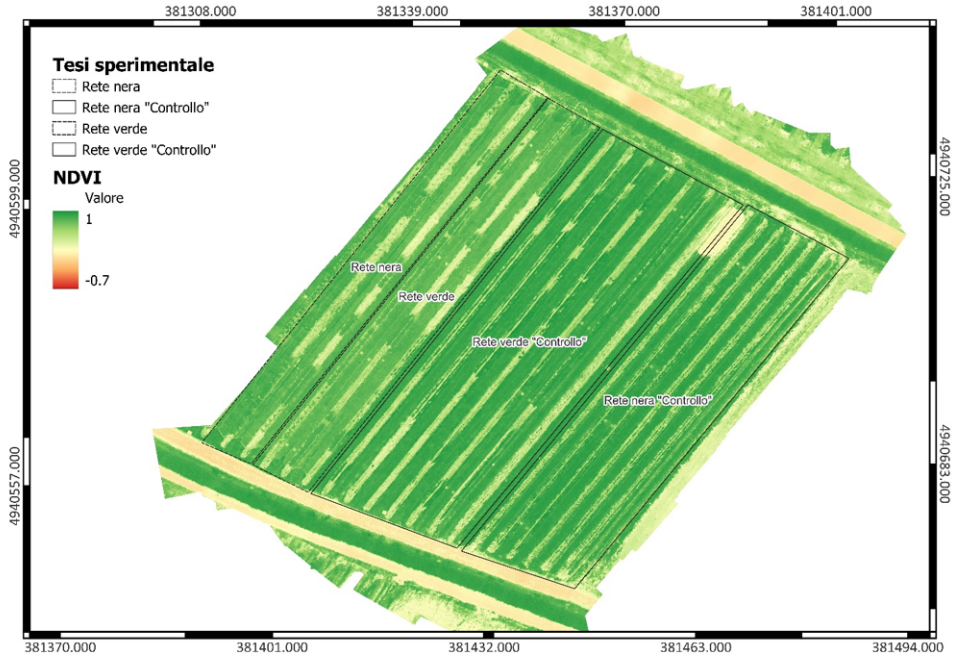


Figure 4.21: NDVI spatial distribution map of the experimental orchard acquired during Flight 1 at solar noon (12:00 PM). The map illustrates the clear radiometric attenuation in the netted zones compared to the open sky control rows under optimal illumination conditions.

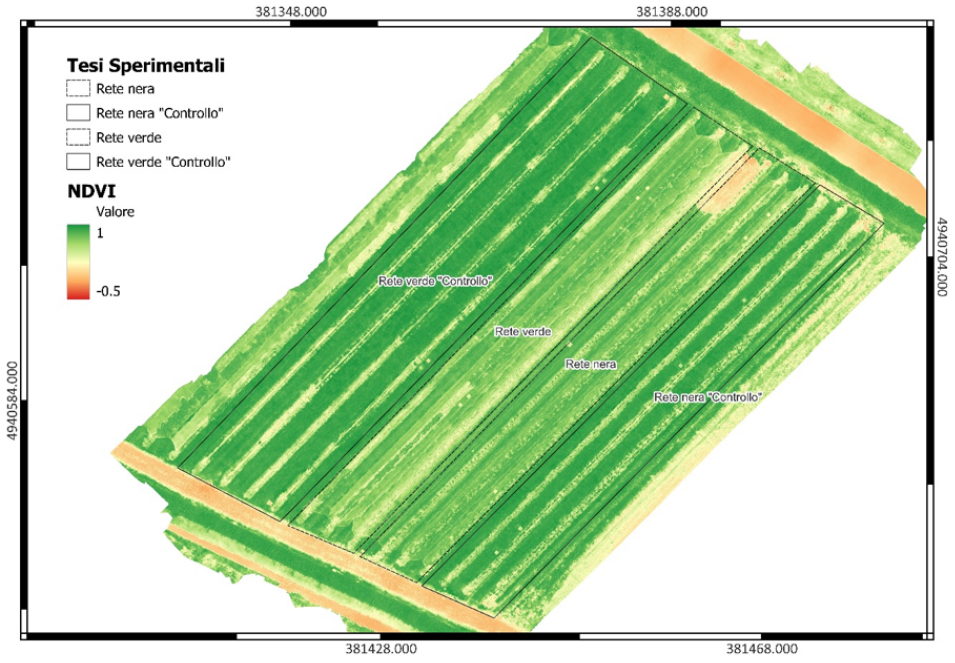


Figure 4.22: NDVI spatial distribution map acquired during Flight 2 in the mid afternoon (4:00 PM). A generalized signal reduction is observed across the entire orchard compared to solar noon, primarily driven by the lower solar elevation angle and the consequent increase in shadowing effects.

4.3.2 Statistical Quantification of the Shading Bias

To rigorously quantify the radiometric interference visually observed in the spatial maps, a statistical analysis was performed on the NDVI data extracted exclusively from the 32 standardized white calibration panels. Tables 4.6 and 4.7 summarize the descriptive statistics, including the Mean, Standard Deviation, Minimum, Maximum, and the t-test significance letters, for the solar noon and mid afternoon flight campaigns across the evaluated treatments.

During the solar noon acquisition (Flight 1), the open sky Control exhibited the highest mean NDVI value (0.606). The presence of the shading infrastructures induced a severe signal depression, dropping the mean NDVI to 0.402 under the Light Green net and 0.327 under the Black net. As discussed in the previous section, the mid afternoon acquisition (Flight 2) recorded a generalized reduction in absolute values, with the Control decreasing to 0.490.

Table 4.6: Descriptive statistics of the NDVI values extracted from the white calibration panels during Flight 1 (Solar Noon, 12:00 PM).

Treatment	**Mean NDVI**	**Std. Dev.**	**Min**	**Max**	**t-test**
Control (Open Sky)	0.606	0.063	0.479	0.675	a
Light Green Net	0.402	0.030	0.348	0.457	b
Black Net	0.327	0.014	0.309	0.343	b

Table 4.7: Descriptive statistics of the NDVI values extracted from the white calibration panels during Flight 2 (Mid Afternoon, 4:00 PM).

Treatment	**Mean NDVI**	**Std. Dev.**	**Min**	**Max**	**t-test**
Control (Open Sky)	0.490	0.062	0.398	0.578	a
Light Green Net	0.294	0.065	0.236	0.360	b
Black Net	0.284	0.049	0.237	0.351	b

However, the critical engineering finding emerges from the inferential statistics. A one way Analysis of Variance (ANOVA) followed by Tukey's Honestly Significant Difference (HSD) post hoc test ($\alpha = 0.05$) was applied to both datasets. As illustrated in the bar charts in Figures 4.23 and 4.24, the statistical behavior of the sensor remains remarkably consistent regardless of the solar zenith angle. In both flights, the Control group is assigned the significance letter 'a', denoting a statistically distinct and higher radiometric baseline. Conversely, both the Light Green and Black nets are assigned the letter 'b', indicating a highly significant difference from the unnetted control ($p < 0.05$).

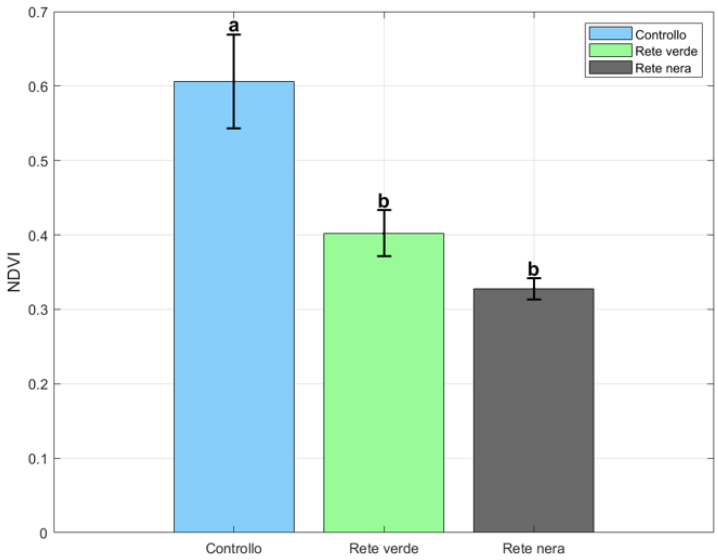


Figure 4.23: Statistical comparison of mean NDVI values across treatments for Flight 1 (Solar Noon). Bars sharing the same letter are not significantly different according to Tukey's HSD post hoc test ($p > 0.05$). The sensor successfully differentiates the open sky control ('a') from the covered zones ('b'), but fails to distinguish between the Green and Black networks.

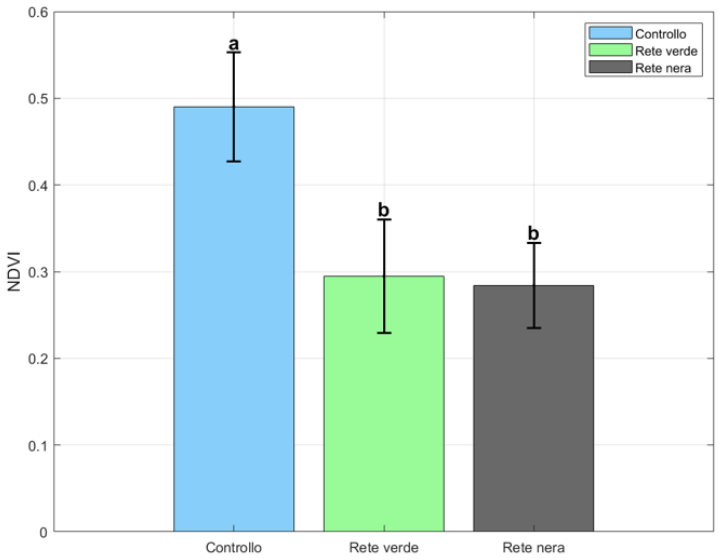


Figure 4.24: Statistical comparison of mean NDVI values across treatments for Flight 2 (Mid Afternoon). Despite the generalized reduction in absolute NDVI values caused by the lower solar angle, the statistical relationship remains identical to solar noon, confirming the systemic nature of the shading bias.

Crucially, despite the inherent chromatic and transmissivity differences between the green and black materials established during the laboratory simulations, the drone's multispectral sensor failed to statistically differentiate them in the field. The combined attenuation of the red and near infrared channels produces an overlapping NDVI response, rendering the two nets statistically indistinguishable (both 'b') under real operational conditions.

Furthermore, an analysis of the radiometric variance reveals a prominent "diffuser effect" introduced by the nets. In Flight 1, the Control area exhibited a standard deviation of 0.063. Beneath the Black net, this variance collapsed to 0.014. The physical mesh not only attenuates the total irradiance but also homogenizes the transmitted light, drastically reducing the spatial radiometric variability. From a precision agriculture perspective, this flattening of the dynamic range is highly detrimental, as it inherently suppresses the subtle vegetative contrasts required to detect early onset crop stress or variable canopy vigor.

Chapter 5

Discussions

5.1 Synthesis of the Radiometric Impact of Shading Nets

The fundamental premise of precision agriculture relies on the integrity of the optical signal reflected by the crop canopy. However, the rigorous laboratory characterizations demonstrate that agricultural shading nets do not act as simple, neutral optical density filters. Instead, they introduce complex, wavelength dependent radiometric distortions that fundamentally alter the spectral signature reaching the sensor.

The spectral atlas generated from the isolated polymeric threads reveals distinct optical behaviors strictly dictated by the material properties. Structures such as the transparent and black nets exhibit a relatively flat, broadband attenuation profile. The black net (Net 02) severely depresses the absolute signal intensity across the entire Visible and Near Infrared (VNIR) spectrum. This uniform behavior is a direct consequence of the dark polymer pigmentation, which acts as a broadband absorber, indiscriminately capturing electromagnetic radiation regardless of the specific wavelength. Conversely, the transparent net (Net 06) acts primarily as a wavelength independent optical diffuser, allowing maximal radiation transmission.

The most critical radiometric divergence emerges when analyzing the Light Green net (Net 03), which introduces a highly selective chromatic filtration. Unlike the broadband absorbers, the optical behavior of this specific cover is strongly wavelength dependent. Within the visible spectrum, the pigmentation generates a distinct reflectance peak in the green band (500–600 nm), actively mimicking the optical signature of natural foliage. This localized green reflection is immediately followed by a severe signal depression in the red region (600–700 nm), where the chromatic pigments heavily absorb the incident radiation. However, moving into the Near Infrared domain (750–900 nm), this optical behavior completely reverses. Because the plastic polymer base is highly transmissive to infrared radiation and lacks specific NIR absorbing additives, the shading capacity of the green net collapses. In this specific region, the transmittance of Net 03 surges, closely mirroring the unhindered behavior of the transparent mesh.

This complex spectral response confirms that the radiometric distortion is a physical phenomenon directly driven by the intrinsic color of the polymer and the physical geometry of the mesh. These specific spectral shifts, particularly the arti-

ficial green peak and the unbalanced red to NIR ratio, have profound implications for aerial monitoring. While this selective filtering severely biases standard mathematical algorithms like the NDVI, the interference extends to all multispectral assessments that rely on strict radiometric fidelity. Consequently, to guarantee the reliability of UAV surveys, the optical influence of each specific agricultural cover must be rigorously calibrated on a band specific basis.

5.2 Cross Scale Radiometric Consistency: Laboratory vs UAV Field Acquisitions

A critical analytical step in transitioning from controlled laboratory simulations to outdoor precision agriculture surveys is understanding the radiometric behavior of the calibration targets. During the UAV field acquisitions, the white calibration panels exhibited an unexpectedly high mean NDVI of 0.606 at solar noon. While theoretical expectations for a purely white, spectrally flat target center around an NDVI near zero, these elevated values are a documented operational characteristic of UAV based multispectral workflows and in field calibration pipelines.

The observed deviation is primarily driven by systematic offsets introduced during the outdoor radiometric calibration process. Calibration workflows relying on downwelling light sensors (ILS) and photogrammetric stitching software frequently induce over estimations of surface reflectance [17]. Research indicates that UAS multispectral sensors consistently over estimate reflectance in field settings, with lower measurement accuracy and a greater magnitude of over estimation occurring specifically in the red edge and near infrared (NIR) bands. This specific over estimation in the NIR channel directly inflates the resulting NDVI calculation.

Furthermore, the deployment of bright white calibration targets can exacerbate these radiometric anomalies. Highly reflective surfaces often push multispectral image sensors to their dynamic limits, as these sensors perform with less precision in the very high range of reflectance. It has been demonstrated that bright white targets can cause multispectral sensors to reach or approach saturation, heavily distorting the calibration algorithms, particularly in the visible bands [18]. Additionally, the physical composition of the artificial targets used in this experimental setup contributes to the baseline shift. The field panels were manufactured from paper based materials rather than perfectly diffuse radiometric Spectralon. Consequently, the paper possesses its own distinct spectral signature and non uniform reflectance profile across the visible and NIR wavelengths, yielding a natural, non zero NDVI baseline.

Despite these absolute radiometric offsets, the structural integrity of the multispectral dataset is validated by the system's robust relative discriminative capacity. It is critical to clarify that calculating a normalized band ratio like the NDVI does not eliminate the radiometric errors introduced by the canopy covers. While normalization can attenuate uniform multiplicative artifacts common to both bands (such as global illumination variations across the field), it cannot compensate for the spectrally selective systematic errors induced by the netting materials. As demonstrated in the laboratory analysis, structures like the light green net alter the visible and near

infrared bands disproportionately, actively distorting the mathematical foundation of the normalized index.

However, while the absolute NDVI values are systematically biased by this selective filtration, the system's relative response to global illumination changes remains mathematically coherent. The reduction in the white calibration panels' NDVI from 0.606 at solar noon to 0.490 in the mid afternoon mirrors the generalized signal attenuation caused by the lower solar zenith angle. Crucially, the relative radiometric separation between distinct ground features remains strictly intact. An analysis of common pixels across the two temporal flights reveals that healthy vegetation shifted systematically from an NDVI of 0.93 to 0.88, while bare soil shifted from -0.035 to 0.018. This consistent, clear separation between the radiometric classes confirms that the sensor's ability to discriminate between canopy vigor, bare soil, and shading structures is completely preserved, allowing for robust spatial differentiation despite the underlying systematic bias.

5.3 Implications for Precision Agriculture Monitoring

The translation of raw optical data into actionable agronomic insights is the ultimate goal of any precision agriculture workflow. However, the introduction of protective structures over modern orchards fundamentally disrupts the standard relationship between canopy reflectance and crop physiology. Based on the physical optical alterations quantified in the laboratory and the statistical evidence gathered during the outdoor UAV campaigns, it is clear that flying over netted environments requires a paradigm shift in how spatial data is interpreted.

The physical presence of the netting material induces systemic radiometric distortions that directly affect the reliability of standard vegetation indices. These optical interferences do not simply lower the overall brightness of the image, but actively modify the spatial distribution and the spectral composition of the light reaching the sensor. The following paragraphs detail the specific agronomic implications of these complex distortions, highlighting how the protective infrastructure impacts radiometric variance, alters the accuracy of prescription mapping, and defines a new statistical baseline for precision monitoring strategies.

5.3.1 The Diffuser Effect and Loss of Radiometric Variance

One of the most critical phenomena observed during the field validation is the profound reduction in spatial radiometric variance beneath the protective structures. As established in the statistical analysis, the physical mesh acts as an optical diffuser. It not only attenuates the total incoming irradiance but also severely homogenizes the transmitted light field. This was empirically proven by the collapse of the standard deviation values under the covered zones compared to the open sky control areas. From an agronomic perspective, this flattening of the dynamic range is highly problematic. Precision agriculture relies heavily on detecting subtle spatial contrasts in crop vigor to identify early signs of localized water stress, nutrient deficiencies,

or disease outbreaks. When the shading net artificially compresses the radiometric variance, these crucial micro variations are effectively masked. Consequently, the resulting vigor map appears artificially uniform, depriving the agronomist of the detailed spatial heterogeneity required to execute timely and targeted field interventions. To effectively mitigate this homogenization and ensure the generation of reliable agronomic data in future applications, this optical interference must be analyzed on a case by case, net by net, and band by band basis. Only through such a highly specific calibration approach can the masked radiometric variance be mathematically restored and accurately interpreted.

5.3.2 Systematic Bias in Prescription Maps

Beyond the loss of spatial variance, the physical interposition of any shading net introduces a fundamental error in the calculation of the absolute vegetation indices. Because the mixed pixel effect physically blends the spectral signature of the canopy with the radiometric interference of the overlying polymer and its cast shadows, the resulting vigor map reflects an apparent vigor rather than the real physiological status of the plant.

This systematic bias poses a severe risk when multispectral data is utilized to drive automated agricultural machinery. In a standard precision agriculture workflow, NDVI maps are translated into prescription maps to guide variable rate application tractors. If the raw, uncalibrated data from a netted orchard is fed into these automated systems, the software will inevitably misinterpret the true health of the crop. For instance, an artificially inflated or depressed NDVI value could command the machinery to distribute an incorrect dosage of fertilizers or phytosanitary products, leading to either costly chemical waste or severe nutritional deficiencies. Therefore, acknowledging and mathematically correcting this apparent vigor is an absolute prerequisite before employing any UAV derived map for autonomous variable rate operations.

5.3.3 Statistical Discriminative Capacity

Despite the spectral mixing and the systematic bias in apparent vigor, the inferential statistical analysis yielded a highly positive and encouraging outcome. The application of the Analysis of Variance (ANOVA) and the subsequent Tukey HSD test successfully and unequivocally differentiated the open sky control zones from the netted zones.

While the commercial multispectral sensor could not statistically separate the optical signature of the black net from the light green net under real field conditions, distinguishing the specific polymer material was not the primary operational objective of this validation. The critical achievement is the robust statistical separation between the presence and the absence of the protective infrastructure. The data proves that the drone's sensor is highly sensitive to the systemic radiometric shift caused by the nets, registering it as a clear, distinct statistical class rather than random background noise.

This robust discriminative capacity is a fundamental starting point for advancing

precision agriculture under covered environments. Knowing that a standard UAV payload can statistically isolate the netted areas from the open sky areas means that future software pipelines could be trained to automatically recognize these distinct zones. Once the covered regions are automatically identified, it will be possible to apply the specific mathematical correction factors developed in the laboratory, thereby restoring the true radiometric value of the crop and enabling accurate automated monitoring.

Chapter 6

Conclusions and Future Developments

6.1 Conclusions

The primary objective of this thesis was not merely to identify, but to rigorously quantify the optical impact of agricultural nets on multispectral UAV surveys. The experimental campaign successfully achieved this goal, establishing a highly solid and positive foundation for future precision agriculture operations. Rather than concluding that standard drone surveys are ineffective under netted environments, this research demonstrated that the radiometric interference caused by the protective nets is not random optical noise, but a clear, constant, and statistically measurable physical variation. The unequivocal separation between covered and open sky areas, definitively validated by the ANOVA analysis, proves that the multispectral sensor captures this environmental shift with extreme precision. Furthermore, the laboratory characterizations revealed that each protective net alters the spectral response in a unique manner, strictly depending on its specific polymer color and mesh geometry. Crucially, recognizing that this optical distortion is highly systematic means that the problem is inherently mathematically remediable. Because the radiometric alteration is predictable and consistent for each specific net type, it is entirely possible to calculate and apply dedicated correction factors. Ultimately, this research marks a foundational step forward for remote sensing in modern orchards. It officially transitions the field from a blind methodology, where the physical presence of the net is erroneously ignored, to a conscious and scientifically grounded workflow. By acknowledging and precisely quantifying the active optical role of shading structures, this thesis lays the necessary groundwork to upgrade the drone from a standard mapping device into an advanced, adaptable monitoring tool, fully capable of delivering reliable agronomic insights even beneath complex agricultural infrastructures.

6.2 Operational Guidelines

To bridge the gap between experimental research and practical agronomic application, several operational protocols must be established. Based on the insights

gathered from both laboratory and field campaigns, the following guidelines are proposed to optimize future UAV surveys over netted orchards:

First, it is highly recommended to conduct and process flights encompassing both covered and open sky areas simultaneously. Processing the entire dataset within a single photogrammetric and radiometric workflow ensures that the relative differences between the two zones are preserved. This unified approach provides a robust comparative baseline, allowing the agronomist to clearly isolate the specific optical interference caused by the shading structure from other environmental variables.

Second, the selection and deployment of calibration targets must be fundamentally reevaluated. Bright white panels should be strictly reserved for controlled laboratory environments, where they are highly effective for quantifying shadow projection and calculating the physical coverage percentage of the mesh. For active field validation and advanced radiometric calibration, operators should instead utilize reference panels featuring various shades of green that closely simulate actual canopy reflectance. Deploying these green reference targets in both laboratory and field settings allows researchers to precisely track how the net alters the specific spectral signature of the background foliage. Naturally, these artificial targets must be accompanied by direct validation on real, homogeneous vegetation within the orchard.

Finally, while standard nadir flight plans remain valid for general monitoring, advanced precision horticulture requires a transition towards three dimensional modeling. The physiological health of a fruit tree is rarely uniform; the upper canopy may present entirely different vigor conditions compared to the lateral or lower leaves. Capturing oblique imagery alongside nadir photos to generate high resolution three dimensional models will enable agronomists to assess the health of the entire plant architecture. This spatial awareness is particularly crucial under protective nets, where the shading effect itself can vary significantly along the vertical profile of the tree.

6.3 Future Developments

To move beyond the initial laboratory and field validation, future research must prioritize direct applications on real vegetation. Since modern orchards and their protective infrastructures remain in place for several years, conducting an initial, highly detailed field calibration is a highly valuable one time investment. By performing parallel flights over netted and open sky rows of the exact same crop variety, researchers can calculate precise radiometric correction factors. While this thesis focused primarily on the NDVI to demonstrate the impact on variable rate spraying operations, this identical calibration methodology must be extended to all other vegetation indices and sensor types. Over time, this case by case approach will culminate in the creation of a comprehensive radiometric database, mapping the specific spectral interference of every commercial net paired with various crop varieties.

Once this extensive database is established, the calibration process can become fully automated. Future precision agriculture software pipelines could feature dedicated modules where the agronomist simply inputs the color and technical speci-

fications of the installed net. The software would then automatically retrieve the appropriate parameters from the database and apply the necessary band by band corrections directly to the raw images. This algorithmic automation will eliminate the need for complex manual adjustments, rendering the workflow completely seamless for the end user.

Looking further ahead, the integration of drone technology with emerging smart agriculture frameworks will radically transform monitoring capabilities. Current shading technologies remain largely traditional, but the near future points toward automated hail nets capable of opening and closing autonomously based on real time weather conditions. As these mechanized systems become more economically accessible and widespread, they will offer unprecedented opportunities for dynamic in flight calibration. Furthermore, the true potential of UAV based remote sensing will be fully unlocked when fused with complementary data streams. By integrating aerial multispectral maps with ground based soil sensors and wearable plant biosensors, the industry will achieve a truly holistic monitoring ecosystem. Within a few years, the complex experimental calibration processes addressed in this thesis could become a daily, fully automated reality in smart orchards worldwide.

Bibliography

[1] Google Earth, "Satellite imagery of agricultural fields with anti-hail nets." Imagery Copyright 2025 Airbus, 2025. Accessed: 2026/03/07.

[2] A. Walter, R. Finger, R. Huber, and H.-P. Piepho, "Smart farming is key to developing sustainable agriculture," *Proceedings of the National Academy of Sciences*, vol. 114, no. 24, pp. 6148–6150, 2017.

[3] W. H. Maes and K. Steppe, "Perspectives for remote sensing with unmanned aerial vehicles in precision agriculture," *Trends in Plant Science*, vol. 24, no. 2, pp. 152–164, 2019.

[4] Y. Shahak, "Photoselective netting: an overview of the concept, r&d and practical implementation in agriculture," *Acta Horticulturae*, no. 1015, pp. 155–162, 2014.

[5] N. Keshava and J. F. Mustard, "Spectral unmixing," *IEEE Signal Processing Magazine*, vol. 19, no. 1, pp. 44–57, 2002.

[6] GIS4Schools, "Remote sensing image analysis." `https://gis4schools.readthedocs.io/en/latest/part3/rs_imageanalysis.html`. Accessed: August 2026.

[7] Alexander D. Levin and Lloyd Nackley, "Principles and practices of plant-based irrigation management." `https://www.researchgate.net/publication/354979683_Principles_and_Practices_of_Plant-based_Irrigation_Management`. Accessed: August 2026.

[8] Azzurra Del Sarto, "Ndvi: Cos'è e come valuta la salute delle colture." `https://tethys.farm/ndvi-salute-colture/`. Accessed: August 2026.

[9] Manisha Das Chaity and Jan van Aardt, "Articolo mdpi - remote sensing." `https://www.mdpi.com/2072-4292/16/3/498`. Accessed: August 2026.

[10] Sanaz Jarolmasjed and Sindhuja Sankaran and Afef Marzougui and Sarah Kostick and Yongsheng Si and Juan Quirós and Kate M Evans, "High-throughput phenotyping of fire blight disease symptoms using sensing techniques in apple." `https://www.researchgate.net/publication/333003373_High-Throughput_Phenotyping_of_Fire_Blight_Disease_Symptoms_Using_Sensing_Techniques_in_Apple`. Accessed: August 2026.

[11] DJI, "Zenmuse l2 specifications." https://enterprise.dji.com/it/zenmuse-l2. Accessed: August 2026.

[12] SAL Engineering, "Maia multispectral camera - technical specifications." https://www.spectralcam.com/maia-tech-2/. Accessed: August 2026.

[13] Specim Spectral Imaging Ltd., "Specim announces new camera series for industrial needs." https://www.specim.com/specim-announces-new-camera-series-for-industrial-needs/. Accessed: August 2026.

[14] Agroexpert, "Sadovyy robot insighttrac rover stal pobeditelem premii ag robot of the year 2023." Accessed: August 2026.

[15] Ken Treloar, "Do orchard nets break autonomous agtech?." https://www.agtechdiaries.com/p/do-orchard-nets-break-autonomous-agtech. Accessed: August 2026.

[16] Alejandro Ehrenfeld and Álvaro Egaña and Felipe Andrés Santibáñez-Leal and Felipe Garrido and Marcia Ojeda and Brian Townley and Felipe Navarro, "Hidsag: Hyperspectral image database for supervised analysis in geometallurgy." https://www.researchgate.net/publication/369477992_HIDSAG_Hyperspectral_Image_Database_for_Supervised_Analysis_in_Geometallurgy/figures?lo=1. Accessed: August 2026.

[17] S. Cao, B. Danielson, S. Clare, S. Koenig, C. Campos-Vargas, and A. Sanchez-Azofeifa, "Radiometric calibration assessments for uas-borne multispectral cameras: Laboratory and field protocols," *ISPRS Journal of Photogrammetry and Remote Sensing*, vol. 149, pp. 132–145, 2019.

[18] L. Deng, Z. Mao, X. Li, Z. Hu, F. Duan, and Y. Yan, "Uav-based multispectral remote sensing for precision agriculture: A comparison between different cameras," *ISPRS Journal of Photogrammetry and Remote Sensing*, vol. 146, pp. 124–136, 2018.